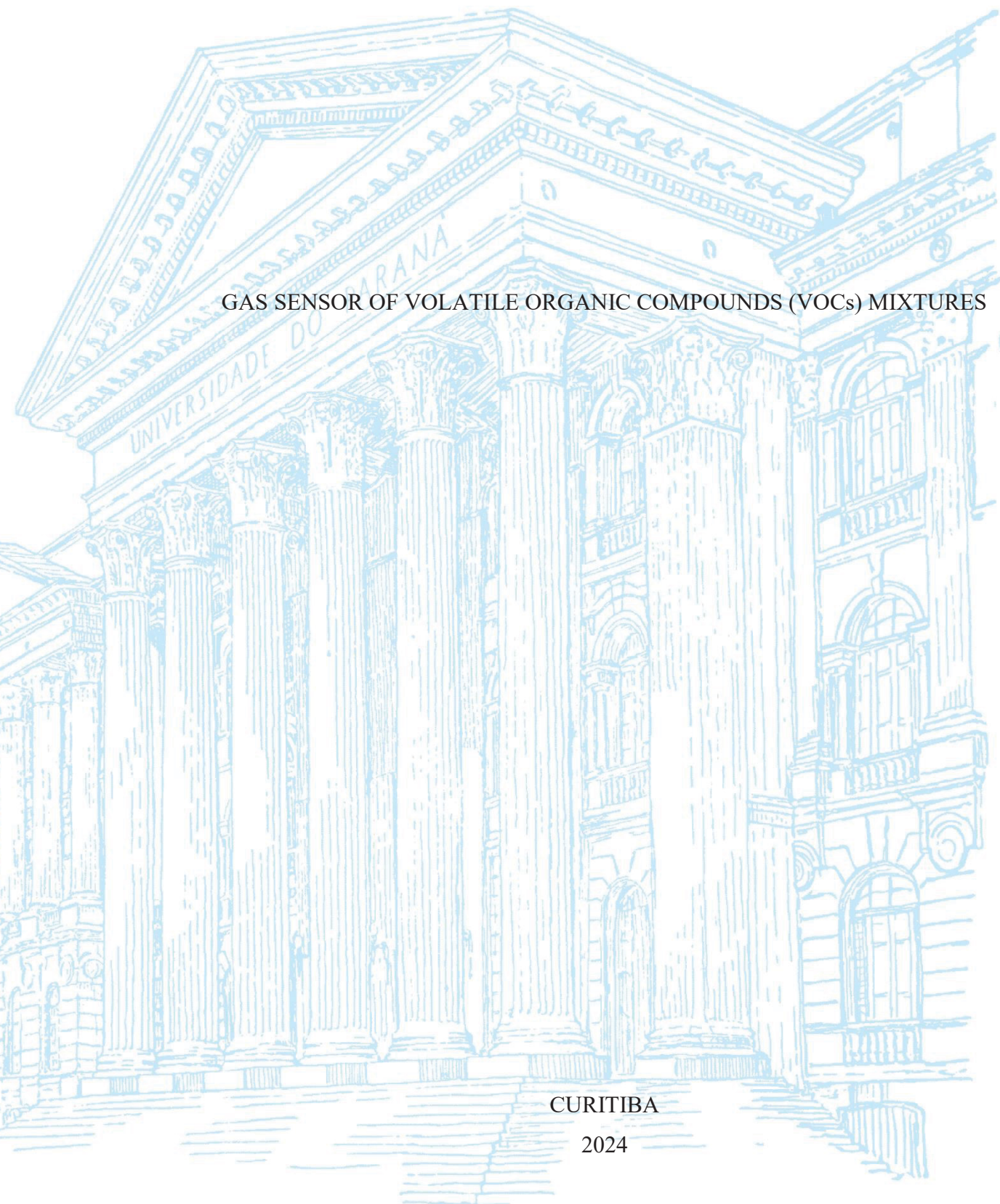UNIVERSIDADE FEDERAL DO PARANÁ

CLARA INÉS GARCÍA MARTÍNEZ

GAS SENSOR OF VOLATILE ORGANIC COMPOUNDS (VOCs) MIXTURES

CURITIBA

2024

CLARA INÉS GARCÍA MARTÍNEZ

GAS SENSOR OF VOLATILE ORGANIC COMPOUNDS (VOCs) MIXTURES

Tese apresentada ao Programa de Pós-Graduação em Engenharia e Ciência dos Materiais, no Setor de Tecnologia, na Universidade Federal do Paraná, como requisito parcial à obtenção do título de Doutora em Engenharia e Ciência dos Materiais.

Orientador: Prof. Dr. José P. Mansueto Serbena

CURITIBA

2024

TERMO DE APROVAÇÃO

Os membros da Banca Examinadora designada pelo Colegiado do Programa de Pós-Graduação ENGENHARIA E CIÊNCIA DOS MATERIAIS da Universidade Federal do Paraná foram convocados para realizar a arguição da tese de Doutorado de **CLARA INÉS GARCÍA MARTÍNEZ** intitulada: **Gas Sensors of Volatile Organic Compounds (VOCs) Mixtures**, sob orientação do Prof. Dr. JOSÉ PEDRO MANSUETO SERBENA, que após terem inquirido a aluna e realizada a avaliação do trabalho, são de parecer pela sua APROVAÇÃO no rito de defesa.

A outorga do título de doutora está sujeita à homologação pelo colegiado, ao atendimento de todas as indicações e correções solicitadas pela banca e ao pleno atendimento das demandas regimentais do Programa de Pós-Graduação.

CURITIBA, 23 de Fevereiro de 2024.

Assinatura Eletrônica
28/02/2024 09:42:19.0
JOSÉ PEDRO MANSUETO SERBENA
Presidente da Banca Examinadora

Assinatura Eletrônica
29/02/2024 11:33:52.0
PEDRO BERTEMES FILHO
Avaliador Externo (UNIVERSIDADE DO ESTADO DE SANTA CATARINA)

Assinatura Eletrônica
29/02/2024 12:20:35.0
JAREM RAUL GARCIA
Avaliador Externo (UNVERSIDADE ESTADUAL DE PONTA GROSSA)

Assinatura Eletrônica
28/02/2024 10:29:27.0
CÉSAR AUGUSTO DARTORA
Avaliador Interno (UNIVERSIDADE FEDERAL DO PARANÁ)

Assinatura Eletrônica
28/02/2024 10:33:03.0
CAMILLA KARLA BRITES QUEIROZ MARTINS DE OLIVEIRA
Avaliador Interno (UNIVERSIDADE FEDERAL DO PARANÁ)

UNIVERSIDADE FEDERAL DO PARANÁ - CURITIBA - Paraná - Brasil
CEP 81531-990 - Tel: (41) 3361-3308 - E-mail: pipe@ufpr.br
Documento assinado eletronicamente de acordo com o disposto na legislação federal Decreto 8539 de 08 de outubro de 2015.
Gerado e autenticado pelo SIGA-UFPR, com a seguinte identificação única: 339527
**Para autenticar este documento/assinatura, acesse https://siga.ufpr.br/siga/visitante/autenticacaoassinaturas.jsp
e insira o codigo 339527**

I would like to dedicate this thesis to my beautiful family;
who believed in me, more than I do myself.

ACKNOWLEDGMENTS

"The most difficult thing is the decision to act, the rest is merely tenacity."

Amelia Earhat

And sometimes, serendipity comes along!

RESUMO

Esta tese teve como objetivo investigar experimentalmente o comportamento de detecção de vapores de acetona e etanol, através da fabricação e caracterização de sensores baseados em nanoflocos de hBN dopados com BaF_2 em porcentagens de 2,5 %, 5 % e 10 %, bem como em compósitos a base de óxido de nanopartículas de óxido de zinco (ZnO), grafeno induzido por laser (LIG), nanotubos de carbono de parede múltipla (MWCNT) e polivinilpirrolidona (PVP): LIG/ZnO/MWCNTs e LIG/ZnO/MWCNTs/PVP. A resposta dos sensores foi avaliada por meio de medidas de espectroscopia de impedância elétrica, considerando tanto a concentração do analito quanto a frequência de operação. Para os sensores baseados em nanofolhas de hBN, as frequências de operação foram definidas entre 1 e 3 kHz, determinando-se o limite de detecção (LoD) e a sensitividade dos dispositivos. As sensitividades e os limites de detecção foram derivados da parte real da impedância (denominada na tese como resistência). Os sensores de hBN com 2,5% de BaF_2 demonstraram sensitividades para acetona e etanol de $2,1 \times 10^{-2}$ e $1,6 \times 10^{-2}$ ppm^{-1}, com LoD's de 43,2 e 61,7 ppm, respectivamente. Os resultados indicam uma correlação com a presença de defeitos nestas amostras. Os sensores de hBN apresentaram tempos de resposta e recuperação inferiores a 100 segundos. Adicionalmente, o sensor de hBN com 5% de BaF_2 manteve consistentemente a mesma sensitividade de $0,04 \times 10^{-2}$ ppm^{-1} após 18 meses de armazenamento. Também foi explorado o potencial dos sensores com eletrodos interdigitados de LIG para detecção de acetona e etanol. As estruturas combinadas com eletrodos de LIG incluíram ZnO, MWCNTs e PVP. À medida que as concentrações do analito variaram entre 0 e 300 ppm, observou-se um aumento na resistência de resposta dos sensores baseados em LIG/ZnO/MWCNTs e LIG/ZnO/MWCNTs/PVP, avaliados em termos de LoD e sensitividade a uma frequência de 100 Hz. Para os sensores baseados em LIG/ZnO/MWCNTs, o LoD para acetona e etanol foi 8 e 58 ppm, com sensitividades de $0,076 \times 10^{-2}$ e $0,018 \times 10^{-2}$ ppm^{-1}, respectivamente. Da mesma forma, para os sensores baseados em LIG/ZnO/MWCNTs/PVP, determinou-se o LoD para acetona e etanol em 11 e 17 ppm, com sensitividades de $0,191 \times 10^{-2}$ e $2,319 \times 10^{-2}$ ppm^{-1}, respectivamente. As medições de espectroscopia de impedância elétrica analisaram a resistência do limite de grão, no caso dos sensores baseados em LIG/ZnO/MWCNTs/PVP, aumentando de $4,23 \times 10^6$ até $33,33 \times 10^6$ Ω quando a concentração do etanol aumenta de 0 a 300 ppm.

Palavras-chave: hBN. Etanol. Acetona. Grafeno induzido por laser. Nanopartículas de óxido de zinco. Nanotubos de carbono de paredes múltiplas. LIG. Detecção de gases. Sensores de VOC's.

ABSTRACT

This thesis aimed to experimentally investigate the detection behavior of acetone and ethanol vapors through the fabrication and characterization of sensors based on hexagonal boron nitride (hBN) nanoflakes produced by incorporating barium fluoride (BaF_2) at different weight percentages: 2.5 %, 5 %, and 10, as well as zinc oxide (ZnO), laser-induced graphene (LIG), multi-walled carbon nanotubes (MWCNTs) and polyvinylpyrrolidone (PVP): LIG/ZnO/MWCNTs and LIG/ZnO/MWCNTs/PVP composites. The sensors' response was evaluated through electrical impedance spectroscopy measurements, considering both analyte concentration and operating frequency. In the case of the sensors based on hBN nanosheets, operating frequencies were set between 1 and 3 kHz to determine the detection limit (LoD) and sensitivity of the devices. Sensitivities and detection limits were derived from the real part of impedance (referred to as resistance in this thesis). hBN sensors with 2.5% BaF_2 showed sensitivities for acetone and ethanol of 2.1×10^{-2} and 1.6×10^{-2} ppm^{-1}, with detection limits of 43.2 and 61.7 ppm, respectively. The results indicate a correlation with the presence of defects in these samples. hBN sensors exhibited response and recovery times of less than 100 seconds. Additionally, the hBN sensor with 5% BaF_2 maintained a consistently same sensitivity of 0.04×10^{-2} ppm^{-1} after 18 months of storage. The potential of sensors with laser-induced graphene (LIG) interdigitated electrodes for detecting acetone and ethanol was also explored. Structures combined with LIG electrodes included ZnO, MWCNTs, and PVP. As analyte concentrations varied between 0 and 300 ppm, an increase in response resistance was observed for sensors based on LIG/ZnO/MWCNTs and LIG/ZnO/MWCNTs/PVP, evaluated in terms of LoD and sensitivity at a frequency of 100 Hz. For sensors based on LIG/ZnO/MWCNTs, the LoD for acetone and ethanol was 8 and 58 ppm, with sensitivities of 0.076×10^{-2} and 0.018×10^{-2} ppm^{-1}, respectively. Similarly, for sensors based on LIG/ZnO/MWCNTs/PVP, the LoD for acetone and ethanol was determined to be 11 and 17 ppm, with sensitivities of 0.191×10^{-2} and 2.319×10^{-2} ppm^{-1}, respectively. Electrical impedance spectroscopy measurements analyzed the grain boundary resistance, in the case of sensors based on LIG/ZnO/MWCNTs/PVP, increasing from 4.23×10^6 to 33.33×10^6 Ω as the ethanol concentration increased from 0 to 300 ppm.

Keywords: hBN. Ethanol. Acetone. Laser induced graphene. Zinc oxide nanoparticles. Multi walled carbon nanotubes. LIG. Gas sensing. VOC's sensors.

TABLE OF CONTENTS

CHAPTER 1

1 GENERAL INTRODUCTION

1.1 BACKGROUND AND MOTIVATION

We perceive changes in the environment that surrounds us through the five senses, which act as peripheral detection devices. Sensory cells of the senses respond to different stimuli, carrying information through the nervous system to the brain, where they will be processed and analyzed, resulting in the different experienced sensations (Figure 1). Inside our senses, smell and taste are responsible for perceiving variations in the chemical composition around us, preferably in the gas and liquid phase[1], Consequently, chemical sensors serve as artificial analogs to our innate sensory systems. Another interesting case involves mosquitoes, equipped with a set of sensors in their antennae, including a chemical sensor capable of detecting carbon dioxide and lactic acid from distances of up to 36 meters. Mammals and birds release these gases when they breathe. Certain chemicals in sweat also seem to attract mosquitoes, explaining why individuals who perspire more readily tend to attract more of these insects[2].
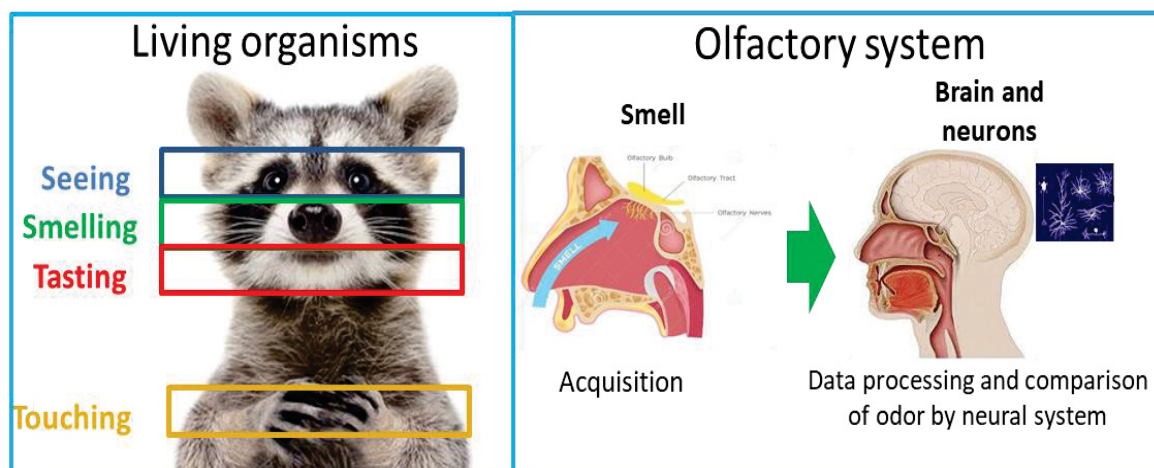
Figure 1 – Schematic of the five senses and human olfactory system[3].

Similarly, modern society has developed electronic elements or devices that are capable of detecting external stimuli and, as a consequence, show a response[1], some examples are shown in Figure 2.
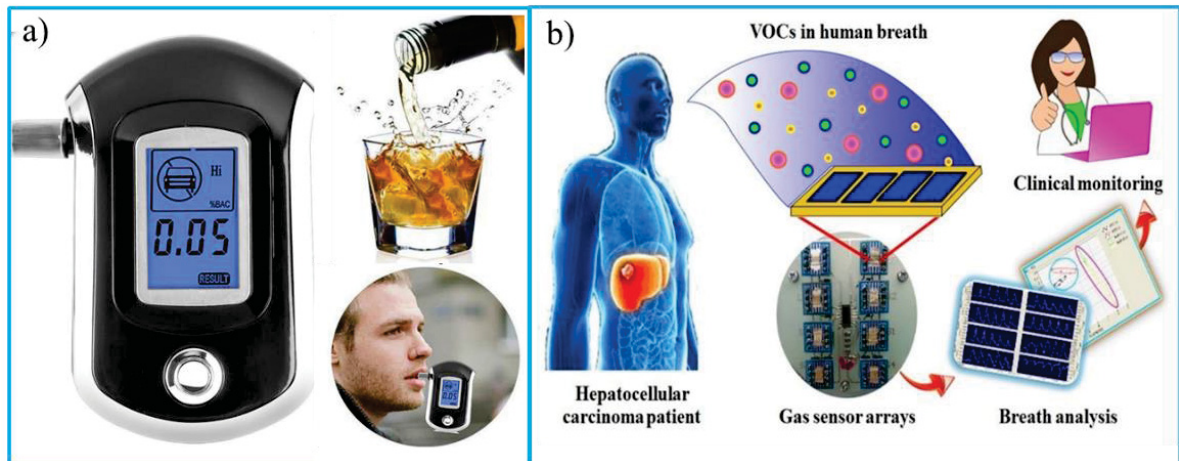
Figure 2 – Portable Police Breath analyser (a) and schematic diagram of VOCs exhaled breaths monitoring for liver cancer screening method (b)[4].

Sensors have been developed for the control of conditions such as temperature, concentration of chemical species, pressure, etc. in areas such as the aerospace field, integrated circuits, food industries, farming industries, environmental science, national security sector, healthcare area and many more[2,5–7] (Figure 3).
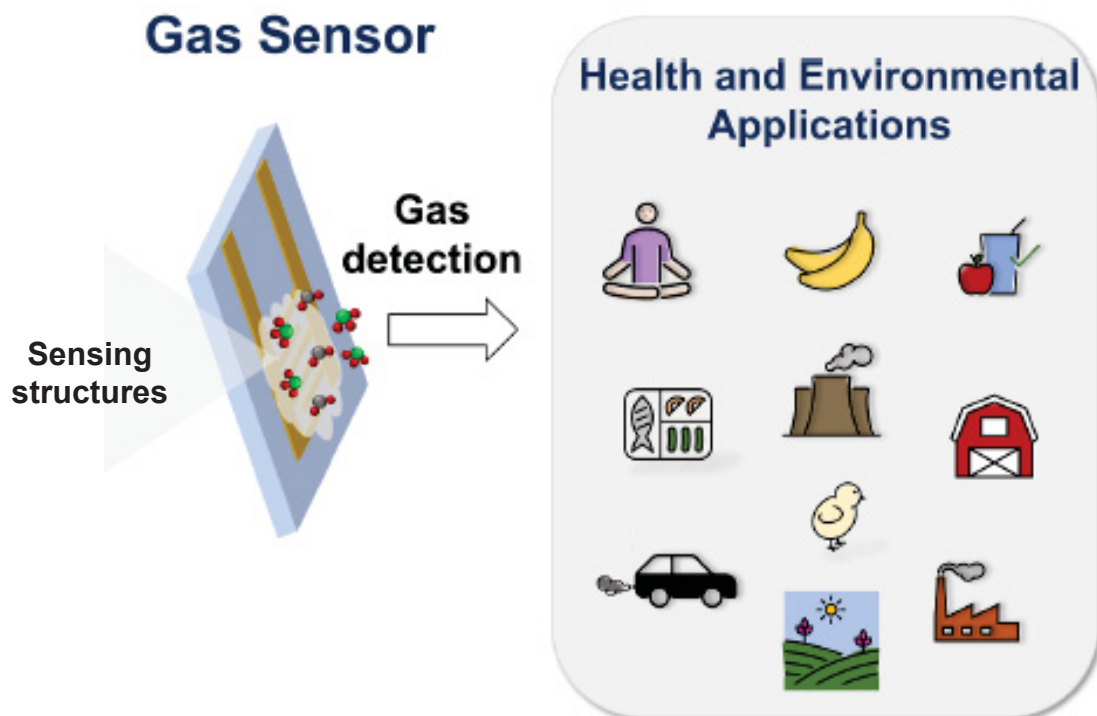
Figure 3 – Schematic of sensors applications[8].

To illustrate how sensors have changed and improved almost every aspect of our lives, the example of the biosensor for measuring glucose levels, proposed in 1962 by Clark and Lyons[9], is brought forward. They observed that people with diabetes died prematurely because

the disease was poorly controlled. Diabetic patients had to go to the hospital to determine their glucose concentration. Furthermore, the results would take days or weeks to be seen and interpreted by a doctor. This meant that the dose of insulin that was injected was always an approximate amount. Today, home blood glucose meters are used by millions of people. Another example is pregnancy tests[10]. It has a specific receptor to detect a single hormone that is present in the urine of women. These two cases are fully selective biosensors. What will our future be like? We could have a series of portable sensors where we could analyze each type of disease. Early, accurate and informative diagnosis is essential for selecting the most appropriate therapy and administering it in time. Rapid identification of an infectious outbreak is crucial to stem an epidemic. Clinical diagnosis thus must evolve even more to incorporate new methods and technologies that enable rapid, simple screening of the population, to detect diseases before their physical onset. Colon, lung, ovarian, pancreatic cancer, and those types of cancer that we can only detect when they are already in more advanced stages, with these devices will be able to be detected when those initial biomolecular changes start[11–13].

Preti et al. (2018) studied gas sensors to detect ovarian cancer. Their research demonstrated that dogs and electronic devices are capable of detecting the change in scent that accompanies the onset of ovarian cancer, even detecting these markers at an early stage before the cancer is lethal. There is a change in metabolism that is translated into the blood and causes the blood to have a different odor. Volatile organic compounds (VOCs) may possess an odor and can be found emanating from all body fluids. As cells turn malignant, analyzing changes in these VOCs can provide insight into cancer onset and diagnosis. However, modern medicine does not utilize the odor information present and emanating from the body[14,15].

But Haick et al. have taken smell diagnosis to the next level. They found that detection of these VOCs throughout breath would be the most beneficial[16–20]. They have identified a unique fingerprint in the breath of people with 17 different types of diseases. People have a unique fingerprint that distinguishes one person from another, but in patients, that fingerprint changes significantly, and exhaled breath could discriminate between different diseases. They have developed a device that contains two nanomaterials, silicon nanowires and gold nanoparticles, which can imitate the olfactory system of a human or a canine. The electronic sensor detects whether the patient is healthy or has a disease, and even more interestingly, it can predict who is at high risk of developing a disease in the future. This is a critical point because it identifies cancer or disease at very early stages, significantly increasing the survival rate. For example, in the case of lung cancer, they demonstrated an increase survival rate from 10 % to 70 % only by early diagnosis[21].

Detection of volatile organic compounds (VOCs) in exhaled breath is a very attractive non-invasive diagnostic tool for the fast and simple recognition of various diseases, including diabetes[22–24]. In particular, the breathing diagnosis for diabetes is largely based on an acetone breath test[25]. Currently, diagnosing cancer is a very painful process, therefore if VOCs sensor can add a step that is not painful, not invasive and can diagnose cancer at much earlier stages, it is worth investigating. Besides, monitoring and detecting toxic gases related to human and environmental health quickly and reliably is one of the challenges faced by humanity at the dawn of the 21st century[26] and could be a real game changer for humanity. The measurement of volatile organic compounds (VOCs) in real-time and under various conditions faces limitations in terms of applicability, including high costs, impracticality due to bulky equipment (such as gas chromatography-mass spectrometry (GC/MS), mass spectrometry (MS), atomic absorption spectroscopy (AAS), and others)[27], slow data processing, and the requirement for skilled personnel[28]. However, these techniques do offer several advantages, such as high precision and low detection limits. They are capable of simultaneously detecting a wide range of analytes. On the other hand, the utilization of chemical sensors for these purposes is still in the developmental stage.

1.2 OBJECTIVES

Overall Purpose

Optimize the set of parameters that determine the best performance on VOCs gas sensors operating under analytes mixtures and concentrations. These parameters include various types of nanoparticles, electrodes, operating conditions, and VOCs concentrations.

Specific objectives

- ✓ Determine the conditions to prepare nanostructures dispersion, such as solvents as well as surfactants, nanoparticles concentration and mixing condition with the best sensing response.
- ✓ Design an experimental set-up for the complete control of the variables under study, like temperature, voltage and analyte concentration.

✓ Characterize the sensing materials through Scanning Electron Microscope (SEM), Transmission Electron Microscopic (TEM), Energy-dispersive X-ray spectroscopy (EDS), Raman spectra and X-ray diffraction (XRD).

✓ Characterize the devices by evaluating sensitivity, selectivity, detection and quantification limits, response and recovery times, and conducting electrical impedance spectroscopy analysis. This comprehensive approach aims to determine the models of the sensor operation.

1.3 METHODOLOGY

This research was developed as follows:

1. A comprehensive literature review on state-of-the-art sensors based on nanostructures was conducted to identify potential research opportunities and issues to be solved.

2. Proficiency in experimental techniques applicable to sensor devices was achieved through theoretical study and practical application.

3. Sensors based on various types of new nanoparticles were evaluated when exposed to a range of analytes, in order to select the materials with the best sensing properties to detect VOCs.

4. After selecting the appropriate sensing materials, the best operating conditions were identified. It is expected the optimization of the sensitivity, detection and quantification limits, as well as response and recovery times.

5. Characterization of the active materials used in the sensor devices was performed to gain a comprehensive understanding of their properties.

6. Finally, the performance of the sensors was analyzed by integrating material and sensor characterization, along with electrical impedance spectroscopy analysis. This approach allowed us to uncover potential phenomena within the system by extracting parameters from the equivalent circuit.

The studies related to this thesis have been presented at conferences and seminars. The study on the detection of ammonia vapor and other VOCs, presented in chapter 3, was published in Journal of Physics: Materials[29] and in Chemosensors[30]. The study on the detection of polar and non-polar VOCs was published in Materials Today Communications[31]. The research presented in chapter 4 will be published in 2024.

CHAPTER 2

2 LITERATURE REVIEW

This chapter provides a comprehensive bibliographical review, offering a concise overview of the history of gas sensors. It defines gas sensors, discusses various types of gas sensors, explores their working mechanisms, examine characterization parameters, and delves into impedance spectroscopy and analytical methods used in the study of sensor sets.

2.1 HISTORICAL OVERVIEW

Gas detection has a long history dating back to the Industrial Revolution, when coal miners needed to determine the presence of methane gas in the mines where they worked. The challenge was that methane gas is colorless and odorless, making its detection difficult. Initially, miners used humans as portable gas leak detectors by having them wear wet blankets and carry lit wicks to ignite methane pockets in mine walls. However, this method proved dangerous, prompting the exploration of alternative approaches[32,33].

One such method involved using canaries as indicators of gas presence. Miners brought canaries into mine tunnels and monitored their behavior. If a canary showed signs of distress or stopped chirping, it indicated the presence of methane and the need for immediate evacuation[32–34]. While this method reduced human casualties and provided a visible and audible gas detection method, there was still room for error.

Flame lights, as shown in Figure 4a, were introduced as a technological advancement in mine gas detection. Miners ignited a flame in an area with fresh air and observed its behavior to assess atmospheric conditions. A reduction in the flame indicated low oxygen levels, while an increase in size signaled the presence of methane mixed with oxygen, necessitating evacuation. However, flame lights were not universally applicable to all industries[32–35].

In 1926, Dr. Oliver Johnson invented the first modern gas detector—a catalytic sensor capable of detecting combustible elements in the atmosphere. This portable gas detector burned the gas inside it, providing a reading of the gases present. Although it required manual operation by pressing a button for a new reading, it represented a significant safety advancement for miners[35].
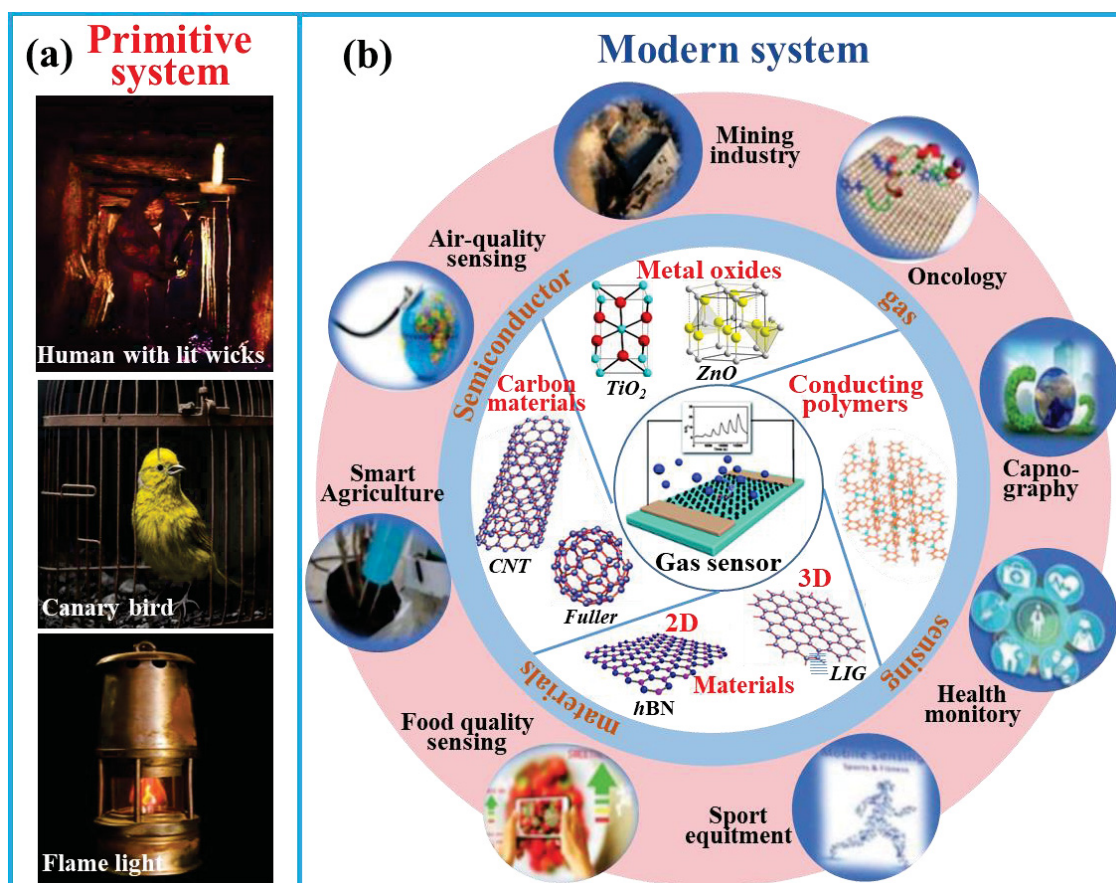
Figure 4 – Evolution of gas sensors. Based on Padvi (2021)[34], Nikolic (2020)[36] and Dariyal (2021)[37].

Semiconductor materials played a crucial role in the development of gas detection technology. In 1952, researchers Brattain and Bardeen[38] explored the gas-sensitive effects of germanium, marking its use as the first semiconductor material for gas detection. Further research in 1954 by Heiland[39] revealed the influence of changes in gas partial pressure on the semiconducting properties of zinc oxide. These findings laid the foundation for the development of chemoresistive gas sensors.

During the early 1960s, Seyama[40] demonstrated the feasibility of gas sensing using electrical devices. By employing a thin film of zinc oxide as a sensing layer operating at high temperatures, chemoresistive sensors exhibited significantly higher responses to gases such as propane compared to previous thermal conductivity detectors.

In the early 1970s, Taguchi[41] introduced the first practical chemoresistive gas sensor device, utilizing tin dioxide as the sensitive material and incorporating palladium as a metal catalyst to enhance sensitivity, selectivity, and stability. These devices, commercialized by Figaro Inc., found applications as alarms in residential settings to monitor the presence of explosive gases and prevent accidents and fires. This marked the widespread application of semiconductor gas sensors[36].

In the late 1980s, the field of semiconductor gas sensors underwent significant expansion, emerging as one of the most active research areas in the sensor community. The demand for high-performance gas sensors with enhanced sensitivity, selectivity, faster response times, lower power consumption, and improved device reliability fueled extensive efforts to develop novel sensing materials (Figure 4b). This led to the exploration of conducting polymers as viable options. In the early 2000s, the focus shifted towards carbon structures, and subsequently, research delved into the investigation of their composites. More recently, there has been a growing interest in the utilization of 2D materials for gas sensing applications[36]. As the cost and performance of electronic gas sensors improved over time, these sensors found integration into various systems, including industrial emission control, environmental monitoring, household security, vehicle emission control, agriculture, biomedical applications, and more[42,43].

This overview of the history of gas sensors not only adopts a chronological approach to delve into the past but also uncovers crucial concepts, emerging materials, and cutting-edge technologies.

2.2 FUNDAMENTS OF DEVICES AND SENSING MATERIALS

2.2.1 Definition of gas sensor

Gas sensors are chemical sensors that operate based on the principle of adsorbing gas onto the surface of the active material[44]. This process enables them to detect and transform chemical information, including concentration, pressure, particle activity, and more, into a useful electrical signal[45,46]. Sensors typically consist of two main components: the **sensing material** (or receptor) where the molecular recognition takes place and the **transducer** that allows the measurement of interaction events between the analyte in a gaseous phase and the solid-state sensitive layer[10,47]. The analytes interact with the sensing material, leading to changes in its physical properties such as temperature (ΔT), mass (ΔM), conductivity ($\Delta \sigma$), work function ($\Delta \Phi$), refractive index (Δn), and permittivity ($\Delta \varepsilon$). On the other hand, the transducer is an electric device that converts one of these physical quantities into a variation in its electric parameter, which can include capacitance (ΔC), inductance (ΔL), and resistance (ΔR) as shown in Figure 5. Finally, the sensing signal is generated by the circuit to which the sensor is connected[27].
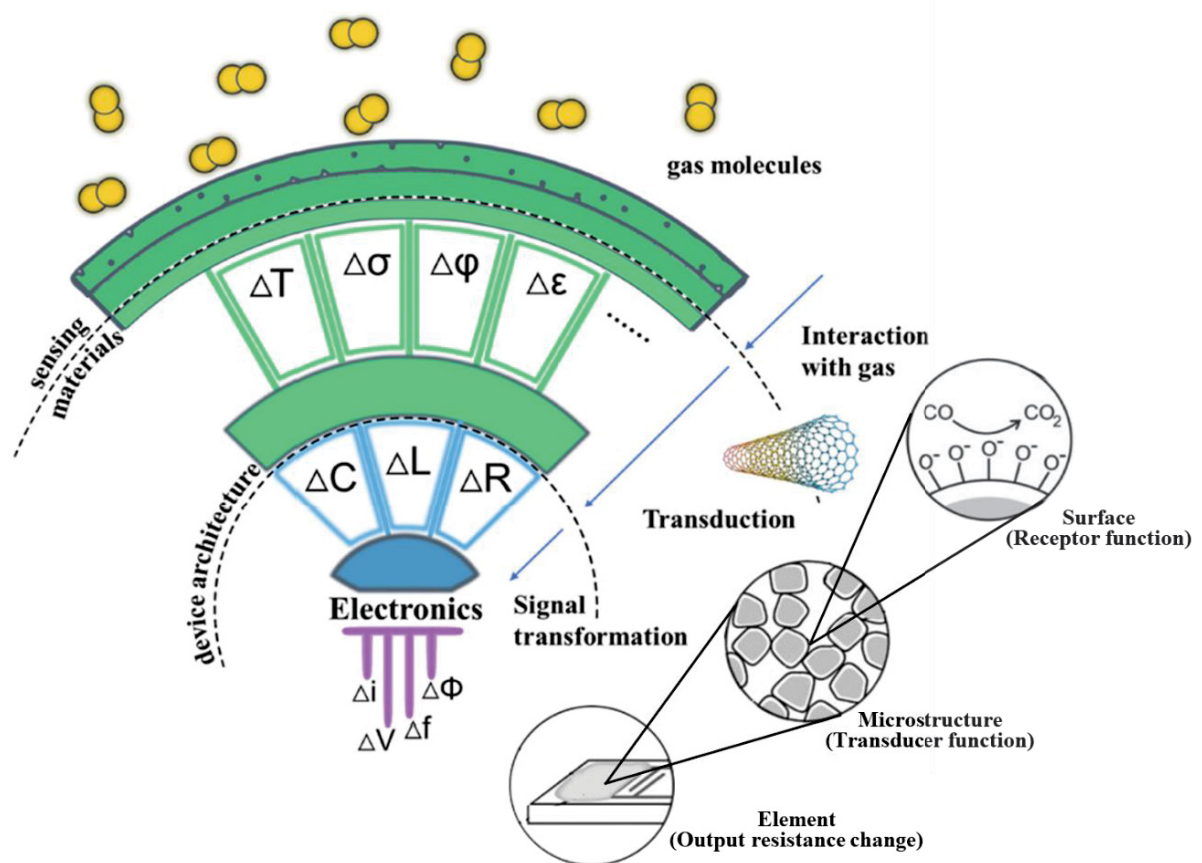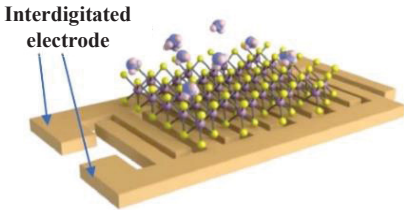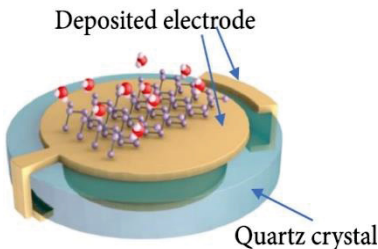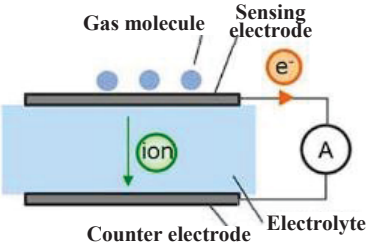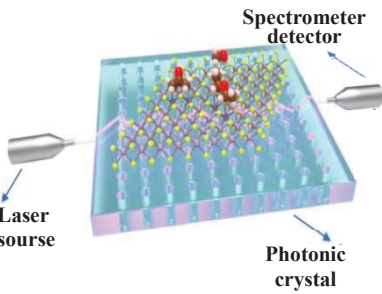
Figure 5 – Logical structure of a chemical sensor[48,49].

2.2.2 Classification of gas sensors

Gas sensors can be classified based on their operating mechanism, as proposed by Amuzuvi et al.[33] Nonetheless, despite the abundant possibilities that chemistry offers for assembling diverse receptors, the principles available for electronic transducers are relatively limited. They are typically categorized into four main groups, each corresponding to the measurement of a specific physical quantity influenced by molecular recognition events. These categories include chemoresistive, mass transducer, electrochemical, and optical sensors[27]. Table 1 shows a brief description for each category.

TABLE 1 – Operating principle of categorized sensors.

Sensor platform[50]	Operating principle
Chemoresistive Interdigitated electrode	The chemoresistive sensors are the most basic and straightforward electronic components to integrate into electronic systems[27]. The fabrication process is relatively simple: the sensing material is deposited between two parallel electrodes on an insulating substrate. To regulate the overall resistance, an interdigitated pair of electrodes is often employed, allowing modulation based on the presence or absence of the analyte. Chemoresistors have been developed using a diverse range of structures, including metal oxides, conductive polymers, organic and inorganic materials, as well as composites. It is worth emphasizing that this particular type of sensor holds a central focus in the thesis at hand[51–53].
Quartz Crystal Microbalance Deposited electrode Quartz crystal	Mass sensors are specifically designed to detect changes in the mass of the active layer resulting from interactions between chemical species and the sensor. One notable example is the Quartz Crystal Microbalance (QCM), which consists of a quartz crystal positioned between two parallel metal electrodes. The QCM leverages the piezoelectric property of the quartz crystal, causing it to oscillate when a voltage is applied across the electrodes. The operating frequency of the QCM device is dependent on the velocity of the wave and the thickness of the crystal. By coating the electrodes with a selective material, the QCM can effectively target specific analytes. When exposed to an analyte, the operating frequency of the QCM device undergoes a shift that corresponds to the type and concentration of the target molecules[54,55].
Electrochemical Gas molecule — Sensing electrode ion Counter electrode — Electrolyte	The fundamental components of an electrochemical sensor consist of a working electrode (or sensor), a reference electrode, and a counter electrode. These electrodes are positioned within the sensor enclosure and contact a liquid electrolyte. The operating principle relies on the diffusion of gas through a permeable electrode, leading to an interface with the cell's electrolyte. At this interface, electrochemical reactions occur, resulting in modifications to the electrical characteristics of the electrode[35]. Electrochemical sensors are categorized into potentiometric (energy conversion), voltammetric (limiting current), and conductimetric types (resistive)[45,46].
Optical Spectrometer detector Laser sourse Photonic crystal	In optical chemical sensors, the analyte is identified by monitoring changes in the optical properties of a sensitive material. Optical transduction techniques encompass various methods such as optical absorption, luminescence, colorimetry, and refractive index variation. One fascinating type of optical sensor is the crystal photonic sensor, which utilizes materials with a periodic refractive index pattern. The periodicity of the refractive index creates a forbidden region for certain frequencies, preventing the propagation of photons through the structure. This forbidden frequency region is known as a photonic bandgap (PBG). When exposed to external gases, the optical properties of photonic crystals, including the location of their PBG, can be readily modulated[56–59].

2.2.3 Gas-solid interaction

In this section, the fundamental physical and chemical processes occurring at the surface of a solid-state gas sensor are explored, with a particular focus on the dynamic motion of gas molecules (adsorption-desorption) and the sensing mechanism (band bending theory). Understanding these processes is essential for comprehending and substantiating the mechanisms observed in the gas sensors that have been fabricated and studied experimentally in subsequent chapters.

The dynamic behavior of gas molecules, including adsorption and desorption, is closely linked to the sensing process. In gas sensing, injected molecules diffuse rapidly throughout the test chamber. Some of these molecules are adsorbed onto the sensing layer, causing variations in resistance or conductivity, known as "response." Desorption, on the other hand, is the reverse process where adsorbed molecules are released back into the gas phase[60]. The gas-sensing mechanism in resistive-based sensors relies on structure morphology[61,62]. A higher surface area provides more adsorption sites, enhancing gas response. The active layer contains free electrons in the surface conduction band, influenced by factors like defects, bandgap, thermal activation, doping, vacancies, interstitials, oxygen partial pressure[55]. The power law theory for MOS gas sensors, proposed by Yamazoe et al.[63], integrates the depletion layer theory with gas adsorption and reaction. According to this theory, the resistance of a MOS material exposed to a specific gas with partial pressure P is proportional to P^n, where n is a constant for a specific target gas[60].

Adsorption

Adsorption processes are of utmost importance in the sensing mechanism of gas sensors. They play a critical role in determining several key parameters of the sensor device, including sensitivity, limit of detection, selectivity, as well as response and recovery time. When gas molecules come into contact with a solid surface, they can either remain adsorbed or undergo desorption, depending on factors such as temperature and the binding energy with the surface. During the adsorption process, gas molecules (referred to as adsorbate) interact with the surface of the solid (known as adsorbent), forming bonds between the two components. This process can be categorized into two main types: physisorption and chemisorption[64].

Physisorption arises from weak intermolecular forces, like Van der Waals interactions, and represents a reversible process. The adsorbed particles in physisorption exhibit low binding

energy, rendering them easily desorbable. Generally, physisorption occurs at lower temperatures compared to chemisorption[65]. As an instance, in metallic oxide semiconductors (MOS), oxygen (O_2) undergoes physisorption at temperatures below 150°C, leading to the formation of physisorbed oxygen (O_2^-). In this state, the physisorbed molecule is consistently maintained at a greater distance than it would be in the event of a chemical bond, typically exceeding four bonding lengths[66].

In contrast, chemisorption involves stronger bonding forces such as ionic, covalent, or hydrogen bonds. It necessitates a higher energy input to achieve equilibrium or the system's minimum energy state compared to physisorption. During chemisorption, there is a rearrangement of electrons between the gas and the solid, resulting in the formation and breaking of chemical bonds. This process can also trigger chemical reactions, such as oxidation when the solid surface interacts with oxygen. Unlike physisorption, chemisorption is not limited by temperature and can occur over a broader temperature range. In the case of oxygen species, they chemisorb onto the surface as chemisorbed oxygen (O^- or O^{2-}). The kinetics of this process can be described using adsorption kinetics principles, as outlined below[17,66–70].

$$O_2 \text{ (gas)} \leftrightarrow O_2 \text{ (absorbed)} \tag{2.1}$$
$$O_2 \text{ (adsorbed)} + e- \leftrightarrow O_2^- \text{ (physisorbed)} \tag{2.2}$$
$$O_2^- \text{ (adsorbed)} + e- \leftrightarrow 2O^- \text{ (chemisorbed)} \tag{2.3}$$
$$O^- \text{ (adsorbed)} + e - \leftrightarrow O^{2-} \text{ (chemisorbed)} \tag{2.4}$$

When the sensor is exposed to VOC gases (such as formaldehyde, ethanol, acetone, methanol, and others), the adsorbed oxygen ion species react with VOC gas molecules on the sensing layer's surface, leading to the formation of CO_2 and H_2O. This reaction causes the trapped electrons to be released back to the conduction band of the sensing layer. As a result, the thickness of the space-charge layer and the potential barrier decrease. The reaction can be represented as follows[71]:

$$VOCs \text{ (gas)} \leftrightarrow VOCs \text{ (adsorbed)} \tag{2.5}$$
$$VOCs \text{ (adsorbed)} + Ox^- \leftrightarrow CO_2 + H_2O \text{ (g)} + e^- \tag{2.6}$$
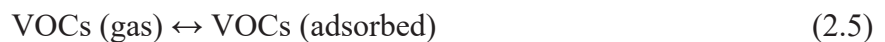
On the other hand, the adsorption of particles, which refers to the quantity of adsorbate on the surface of the adsorbent, can be accurately described using adsorption isotherms based on various models at a constant temperature. Commonly used isotherms include Henry's

adsorption isotherm, Freundlich equation, Langmuir equation, and Brunauer-Emmett-Teller (BET) theory. Langmuir's adsorption isotherm, in particular, is widely utilized[72] and has been explained elsewhere[73].

The sensing mechanism

Gas sensors based on semiconductors are categorized as n-type and p-type sensors, depending on the majority charge carriers (electrons or holes). Both n-type and p-type semiconductors exhibit adsorption of oxygen molecules on their surfaces[66]. The sensing mechanism of n-type and p-type MOS sensors in the presence of an oxidizing gas can be explained through the formation of an electronic core-shell configuration, as depicted in Figure 6. In the case of n-type semiconductors, the cores of particles represent the n-type semiconducting region, while the shells exhibit a resistive electron depletion layer (EDL) (Figure 6a,b). On the other hand, the adsorption of oxygen anions on p-type oxide semiconductors leads to the formation of a hole accumulation layer (HAL) near the material's surface due to electrostatic interaction between the oppositely charged species[74].
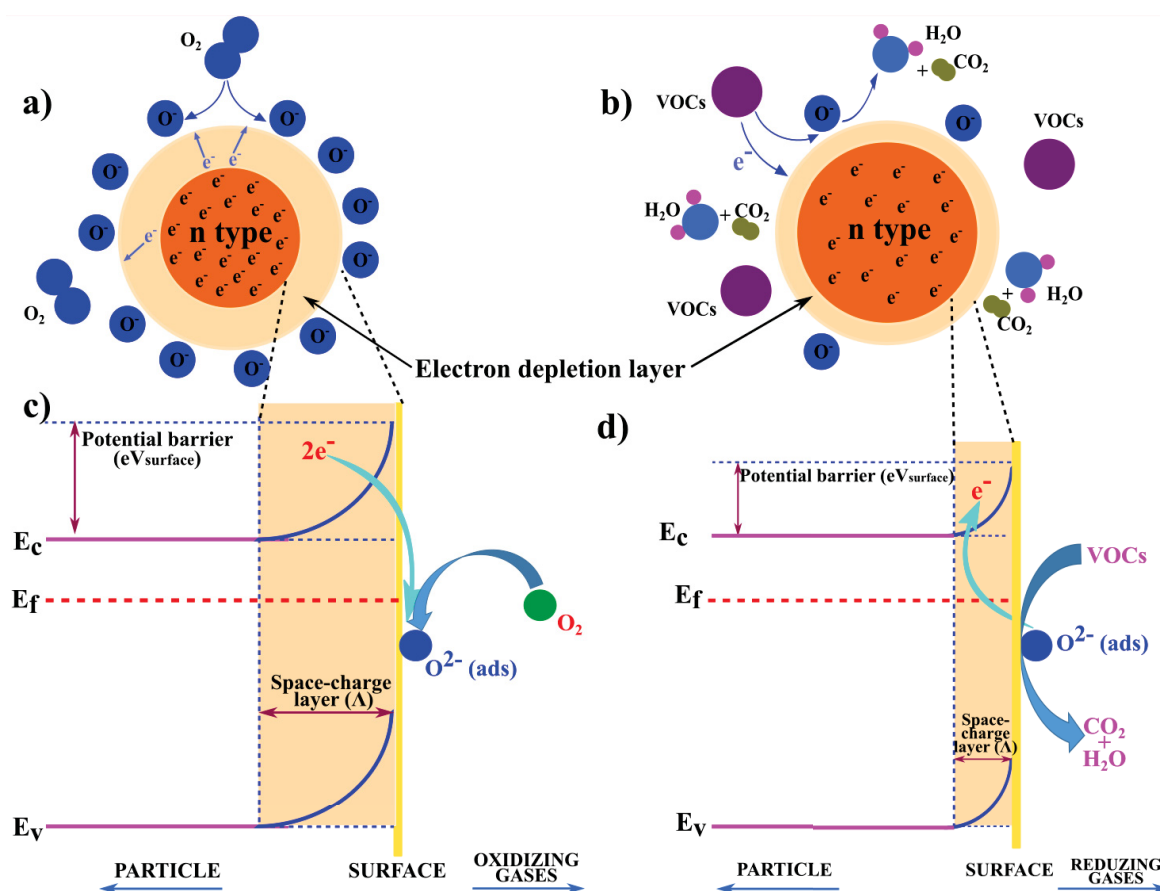
Figure 6 – Schematic diagram of gas-sensing mechanism and energy band levels of n-type semiconductors-based sensor in air (a,c) and VOCs (b.d). E_c, E_v, and E_f denote the energy of the conduction band, valence band, and the Fermi level, respectively [54,69–73,75,76].

The sensing mechanisms can be understood by applying the band bending theory[75]. When the active layer is exposed to an ambient atmosphere containing various gases, oxygen tends to preferentially adsorb onto the surface. This leads to an electron flow from the semiconductor to the oxygen molecules, causing the extraction of electrons from the conduction band (E_c) and their trapping as ions on the surface. Consequently, a negatively charged oxygen molecule forms on the semiconductor, resulting in upward band bending and an increased potential barrier at the grain boundaries. This alteration in the band structure results in reduced conductivity compared to the flat band situation, as illustrated in Figure 6c. The region depleted of electrons is known as the space-charge layer, and its thickness corresponds to the length of the band bending region.

In the presence of reducing gases, such as VOCs, the interaction of these oxygen species can initiate various processes, including reactions, competitive adsorption, or replacement of the adsorbed oxygen by other molecules. This can decrease or even reverse the band bending, leading to increased conductivity compared to the initial state, as shown in Figure 6d[76–80].

During the sensing process, the resistivity change in the active layer is influenced by its intrinsic physical properties, such as the type of semiconductor and, consequently, its bandgap (E_g), as well as the properties of the target gas[81], as illustrated in Figure 7. In **n-type** semiconductors, exposure of the surface to an **oxidizing** gas leads to the extraction of free electrons, depleting the majority charge carriers and resulting in **increased sensor resistance**. Conversely, in a **reducing** gas environment, the width of the electron depletion layer decreases, leading to a **reduction in sensor resistance**. On the other hand, in **p-type** semiconductors, the scenario is reversed. When the **oxidizing** gas captures the free electrons (which are minority charge carriers in this case), the number of holes (majority charge carriers) increases, thereby **enhancing conductivity** upon oxygen adsorption. However, for **reducing gases**, the opposite occurs, and the **resistance increases**[82]. Table 2 provides examples of oxidizing and reducing gases.

TABLE 2 – Sensing Response in n-Type and p-Type Materials towards Reducing and Oxidizing Gases[83].

Sensor-response behaviour	n-type	p-type	Example of target analyte
Oxidizing gas	Resistance increases	Resistance decreases	O_2, O_3, NO_X, CO_2, SO_2
Reducing gas	Resistance decreases	Resistance increases	H_2, H_2S, CO, NH_4, **Ethanol, Acetone**, CH_4
Dominant-charge carrier	Electrons (e-)	Holes (h+)	-
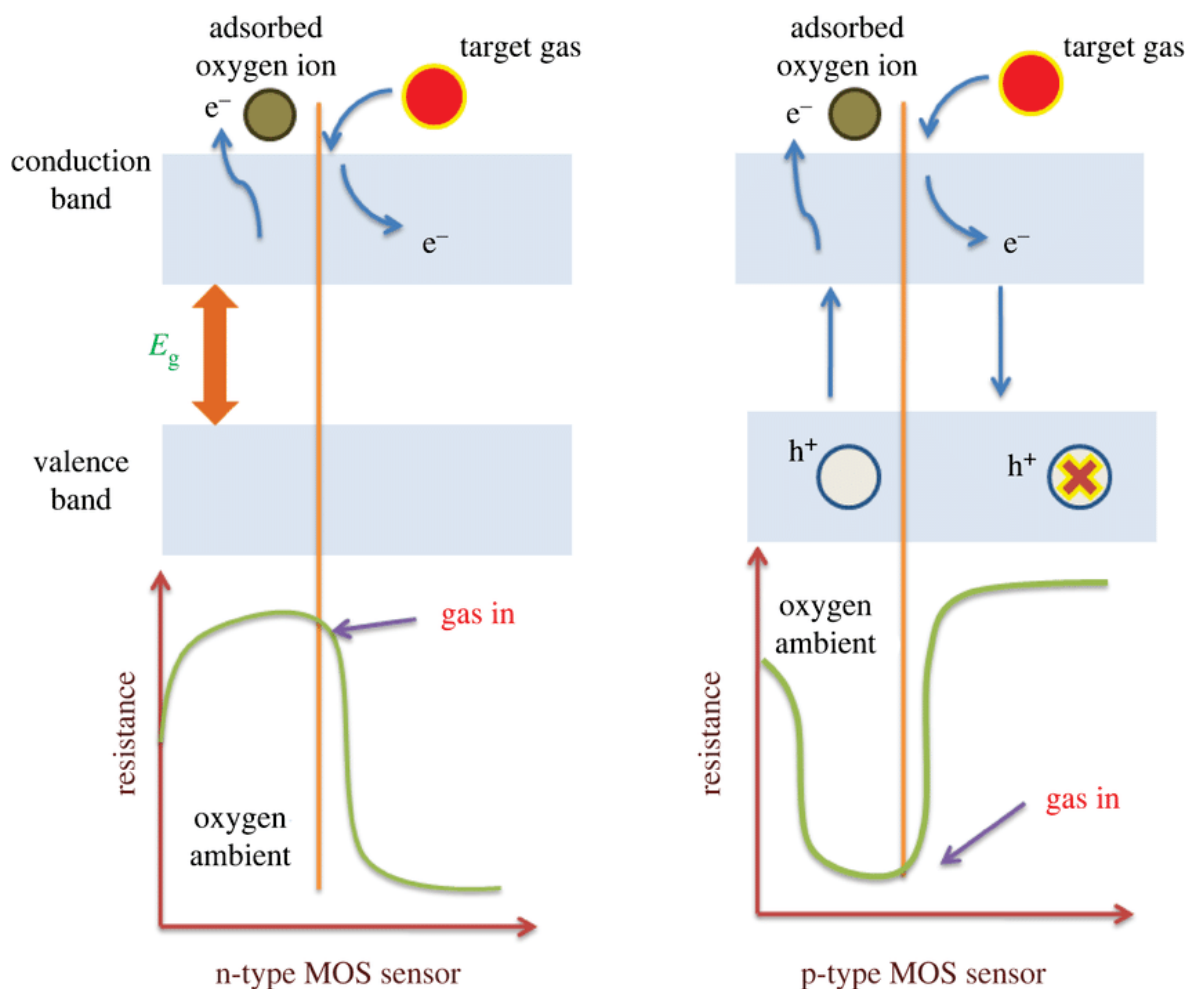
Figure 7 – Diagram of the sensing mechanism for resistance change in n-type and p-type MOS Sensors upon exposure to a reducing gas. E_g denotes the energy band gap[79,84].

Although the sensing mechanism of semiconductor sensors primarily involves surface adsorption of oxygen ions; the sensing process is not limited to oxygen adsorption and mainly relies on charge transfer. The sensing film acts as a donor or acceptor of charges during the charge transfer process with the adsorbed gas molecule. As different gases can exchange charges with the sensing material, it is the magnitude of charge exchange that determines variations in the conductive properties of the film. This characteristic enables the classification of gas sensor specificity based on the extent of charge exchange[52,53].

2.2.4 Nanostructured materials

Nanostructured sensors utilize materials composed of nanosized building blocks (Figure 8), exhibiting many interesting features, such as quantum effects, the possibility of surface functionalization, tunable porosity and a surface-area-to-volume ratio greater than that of bulk materials. Consequently, their behaviour significantly diverges from that of bulk materials,

resulting in enhanced chemical reactivity, as well as improved mechanical, optical, electrical, and magnetic characteristics. These nanostructured materials can be classified into carbon-based nanomaterials (fullerenes, carbon nanotubes, carbon nanofibers, carbon black, graphene, and carbon onions), inorganic nanomaterials (metals, metal oxides, and ceramic nanomaterials), organic-based nanomaterials (micelles, dendrimers, polymersomes, hydrogels, nanoconjugates), and composite nanostructures (hybrid nanofibers and metal-organic frameworks) based on their chemical composition[85,86].

In recent years, significant attention has been devoted to 2D materials for further enhancing gas-sensing performance. Extensive research has been conducted on atomically thin-layered materials such as graphene, boron nitride, molybdenum disulphide, black phosphorus, and tungsten sulphide. These materials offer a substantial surface-to-volume ratio, excellent signal-to-noise ratio, and high chemical stability. The ultrathin-layered structure of these materials restricts current paths, with the surface response to target gases directly influencing their gas-sensing properties[66].
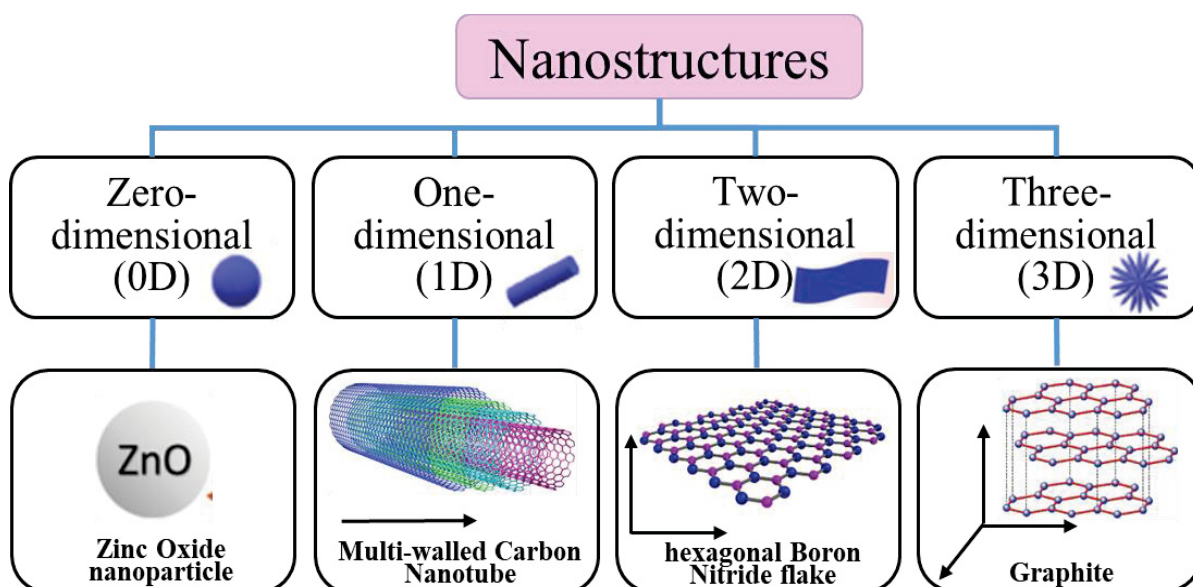
Figure 8 – Relationship between 0D, 1D, 2D and 3D morphologies with nanostructures employed in this study. Based on Franco (2022)[8].

The subsequent chapters of this study focus on hexagonal boron nitride (*h*BN), laser-induced graphene (LIG), zinc oxide (ZnO), and multi-walled carbon nanotubes (MWCNTs) as applied to gas sensors. These chapters delve into the specific characteristics and properties of these materials, providing valuable insights into their roles in gas sensing applications.

2.3 SENSOR PERFORMANCE EVALUATION

It is usually necessary to use some specific indicators to evaluate the gas-detection ability of a sensor[87]. An ideal gas sensor needs to have the following features: high sensitivity to low gas concentrations, repeatability, the lowest detection limits, rapid response, reversible operating ability, good selectivity to different gases of interest, low-manufacturing cost, stable operation over many cycles of use, and low power consumption during operation[48,88] Next, we present an overview of these parameters considering their characteristics and particularities.

2.3.1 Sensor response

The response (R_{es}) of a gas sensor to a specific analyte is crucial for its practical application. If a gas sensor fails to detect the target gas, it becomes impractical. The response is commonly described as the change in the electrical behavior of the sensing film after exposure to the analyte, compared to its initial electrical behavior without gas exposure (Figure 9). Traditionally, there are three formulas used to calculate this parameter: $(R_f - R_0)/R_0 \times 100$, R_f/R_0, and in this study, the relative resistance variation approach, as shown in equation 2.7, was utilized[8,55].

$$R_{es} = \Delta R/R_0 \tag{2.7}$$

where,

$\Delta R = R_f - R_0.$

R_f = the resistance of the sensor when exposed to analyte.

R_0 = the resistance of the sensor in inert atmosphere (N_2) or background gas.
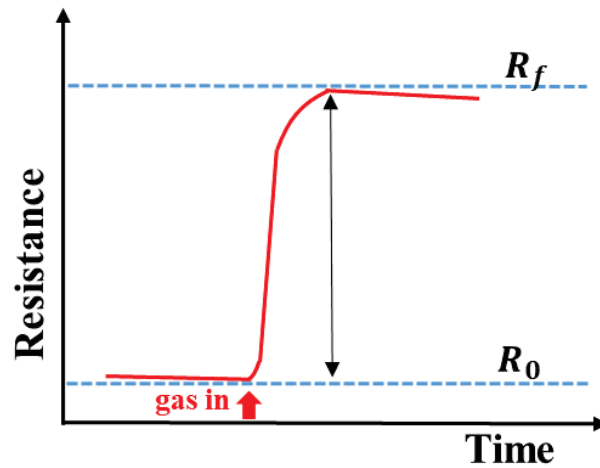
Figure 9 – Graphical representation of response[8].

2.3.2 Sensitivity

Sensitivity represents a measure for evaluating the fluctuation of gas target concentration values in the surrounding environment. It was determined by the change in measured resistance corresponding to a change in the concentration of the injected analyte (the substance being measured). The slope of the sensor's calibration curve is commonly used to estimate sensitivity[89] as shown in Figure 10.

The calibration curve illustrates the variation in the response as the concentration of the analyte changes. To capture the trend in the data, the curve is adjusted by fitting a mathematical model that represents the relationship between the variables[90].
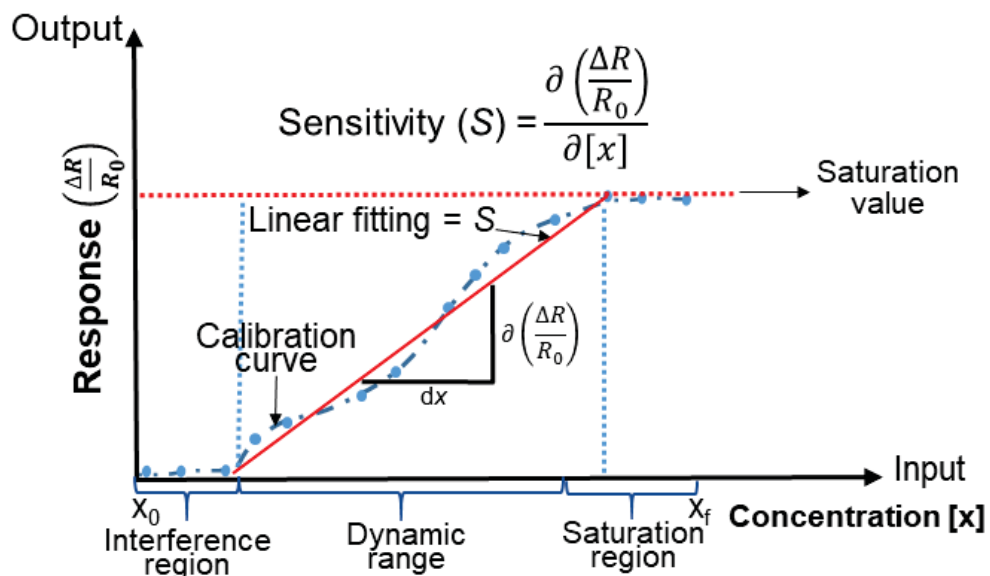
Figure 10 – Calibration curve example (with offset). Based on Janata[91] and Webster (1999)[90].

According to the site-binding hypothesis, atoms present on the surface of the sensing material serve as binding sites for analyte adsorption. Consequently, the conductance change of the device is directly linked to the extent of analyte molecule occupation on the sensing material's surface[92]. To enhance sensitivity, it is advantageous to introduce additional binding sites for the analyte[48].

2.3.3 Selectivity

It's usually defined as the ability of a sensor to recognize and measure an electrical response for a target gas without interference from non-target gases in multigas environments[87]. Selectivity can be mathematically defined as the ratio between the responses of a target gas and the responses to an interferent[93]. Besides, the graphical representation can be in terms of dynamic curve of sensor response (Figure 11a) or bar charts of sensor response for target analyte and interferents (Figure 11b)[8].

A high selectivity corresponds to a higher response of the gas sensor to a target gas compared with the response to interfering gases[94]. Typically, gas sensors are sensitive to more than one gas and exhibit cross-sensitivity. Hence, obtaining a high selectivity in a gas sensor is difficult, which limits the practical applications of gas sensors[95]. In order to find a solution to this problem of selectivity, an arrangement of sensors and analysis tools will be used in this study.
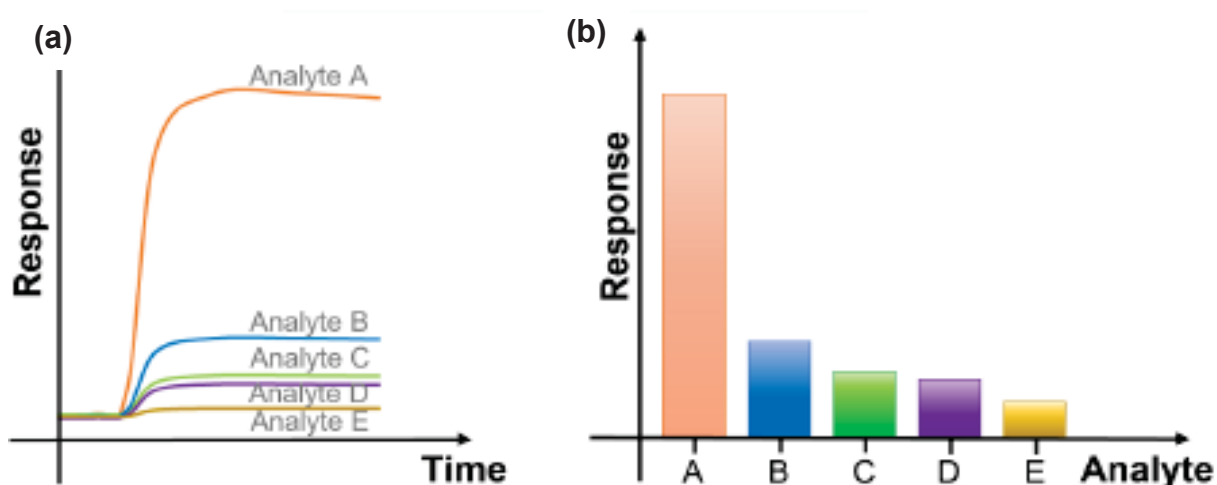
Figure 11 – Graphical representation of selectivity[8].

2.3.4 Limit of detection (LOD)

The LOD refers to the lowest concentration of analyte detectable by the sensor, thereby producing an instrument response under specific operating conditions, distinguished statistically from the response recorded for the blank sample (without the analyte)[96]. Calculating the LOD involves determining the critical level (L_C), which is obtained by adding the response of the blank to three times the standard deviation of the same blank (equation 2.8[97]). This L_C value allows us to discern the presence of the analyte in a sample after measurement. If the response to the analyte exceeds L_C, it indicates the presence of the analyte[98]. Finally, the LOD is determined by the intersection of the L_C with the slope of the sensor's analytical calibration curve.

$$Lc = X_b + 3\sigma_b \qquad\qquad (2.8)$$

where,

X_b = mean response of the blank, (blank is the response at zero concentration of a target gas, i.e., just in carrier gas or inert atmosphere).

σ_b = standard deviation of the blank.

2.3.5 Response and recovery time

The response time of a sensor indicates the duration taken by the sensor to provide a response after being exposed to the analyte. This parameter is often quantified using a percentage of sensor response. It is commonly reported as the time required to reach 90% of its steady state[99–101], which is the maximum value upon exposure to a specific concentration of the analyte, as depicted in Figure 12. Understanding the response time is crucial for assessing sensor performance, as it provides insights into the kinetics and magnitude of the interaction between the sensing layer and the target gas. However, external factors such as temperature, gas concentration, and flow rate during the experiment can influence this parameter [36,56,86,99].

On the other hand, the recovery time pertains to the opposite process of the response time. It refers to the time needed for the sensor to return to its original baseline response after the target analyte is removed, and the sensor comes into contact with a pure carrier gas, typically air or nitrogen[102]. In some cases, the term T10 is used, which denotes the time required for a 90% recovery[99–101], as shown in Figure 12. Frequently, a fast response time may be

accompanied by a slow recovery time due to chemical adsorption. To enhance gas desorption behavior, treatments like UV irradiation and heating are often employed[66].
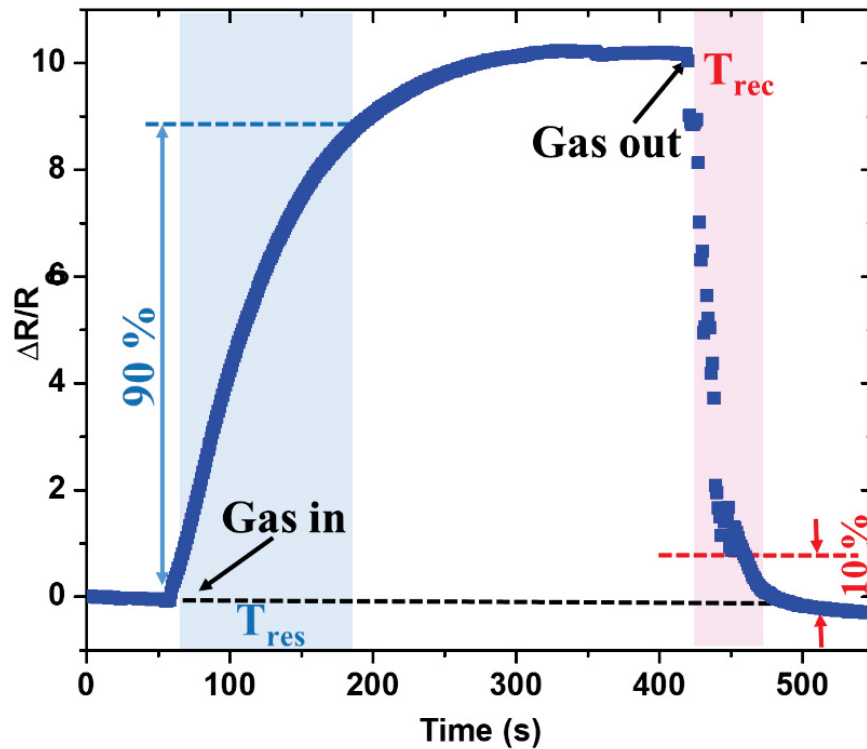
Figure 12 – The response and recovery time of a typical gas sensor[30,103].

2.3.6 Repeatability

Repeatability refers to the sensor's capability to restore its response to the original value and maintain its high sensing performance after measuring the target gas. If the sensor fails to regain the response value in a normal gas environment, it suggests that the target gas might have caused irreversible damage to the sensor, rendering it non-functional[104].

2.3.7 Stability

Stability can be defined as the repeatability over extended periods of time[105]. In other words, long-term stability refers to the sensor's capability to maintain or approximate its initial performance within the specified operating range over an extended duration[106]. Typically, the stability of a prepared sensor is assessed by measuring its response over one or several months, ensuring a consistent and reliable performance (Figure 13).
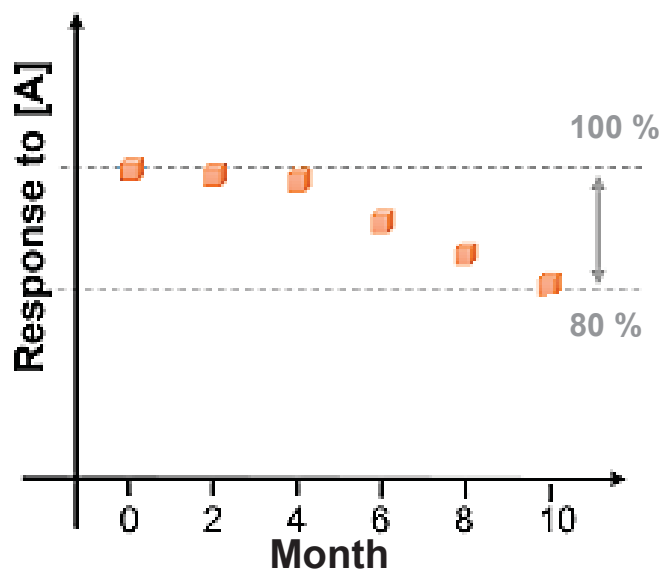
Figure 13 – Graphical representation of the long-term stability of the sensor[8].

2.3.8 Reproducibility

Reproducibility refers to the ability to fabricate multiple sensors that are identical and exhibit consistent responses to a target analyte. However, achieving reproducibility can be influenced by various factors during the development stages. These factors encompass batch-to-batch variations in device construction, challenges in attaching the active materials to the substrate, and variations in the preparation of sensing materials. Interestingly, it is important to note that reproducibility is sometimes overlooked or not emphasized in gas sensor publications, consequently neglecting the significance of consistent and predictable results[107].

2.4 FUNDAMENTALS OF IMPEDANCE SPECTROSCOPY (IS)

Impedance spectroscopy (IS), also known as AC impedance spectroscopy, is a non-destructive and versatile characterization technique used to monitor electrical and electrochemical changes in a system. It provides valuable kinetic and mechanistic information about the process and profiles the electronic structure in electrochemical and solid-state devices. In more detail, during IS analysis, as the target gas is introduced to the sensing unit, a range of reactions can occur on the device, which involve changing sensing materials[108]. IS facilitates quantitative analysis of these dynamic processes and complex interfaces. Consequently, it finds extensive applications in sensor studies for evaluating electron-transfer properties and investigating interfacial chemical transformations that take place on modified surfaces. These

transformations can be attributed to adsorbed species such as ions, organic compounds, and water molecules, as well as diffusion processes (Warburg factor)[109]. By examining these parameters, researchers are able to predict suitable gas sensing mechanisms and gain insights into the behavior of gas sensors.

2.4.1 Basics

The impedance spectroscopy method typically involves applying a low-amplitude sinusoidal potential modulation (AC voltage) at different frequencies to evaluate the response of a system.[109] This response is measured as a sinusoidal current, $I(t)$, which shares the same frequency (ω) and intensity as the applied potential, as one wave leads to the other. However, a crucial effect known as the phase-angle shift (θ) occurs, resulting in a constant time shift between the two waves at a specific angle. The phase-angle shift can vary from –90° to 90° degrees[110]. The relationship between the voltage and current is illustrated in Figure 14.

The mathematical approach of electrochemical impedance data relies on the application of Ohm's law, which describes the linear relationship between potential perturbation and current response, or vice versa. However, it is important to note that the potential-current dependencies of electrochemical systems, in general, exhibit non-linear behavior. Nonetheless, it is possible to extract a small portion of this dependence in which the relationship can be approximated as linear. This approximation is typically valid when the AC voltage applied has a small amplitude[111]. Similar to physical electric circuits, the electrochemical impedance (Z) is defined in equation 2.9.

$$Z(\omega) = \frac{V_{ampl}}{I_{ampl}} \qquad (2.9)$$
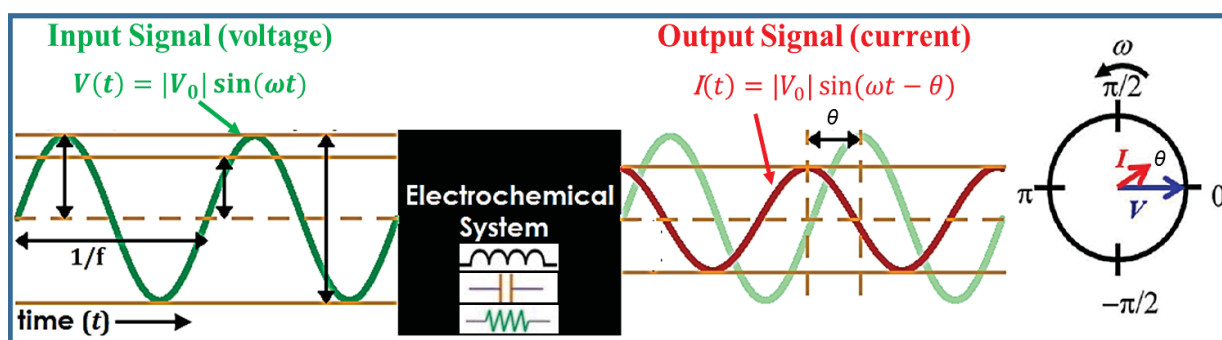
Figure 14 – Relation between sinusoidal input voltage at a single frequency and output current in the time domain delayed by phase shift, θ[112].

where V_{ampl} and I_{ampl} represent the amplitudes of potential and current, respectively, In polar coordinates, these functions are depicted as vectors of length $|V_0|$ and $|I_0|$, rotating counterclockwise at the radial frequency ω, where $\omega = 2\pi f$ denotes the radial frequency in rad/s (f being the frequency in Hz). Describing these functions becomes more straightforward when complex numbers are employed[111]. $V(t)$ and $I(t)$ can be modified by using the complex function $j = \sqrt{-1} = exp\left(\frac{j\pi}{2}\right)$[112].

$$V(t) = |V_0|\exp(j\omega t) \text{ and } I(t) = |I_0|\exp[j(\omega t - \theta)] \qquad \text{(2.10 and 2.11)}$$

The equation 2.9 is transformed:

$$Z(\omega) = \frac{V(t)}{I(t)} = Z_0 \frac{exp(j\omega t)}{exp(j\omega t - j\theta)} \qquad \text{(2.12)}$$

$$Z(\omega) = |Z_0| \exp(-j\theta) \qquad \text{(2.13)}$$

Equation 2.13 can be simplified using Euler's relationship, $\exp(\pm j\theta) = \cos(\theta) \pm j\sin(\theta)$.

$$Z(\omega) = |Z_0| \exp(-j\theta) = |Z_0|(cos\theta - jsin\,\theta) \qquad \text{(2.14)}$$

$$Z(\omega) = |Z_0|cos\theta - j|Z_0| \sin\theta \qquad \text{(2.15)}$$

In this context, equation 2.15 can be divided into real (Z_{Re}) and the imaginary part (Z_{Im}) of the impedance at a specific ω, as shown in equations 2.16 and 2.17. Where, the real and imaginary part of the impedance are denoted by $|Z|cos\theta$ and $|Z|sen\theta$, respectively[113].

$$Z_{Re} \equiv Z' = |Z|cos\theta \qquad \text{(2.16)}$$

$$Z_{Im} \equiv Z'' = |Z|sin\theta \qquad \text{(2.17)}$$

In the literature, it is also common to distinguish the real and imaginary parts of the impedance as Z' and Z'', respectively. Hence, the impedance extracted from equation 2.15 can be expressed as follows:

$$Z(\omega) = Z_{Re} - jZ_{Im} = Z'(\omega) - jZ''(\omega) \qquad \text{(2.18)}$$

The relationship between the rectangular and the polar form is shown in the Figure 15.
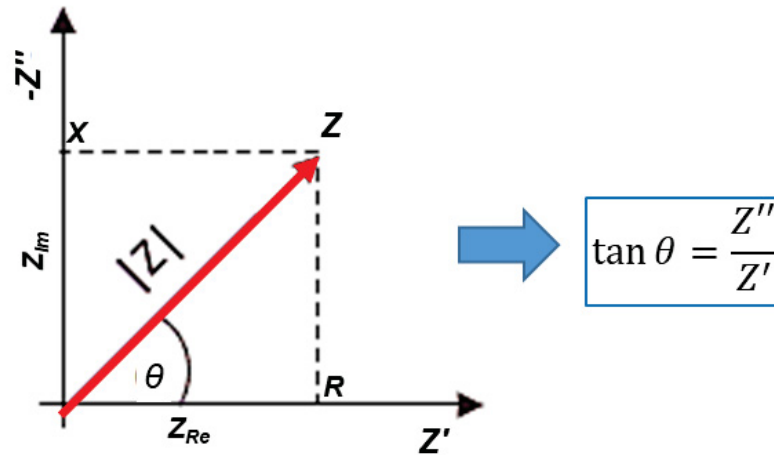
Figure 15 – Vector visualization of the complex impedance Z: Real and imaginary components, and phase angle θ[110].

The modulus of Z and θ are expressed by the following equations:

$$|Z| = \sqrt{(Z')^2 + (Z'')^2} \tag{2.19}$$

$$\theta = \arctan(Z''/Z') \tag{2.20}$$

2.4.2 Typical Spectra

IS is typically analyzed using graphical representations[114], such as the Nyquist plot (also known as a Cole-Cole plot or a complex impedance plane plot)[111] and Bode plots, as shown in Figure 16. The Nyquist plot illustrates the imaginary impedance component (Z'') plotted against the real impedance component (Z') at different excitation frequencies. On the other hand, Bode plots display the impedance modulus $|Z|$ and phase angle (θ) as functions of the logarithm of the applied frequency range[115].

On a Nyquist plot, impedances located near the origin on the X-axis correspond to the high-frequency spectrum. Conversely, at lower frequencies, their respective impedances are depicted on the right side of the plot[109].

The Nyquist plot offers advantages such as easy visualization of ohmic resistance effects and highlighting series circuit components. On the other hand, the Bode plot provides explicit frequency information and allows for a wide range of frequencies to be plotted on a single graph[116]. It can expedite measurements by extrapolating data from higher frequencies. However, the Bode plot is sensitive to changes in circuit values. Therefore, impedance spectroscopy data is commonly analyzed using both Nyquist and Bode plots to leverage their respective strengths and mitigate limitations[111].
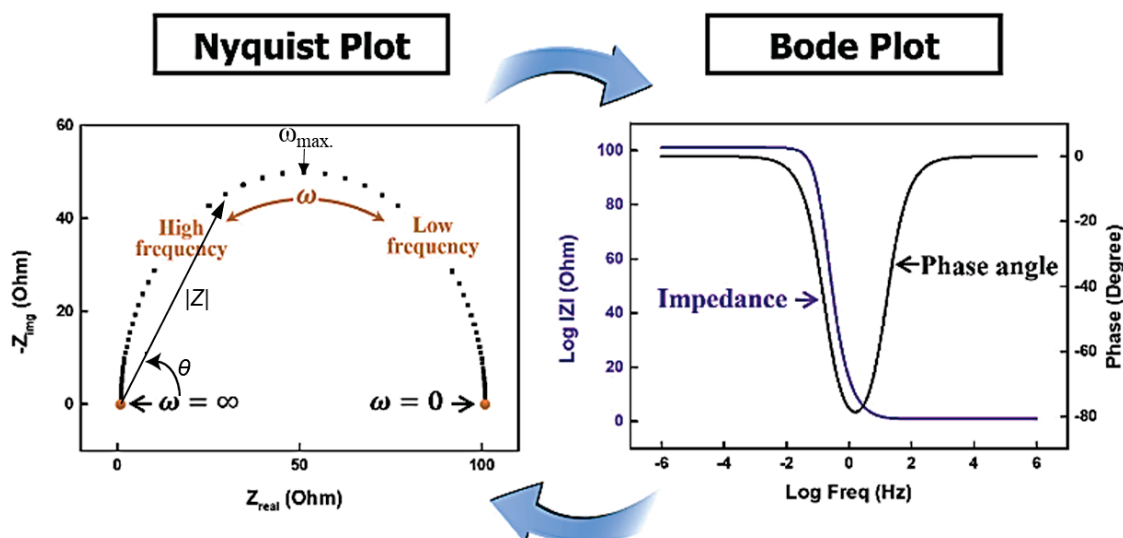
Figure 16 – Impedance Spectroscopy representation by Nyquist plot with one complex impedance value $Z(\omega)$ (left) and Bode plot (right)[112].

2.4.5 Equivalent circuits

IS data are typically modeled by fitting it to an equivalent electrical circuit, where the elements of the circuit are determined based on the Nyquist plot shape. The equivalent circuit represents the electrochemical processes involved and includes passive elements that do not generate current or potential such as resistors (R), capacitors (C), constant phase elements (CPE), inductors (L), Warburg impedance (W) and other elements. These elements are connected in different configurations, such as series or parallel, to quantitatively characterize the device properties and understand conduction mechanisms in gas sensors[111,112,115].

The characteristics of the Nyquist plot provide valuable insights into the underlying physical processes within the system. For example, when a line runs parallel to the y-axis, it indicates the presence of either a standalone capacitor (Figure 17a) or a capacitor in combination with a solution resistor (Figure 17b). The resistance value can be determined by examining the intercept on the x-axis. On the other hand, a semicircular Nyquist plot with an intercept at the origin (Figure 17c) suggests a circuit configuration involving a capacitor in parallel with a resistor. If an additional resistor is introduced in series, the semicircle shifts along the x-axis (Figure 17d), and the value of the series resistance can be determined from the displacement. By carefully analyzing the characteristics of the Nyquist plot and combining this information with knowledge of the device, it becomes possible to construct an accurate equivalent circuit model where each circuit element corresponds to a specific process[117].
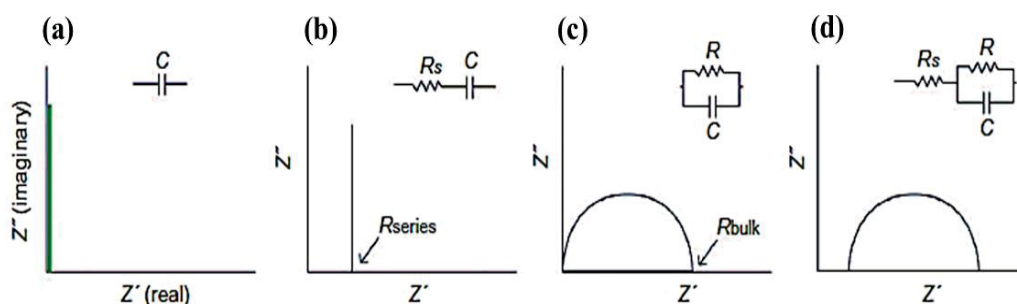
Figure 17 – Typical Nyquist plots for basic electrical circuits. (a) pure capacitor (*C*, only imaginary part of impedance); (b) *R* and *C* in series connection; (c) *R* and *C* in parallel connection; (d) The solution resistance (R_S) is connected in series with an *RC* circuit in parallel[109].
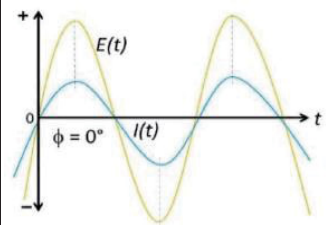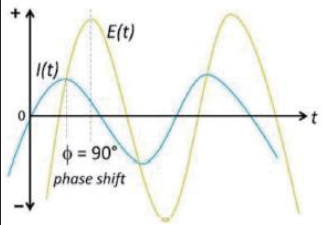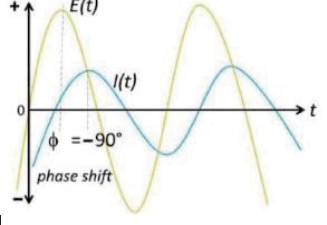
This approach has been widely applied to analyze various electrochemical systems, and existing literature models can serve as valuable starting points for analyzing specific systems. Regardless of the specific processes involved, such as metal deposition, corrosion, ion electroreduction, and nanostructure film formation, these systems exhibit common stages and processes. These include the formation of a double electric layer, the presence of ohmic resistance, charge transfer resistance in electrochemical reactions, the formation of adsorbed layers by intermediates, as well as diffusion phenomena in solutions and organic or polymeric films, among others. By employing equivalent circuits with different interpretations of passive elements, it becomes possible to simulate and gain insights into the diverse processes occurring within the system[118].

The resistance exhibits a purely real impedance, resulting in in-phase current and voltage. On the other hand, the impedance of a capacitor is purely imaginary and inversely proportional to frequency. This is due to the efficient displacement of charges by high-frequency alternating currents, while low frequencies are impeded by physical interfaces or energy barriers. The voltage waveform across a capacitor lags behind the current waveform by 90°. In contrast, the impedance of an inductor increases with frequency, and the voltage waveform leads the current waveform by 90°[119]. Table 3 includes these three elements[118].

The resistance element in an equivalent circuit model represents the movement of electrons through the lattice, specifically related to electrical or ionic transport processes such as conduction, charge transfer, and recombination. On the other hand, electrochemical capacitances in IS are linked to changes in the electrochemical potential of the system resulting from local charge rearrangement. Parameterizing these specific electrochemical capacitances in terms of material properties requires a deeper understanding of the electronic structure, as well as the electronic and ionic dynamics within the sample. Chemical capacitances can arise from various processes, including charge diffusion, chemical reactions, and carrier injection.

When modeling IS data, it is important to consider whether the electrochemical capacitances are connected in parallel or in series with other dynamics in the device, as this affects the overall behavior of the system[120].

TABLE 3 – Basic circuit elements used to model the physicochemical process[110].

Impedance element	R	C	L
Contribution to impedance	$Z = R$	$Z = 1/j\omega L$	$Z = j\omega L$
Phase angle	0°	90°	–90°
Frequency dependence	Constant	Inversely proportional	Directly proportional
Waveform signal			

Alternatively, a constant phase element is a distributed element that produces an impedance having a constant phase angle in the complex plane. A CPE is an empirical impedance function of the following form:

$$Z_{CPE} = \frac{1}{A(j\omega)^n} \qquad (2.21)$$

The Constant A determines the impedance modulus, while the exponent n determines the impedance angle, which ranges from 0° to 90°. In the special cases where $n = 1$ (90°), the CPE acts as an ideal capacitor with the capacitance equal to A, while at $n = 0$ (0°), the element behaves as an ideal resistor.

The CPE is employed when deviations are observed in the measurements. These deviations are often characterized by the center of the circle being depressed below the X-axis from the ideal semicircle, and they can be attributed to electron traps in the metal oxide, microstructural features such as grain size inhomogeneities, or a distribution of relaxation times[118].

CHAPTER 3

3 SENSORS BASED ON BAF₂-MODIFIED hBN FLAKES TOWARDS DETECTION OF VOLATILE ORGANIC COMPOUNDS

3.1 INTRODUCTION

The appropriate selection of a sensitive material is essential for gas sensors[76,121,122], and 2D materials such as graphene have been extensively studied for their unique properties and wide range of applications, including gas sensors[102,123–125]. Likewise, hexagonal boron nitride (hBN) belongs to the 2D materials family and shares many of graphene's properties due to its similar atomic structure. However, it differs in that its honeycomb lattice is formed by B–N bonds instead of C–C bonds[126–129]. Moreover, hBN nanosheets exhibit remarkable physicochemical properties, such as high mechanical strength, high thermal conductivity, and chemical and thermal stability. The partially ionic B–N chemical bonds and 2D nature of hBN nanosheets also provide excellent adsorption properties, resulting in a high surface/volume ratio that fully exposes hBN atoms to gas molecules, making it an attractive material for gas sensing applications[130–132].

Despite their potential, there is limited literature on the utilization of hBN nanosheets as a sensitive material for detecting volatile organic compounds (VOCs)[30]. Therefore, this research aims to provide valuable insights into how the physicochemical properties of hBN flakes influence their screening capabilities for industrial VOCs, with a specific focus on acetone and ethanol. The selection of these specific VOCs was based on three key factors: their easy availability in laboratories, low toxicity for safe handling, and, most importantly, their extensive utilization across various industries including defense, food, industrial and agricultural production, as well as medical and health diagnosis. Detecting and controlling these VOCs is crucial due to the potential health risks associated with long-term exposure. Moreover, it is essential to monitor ethanol concentrations in industrial production and road transportation practices as ethanol vapor and air have the potential to form an explosive mixture[67].

In this chapter, the fabrication, characterization, and evaluation of four different sensors based on hBN nanosheets for detecting ethanol and acetone vapors will be discussed. Additionally, a possible reaction mechanism on the hBN surface will be explored.

3.2 EXPERIMENTAL

For this study, pristine hBN and hBN flakes were employed, with the hBN flakes produced by incorporating barium fluoride (BaF$_2$) at different weight percentages: 2.5 %, 5 %, and 10 %. The sensing materials were synthesized and characterized at the *Laboratoire des Multimatériaux et Interfaces, Université Claude Bernard Lyon 1 (France)*, based on a procedure described elsewhere[133]. Subsequently, a summary will be provided regarding the synthesis and properties of the nanostructures.

The synthesis process involved the polymerization of pure borazine monomer at 55 °C, resulting in the formation of a colorless liquid polyborazylene (PBN). Subsequently, a mixture containing 5 wt.% lithium nitride (Li$_3$N) and varying amounts (ranging from 0 - 10 wt.%) of barium fluoride (BaF$_2$) was added to the PBN, followed by homogenization for 10 minutes. The resulting suspension was then heated to 200 °C for 1 hour, and the solid-state polymer was subsequently annealed at 1200 °C for 1 hour under an inert nitrogen (N$_2$, 98%, Air Liquide, France) atmosphere. The samples were labeled accordingly: pristine or 0 wt% hBN, 2.5 wt% hBN, 5 wt% hBN, and 10 wt% hBN, indicating the modification with 2.5, 5, and 10 wt% BaF$_2$[29].

The properties of these BaF$_2$-Modified hBN Flakes are shown in the Figure 18 and Table 4.
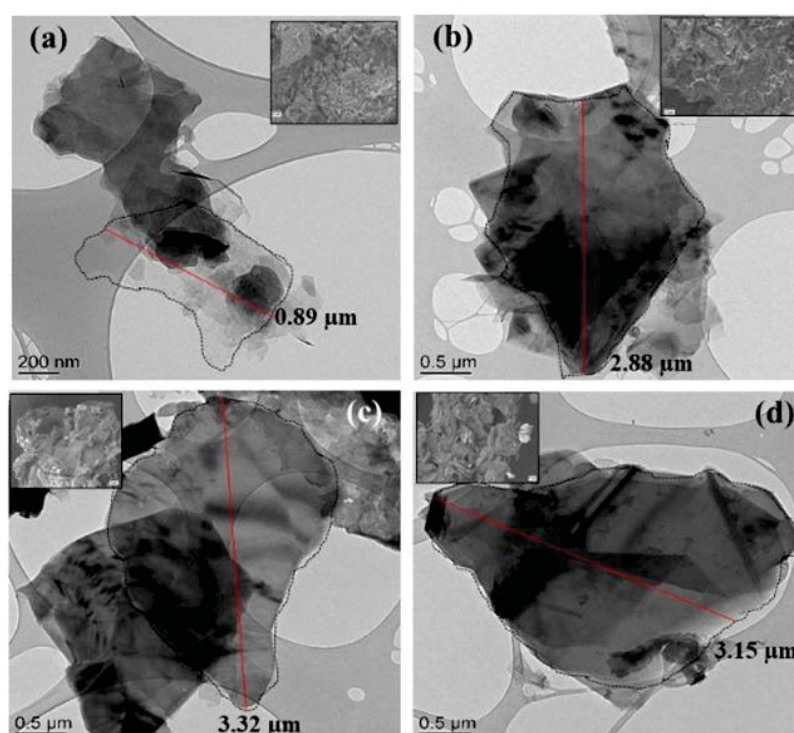
Figure 18 – Low magnification TEM images of hBN samples, (a) 0, (b) 2.5, (c) 5, and (d) 10 wt% BaF$_2$. Inset: SEM micrographs of the as-synthesized samples (1 μm scale bar)[133].

TABLE 4 – Physical and chemical properties of the hBN- BaF$_2$[29].

	Pristine hBN	2.5 wt% hBN	5 wt% hBN	10 wt% hBN
Crystal sizes (µm)	0.89 ± 0.01	2.9 ± 0.7	3.3 ± 0.3	3.2 ± 0.7
Boron/Nitrogen ratio	1.62	1.64	1.57	1.50
Surface areas (m^2 g^{-1})	8.7	3.5	3.6	2.9

The sensors were fabricated using a resin board (FR4) substrate with interdigitated ENIG electrodes (ENIG - Electroless Nickel Immersion Gold, supplied by Micropress S.A.), forming an active area of approximately 64 mm². Each device consists of 18 pairs of electrode strips with a width of 0.1 mm and a gap of 0.1 mm (Figure 19)[134]. According to thermogravimetric analysis, the FR4 does not have considerable mass loss as a consequence of degradation or decomposition, in the range of temperatures between 20 °C and 140 °C. Additionally, the FR4 has low water absorption (<0.1%), it is an insulator (dielectric constant of 4.70) with good mechanical resistance (Young modulus of 24 GPa)[135].
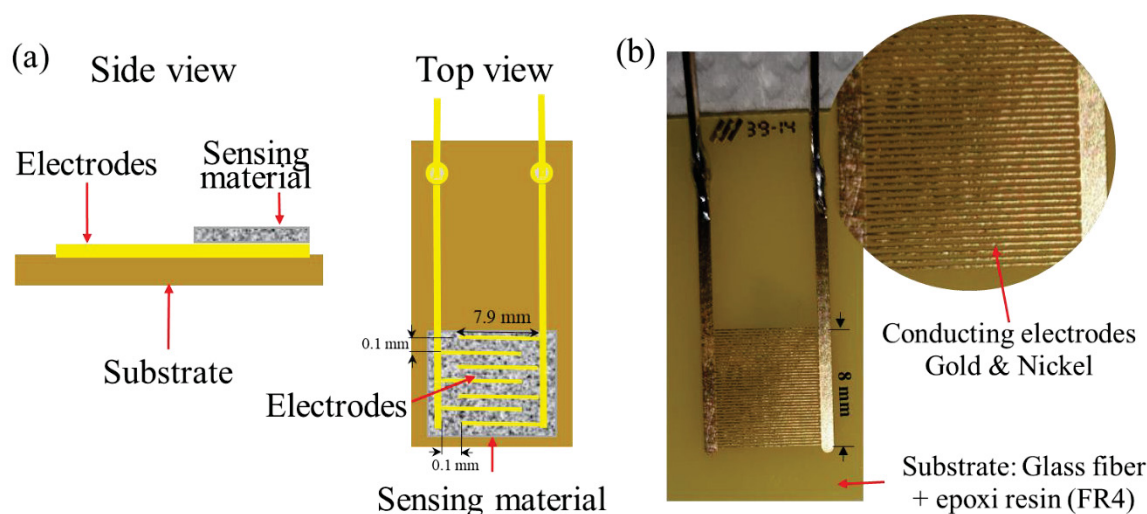
Figure 19 – (a) Representation of the sensors. (b) Photographic images of interdigitated electrodes and its magnification of the active area.

Interdigitated electrodes were sequentially cleaned in acetone, ultra-pure deionized water (resistivity > 18.2 MΩ/cm) and isopropyl alcohol by ultrasonication bath for 20 min in each step. The substrates were dried in an oven at 100 °C for 30 min (Figure 20).
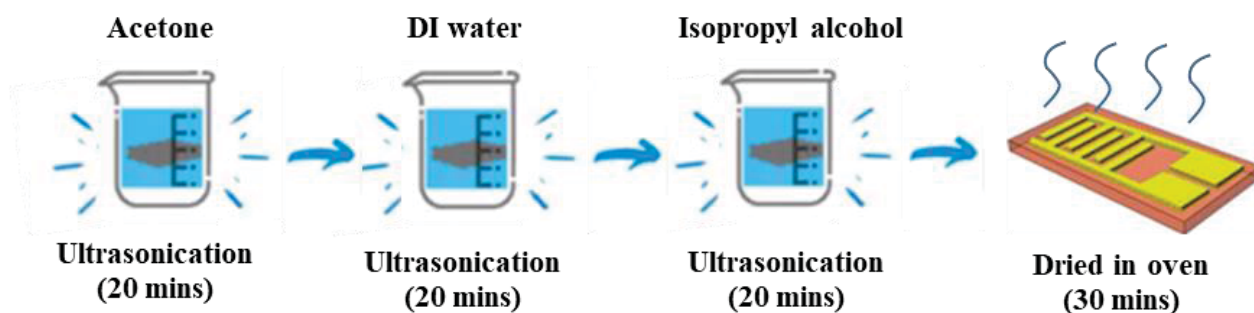
Figure 20 – The scheme of substrate cleaning.

For devices fabrication, dispersions of hBN samples at a concentration of 2 mg/mL in a solution containing 4 mg/mL of hexadecyltrimethylammonium bromide (CTAB) were sonicated for 30 minutes at 60 °C, followed by an additional 30 minutes at 0 °C[29]. The dispersions were then stored at 0 °C for 2 days to facilitate the precipitation of hydrated crystals[136]. Following the careful separation of the decanted portion, the supernatant dispersion (~500 µL), was obtained (Figure 21a). Subsequently, a precise 100 µL volume was extracted from this supernatant dispersion and drop-casted onto the active area of the interdigitated electrode (Figure 21b).
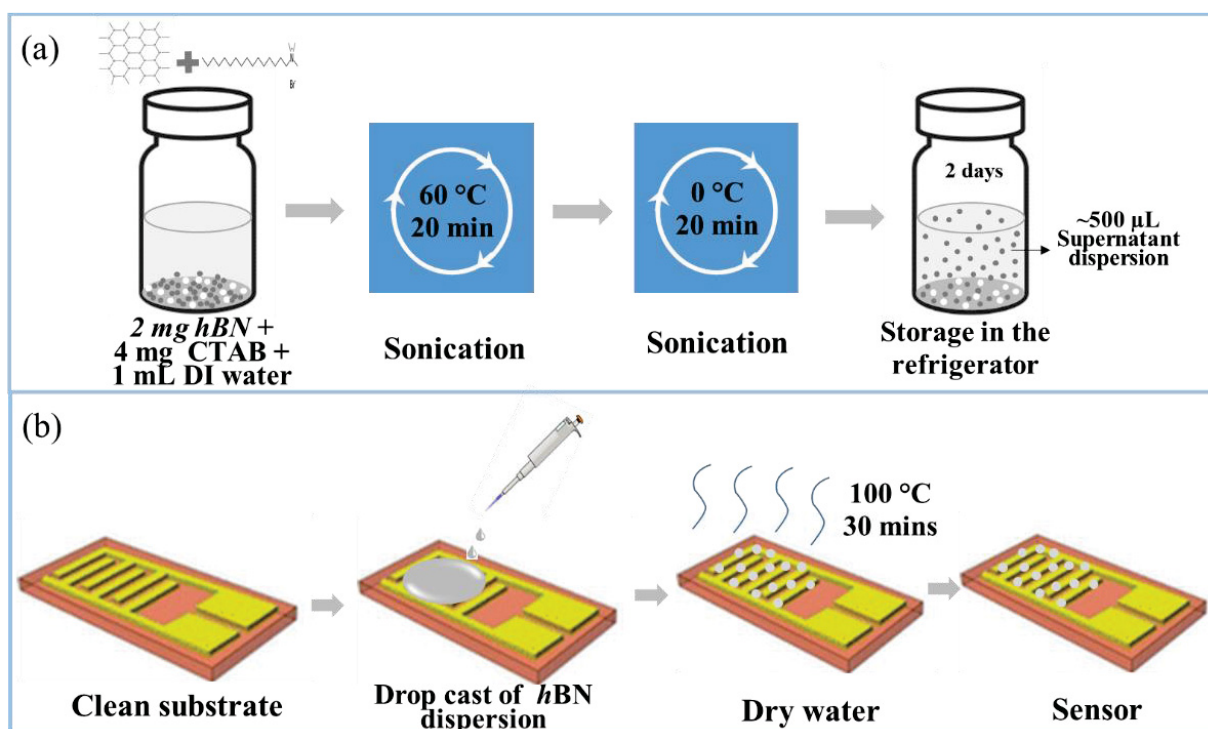
Figure 21 – Scheme of a dispersion with nanostructures (a) and the sensor fabrication (b).

From an experimental perspective, the drop-casting method used in sensor fabrication has been observed to result in heterogeneous modifications of the electrodes, as reported by

several authors[137,138]. Despite efforts to minimize this effect, such as temperature-staggered drying, some surfaces remain non-reproducible. Mutuma et al.[139] noted that differences in the shape and behavior of baseline (zero concentration) sensor resistance curves across frequencies can be attributed to electrode dispersion and sensor film thickness. This observation aligns with the methodology employed in our study, where different sensors were utilized for each measurement.

Concerning sensors measurements, analytes were dropped into a sealed chamber (Figure 22), which was properly grounded and kept in darkness. After a period of 1 hour, allowing the analysis chamber to reach steady-state conditions as determined in a previous study,[29] measurements were taken. The sensor response was obtained through impedance measurements using an Agilent 4284A LCR[1], with an AC signal amplitude of 0.5 V under a dry nitrogen atmosphere[140], where only the real part of it was analyzed and it is referred to resistance. The measuring equipment was calibrated in accordance with the standard procedure outlined in the LCR meter operation manual before initiating the resistance measurements.
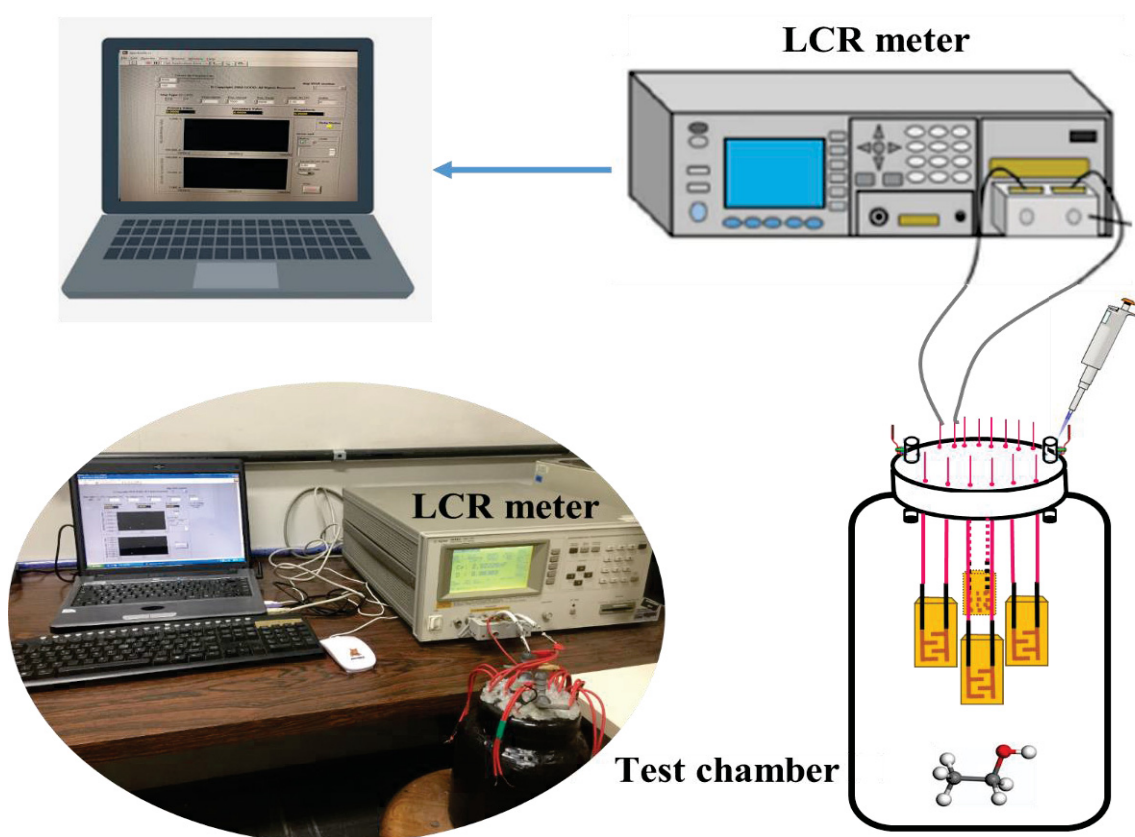
Figure 22 – Illustration of the experimental setup utilized for the electrical characterization of gas sensors.

[1]Electronic test equipment used to measure the inductance (*L*), capacitance (*C*), and resistance (*R*) of an electronic component.

The concentrations of acetone and ethanol vapors (C) were determined by quantifying the quantities of these substances introduced into the analysis chamber, as described by equation 3.1[6,134].

$$C_{ppm} = \frac{2.46 v \cdot d}{V_s \cdot M_W} x 10^7$$

(3.1)

Where v represents the volume (in µL) added to the chamber (in our case 1 µL, 2 µL, 3 µL and 4 µL, which correspond to the vapor concentrations shown in Table 5). V_s is the volume (in mL) of the analysis chamber (here: 2000 mL), d is the density of analyte (in gmL^{-1}) and M_W is the molecular weight of analyte in gM^{-1}

TABLE 5 – Vapor concentration of the analytes calculated using equation 3.1.

Analyte	Concentration (ppm)				
	1 µL	2 µL	3 µL	4 µL	5 µL
Acetone	163	326	489	652	815
Ethanol	211	422	633	844	1055

The response and recovery times were evaluated following the same methodology as represented in Figure 22. However, a rotating cap (as shown in Figure 23) was employed to alternate the sensor's exposure between the inside of the chamber (exposed to the analyte) and the outside, where the sensor was subjected to dry N_2 within a glove box environment (RH < 20%). This technique has been detailed in a separate publication[141].
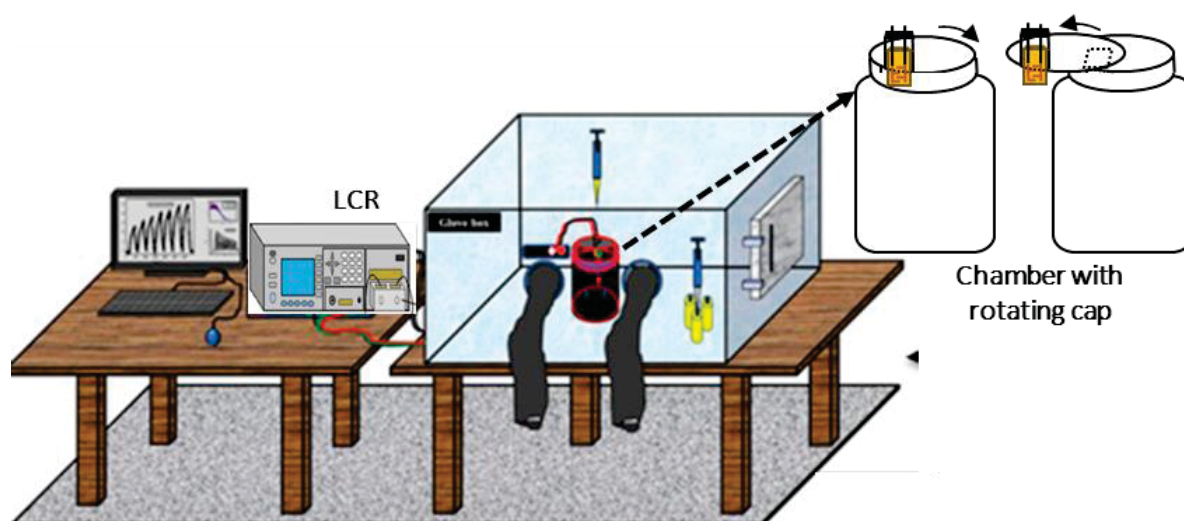
Figure 23 – Diagram showing the sensor inside and outside of the chamber during the transient measurements[30].

3.3 RESULTS AND DISCUSSION

3.3.1 Resistance measurements of the sensors

The electrical resistance of the active materials was plotted against frequency to analyze the response of the sensors as the concentration of individual or mixed analytes increased. Figure 24 demonstrated a significant reliance of the sensor response on the structural properties of the *hBN* nanosheets when exposed to escalating concentrations of acetone and/or ethanol vapors. This was evident in the notable decrease in resistance with increasing frequency across all samples, attributable to the presence of defects within the layered 2D structure of the *h*BN nanosheets[142]. Consequently, whether the nanosheets exhibit few defects as in the case of the 5 wt% BaF$_2$-modified *h*BN sample, or display a higher degree of defects as in the case of pristine and 2.5 wt% BaF$_2$-modified *h*BN samples, the presence of these defects influenced the resistance of the sensors. To mitigate these defects and overcome potential barriers within the layered 2D nanostructure, we applied an alternating electric field, enabling the movement of charge carriers over relatively long distances[143].
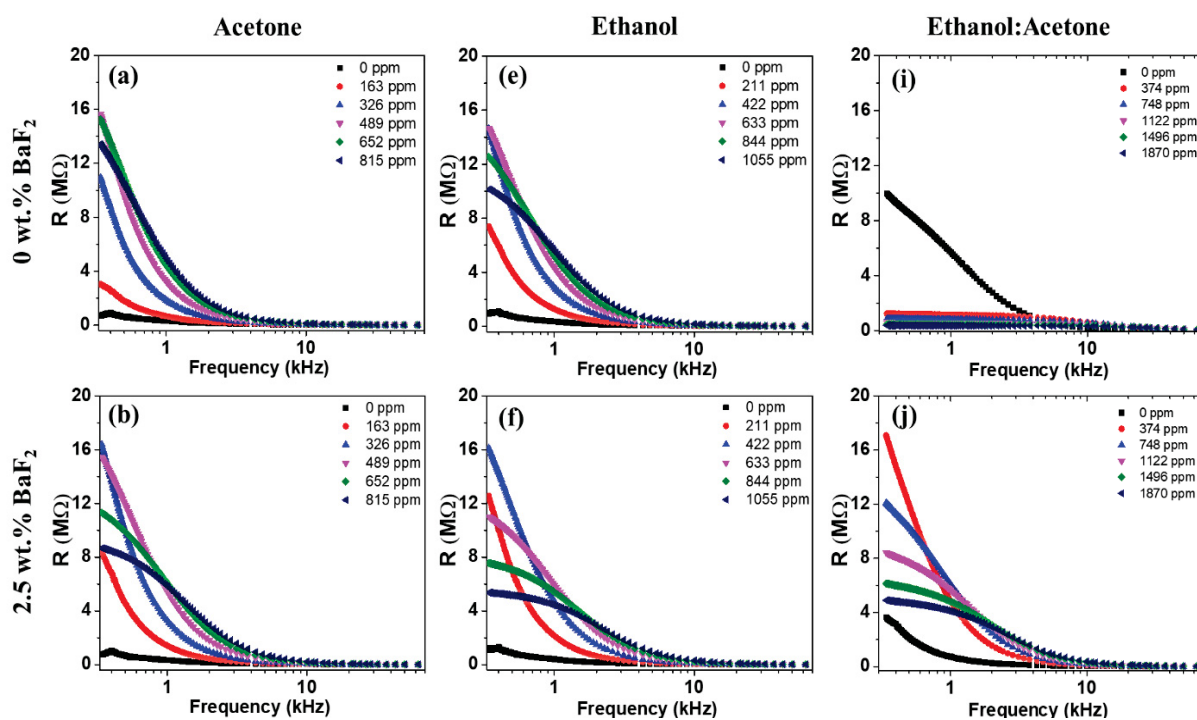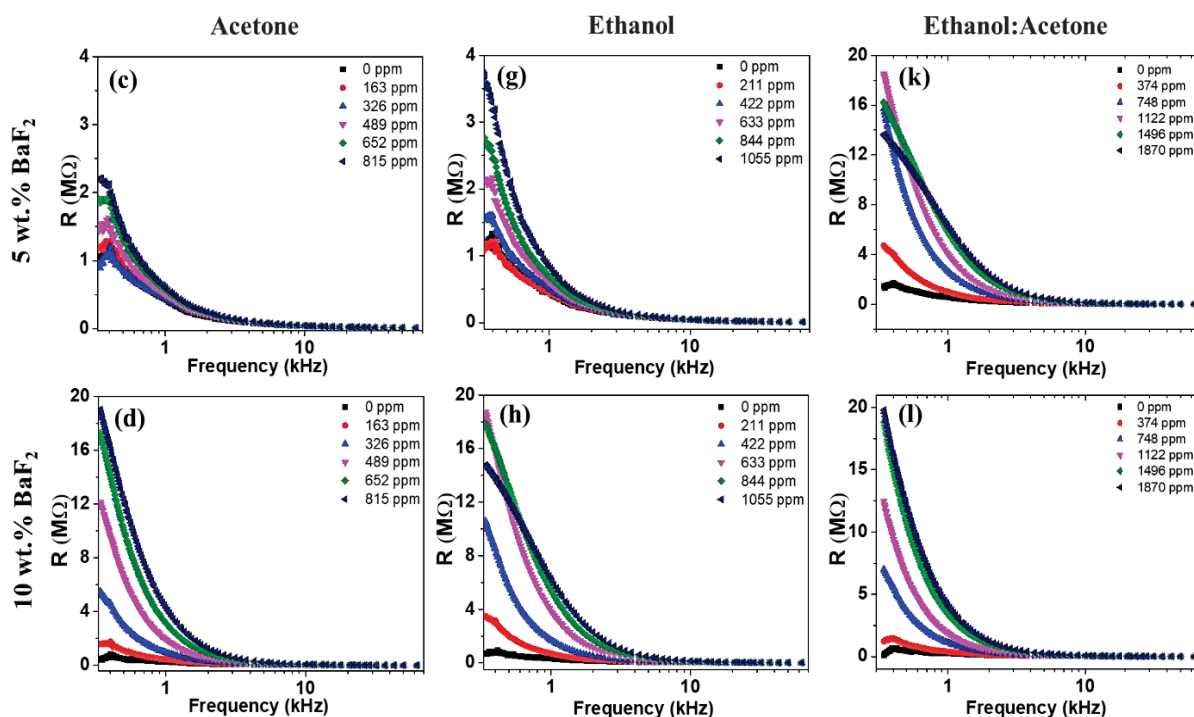
Figure 24 – Dependence of sensor resistance on frequency with increasing concentrations of (a–d) acetone, (e–h) ethanol and (i–l) EtOH:Acetone vapors.

3.3.2 Selection of the Optimal Operating Frequency

The selection of the optimum operating frequency for the sensors aimed to achieve a lower limit of detection (LoD) and higher sensitivity (S) (Figure 25 and Fig. A1 of the Appendix 1). Consequently, the best operating frequencies for the modified hBN-based devices in detecting acetone and/or ethanol were determined to fall within the range of 1-3 kHz. These frequencies proved to be superior to or comparable with those commonly employed by active materials for acetone and/or ethanol vapor detection, particularly for room temperature-based sensors. For instance, Mutuma et al.[139] reported operating frequencies of 3-10 kHz for acetone sensors based on nitrogen-doped hollow carbon spheres. In general, the results highlighted the substantial influence of the hBN sensor material's morphology on its sensing capability towards acetone or ethanol vapors.
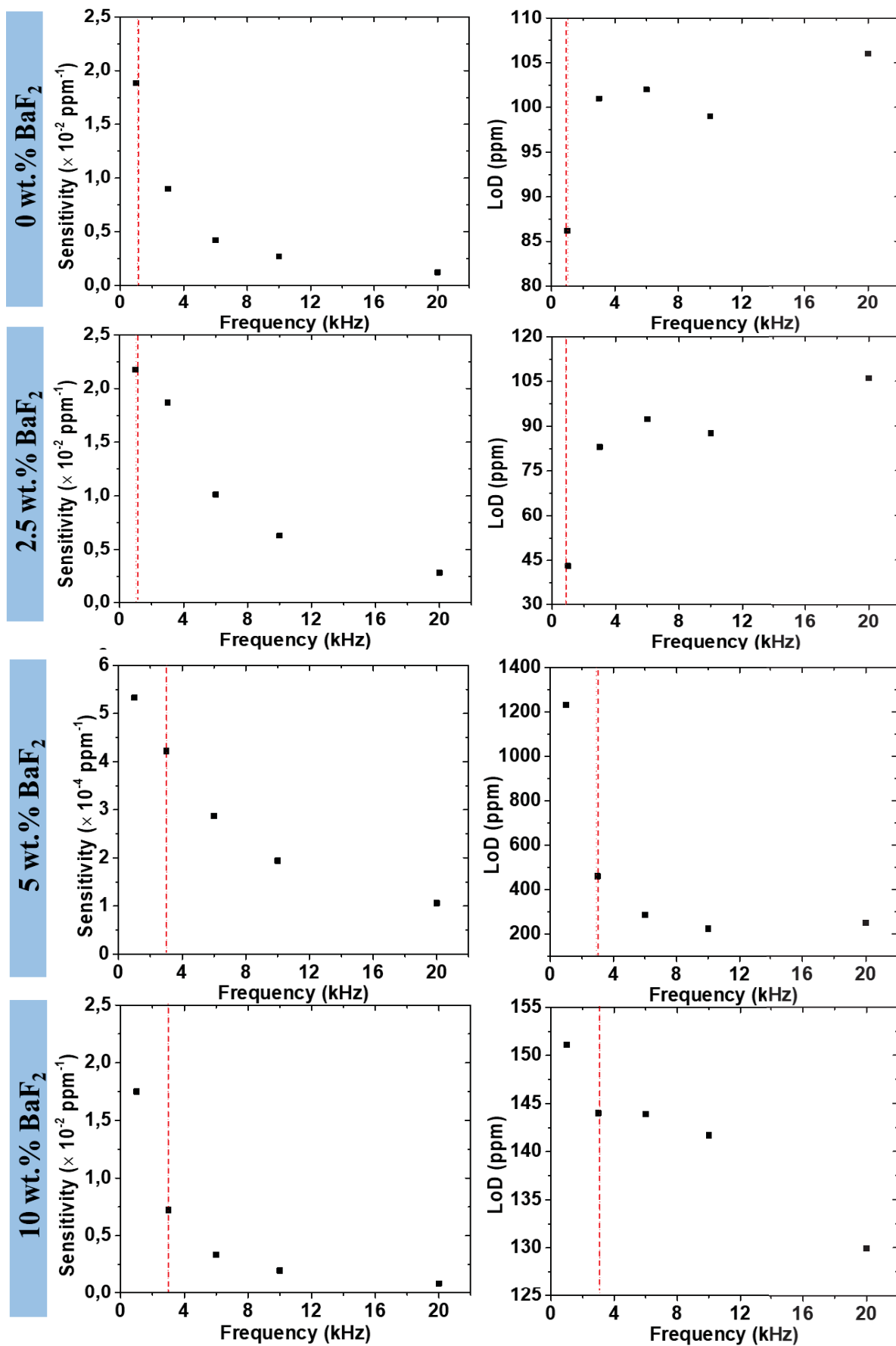
Figure 25 – The sensitivities and LoD of sensors data based on *h*BN-BaF$_2$ 0 wt%, 2.5 wt%, 5 wt% and 10 wt% for acetone, as a function frequency; dashed line indicates the optimum operating frequency.

3.3.3 Sensitivities (*S*) and limit of detection (LoD) of the sensors

The sensing parameters of each *h*BN-based device, including the limit of detection (LoD, equation 2.8) and the sensitivity (*S*), were estimated at the chosen optimum operating frequencies. These estimations were obtained from the plots of sensor resistance and/or response (equation 2.7) against the concentration of the target analytes. In Figure 26, it can be observed that the sensor responses increased with increasing concentrations of acetone or ethanol vapors, indicating that the *h*BN-based nanosheets used in this study exhibited p-type semiconducting behavior. However, the structural morphology of the *h*BN nanosheets significantly influenced the overall sensing performance of the devices. Devices based on *h*BN nanosheets with improved structural properties showed very low sensitivity and extremely high LoD values. For example, the sensor based on 5 wt% BaF$_2$-modified *h*BN nanosheets exhibited a sensitivity of 4.2 x 10^{-4} ppm^{-1} and a LoD of 460 ppm for acetone detection (Table 6). For ethanol detection, the same device registered a sensitivity of 4.5 x 10^{-4} ppm^{-1} and a LoD of 543 ppm. The inadequate sensing performance of the 5 wt% BaF$_2$-modified *h*BN-based devices, despite their relatively fast response and recovery times to acetone and ethanol (Figure 27c,g), could be attributed to the weak interactions between the carbonyl groups of the analyte molecules and the *h*BN basal surface[30].

A similar argument can be applied to explain the LoD of 144 ppm for acetone and 134 ppm for ethanol, as well as sensitivities of 7.2×10^{-3} ppm^{-1} for acetone and 1.9×10^{-3} ppm^{-1} for ethanol, in the case of the 10 wt% BaF$_2$-modified *h*BN-based devices when exposed to increasing concentrations of these vapors. Interestingly, a slight improvement in sensing performance was noticed for the *h*BN nanosheets with improved structural properties when exposed to a mixture of ethanol and acetone (Table 6 and Figure 26s,t). The 5 wt% and 10 wt% BaF$_2$-modified *h*BN-based devices demonstrated higher sensitivities of 7.0×10^{-3} ppm^{-1} and 1.0×10^{-2} ppm^{-1} and low limits of detection (LoD) values of 197 ppm and 439 ppm, respectively, indicating improved charge carrier transfer. Interestingly, the presence of defects had minimal impact on the sensing performance of the 0 wt% and 2.5 wt% BaF$_2$-modified *h*BN-based devices when detecting a mixture of ethanol and acetone vapors. These devices exhibited high sensitivity and low LoD values, suggesting that the defects acted as capture sites for the adsorption of a larger volume of analyte molecules. As a result, the 0 wt% and 2.5 wt% BaF$_2$-modified *h*BN-based devices achieved low LoD values of 30.4 ppm and 18 ppm, respectively.
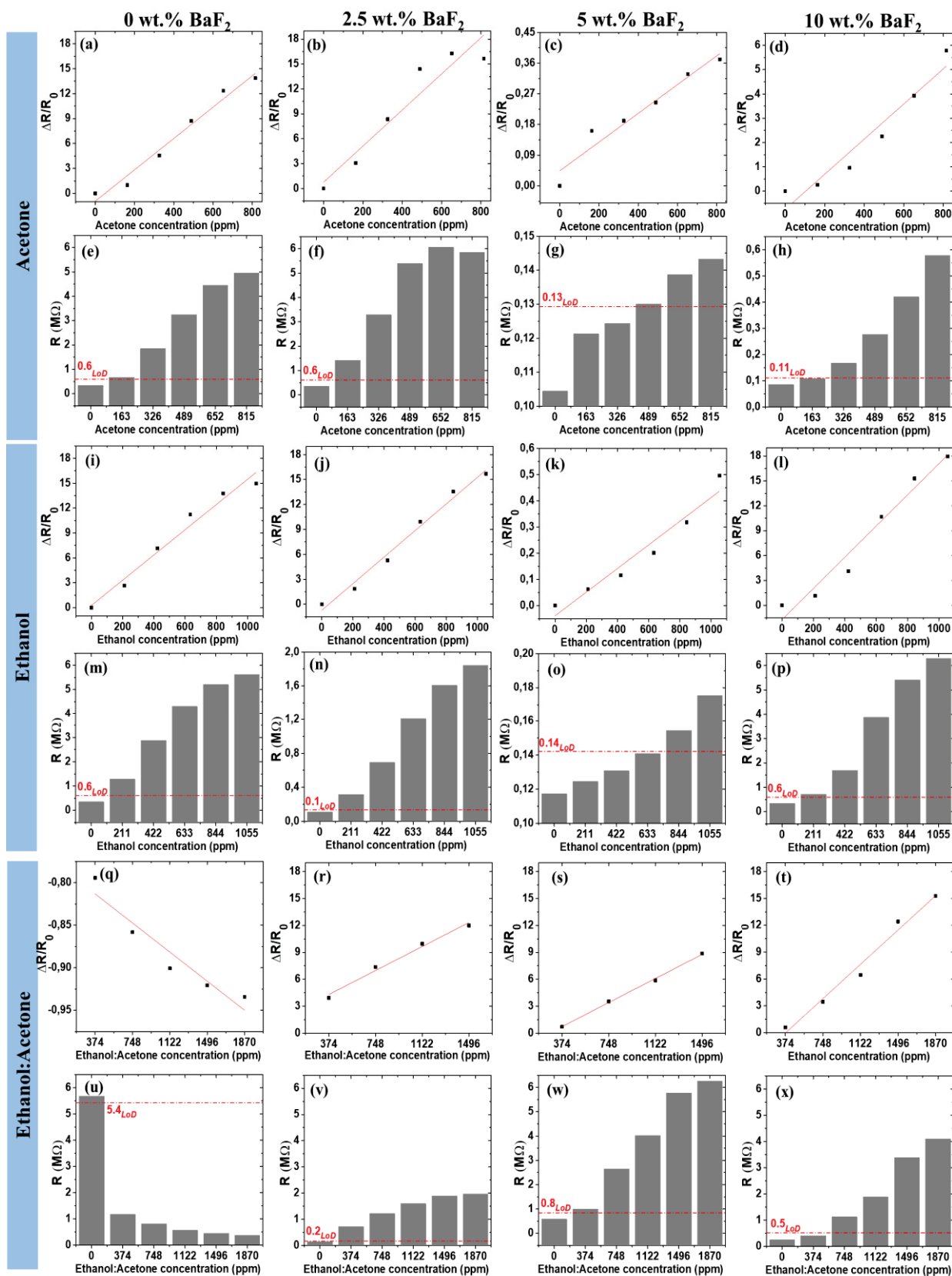
Figure 26 – Data set for sensors based on *h*BN-BaF$_2$ 0 wt%, 2.5 wt%, 5 wt% and 10 wt %, when exposed to acetone, ethanol and EtOH:Acetone at optimum operating frequencies, are presented in the first, second, third and fourth columns, respectively. (a–d, i–l and q–t) response of the sensor versus analyte concentration and (e–h, m–p and w–x) resistance as a function of analyte concentration; the dotted red line indicates the estimated LoD resistance of the corresponding sensor.

The lower limits of detection and higher sensitivity observed in the pristine and defective 2.5 wt% BaF_2-modified hBN samples suggest an improved sensing performance. This can be attributed to the enhanced surface interaction between the analyte molecules and the hBN nanosheets. The presence of nitrogen and/or boron vacancies (V_N or V_B) in the defective hBN structure may have served as electron capture sites, leading to increased sensitivity upon exposure to acetone or ethanol[144,145].

TABLE 6. Optimum frequency (f), determined limit of detection concentration (LoD), and sensitivity (S) for detection of acetone, ethanol, and acetone: ethanol mixture.

Analyte	Parameter	0 wt%	2.5 wt%	5 wt%	10 wt%
Acetone	f (kHz)	1	1	3	3
	S ($\times 10^{-2}$ ppm^{-1})	1.8	2.1	0.042	0.72
	LoD (ppm)	86.2	43.2	460	144
Ethanol	f (kHz)	1	3	3	1
	S ($\times 10^{-2}$ ppm^{-1})	1.5	1.6	0.045	0.19
	LoD (ppm)	30.4	61.7	542.6	133.5
Acetone: Ethanol (1:1)	f (kHz)	1	3	1	1
	S ($\times 10^{-2}$ ppm^{-1})	-9.1	7.0	7.2	10.0
	LoD (ppm)	30.4	18	197	439

3.3.4 Dynamic response

The gas-sensing performance of hBN-based sensors was evaluated by examining their responses to individual acetone or ethanol vapors and their recovery upon vapor removal. Figure 27 demonstrates that all active materials exhibited excellent gas-sensing performance, with response and recovery times of less than 100 s (Table 7) when exposed to 160 ppm analyte vapor at the optimal frequencies. However, when exposed to a vapor mixture, compromised response times were observed for all samples, except for the sensors based on 5 wt% BaF_2-modified hBN samples (t_{res} 56 s and t_{rec} 15 s). This discrepancy can be attributed to the limited interaction between acetone and ethanol molecules with the basal planes of hBN flakes. Additionally, most of the samples exhibited behavior consistent with p-type semiconducting devices. This was indicated by an increase in sensor resistance upon exposure to the analyte vapor and a decrease in resistance upon removal. In contrast, the devices fabricated from 0 wt% BaF_2-modified hBN samples showed n-type semiconducting behavior (Figure 27i). This behavior suggests a prolonged depletion of pre-generated holes and an increased number of

hopping sites due to the defective nature of the 0 wt% BaF$_2$-modified hBN sample, leading to increased conductivity when exposed to the vapor mixture.

The 5 wt% and 10 wt% BaF$_2$-modified hBN samples demonstrated response times of less than 60 s when exposed to acetone vapor, and recovery times of less than 50 s after acetone removal (Figure 27c,d and Table 7). These impressive results can be attributed to the abundance of active surface adsorption sites on the basal planes of the hBN nanosheets. These sites facilitate the generation of ionized adsorbed oxygen species, such as O$_2^-$, O$^-$, or O^{2-} (Figure 28a,b)[146] which in turn accelerate the conversion of acetone to carbon dioxide (Figure 28c(i)). This is possible due to the weak interaction between acetone molecules and the hBN surface[30].

Moreover, the 5 wt% BaF$_2$-modified hBN sample displayed an enhanced saturation platform compared to other hBN-based devices (Figure 27c). This can be attributed to the larger basal planes present in this sample, which enable improved adsorption and coverage of acetone molecules over a larger surface area. Consequently, this sample exhibited faster response and recovery times. Importantly, when exposed to a mixture of acetone and ethanol, the 5 wt% BaF$_2$-modified hBN-based sensor device demonstrated rapid response (56 s) and recovery (15 s) times, indicating its selectivity towards acetone even in the presence of other volatile organic compounds (VOCs).

Table 7 – Response (t$_{res}$) and recovery (t$_{rec}$) time for sensors based on hBN-BaF$_2$ 0, 2.5, 5 and 10 wt%

Analyte	Samples	t$_{resp}$ (s)	t$_{recov}$ (s)
Acetone	0 wt%	74	95
	2.5 wt%	61	71
	5 wt%	36	44
	10 wt%	54	50
Ethanol	0 wt%	79	34
	2.5 wt%	77	40
	5 wt%	69	34
	10 wt%	71	56
Acetone: Ethanol (1:1)	0 wt%	78	15
	2.5 wt%	113	75
	5 wt%	56	15
	10 wt%	102	20
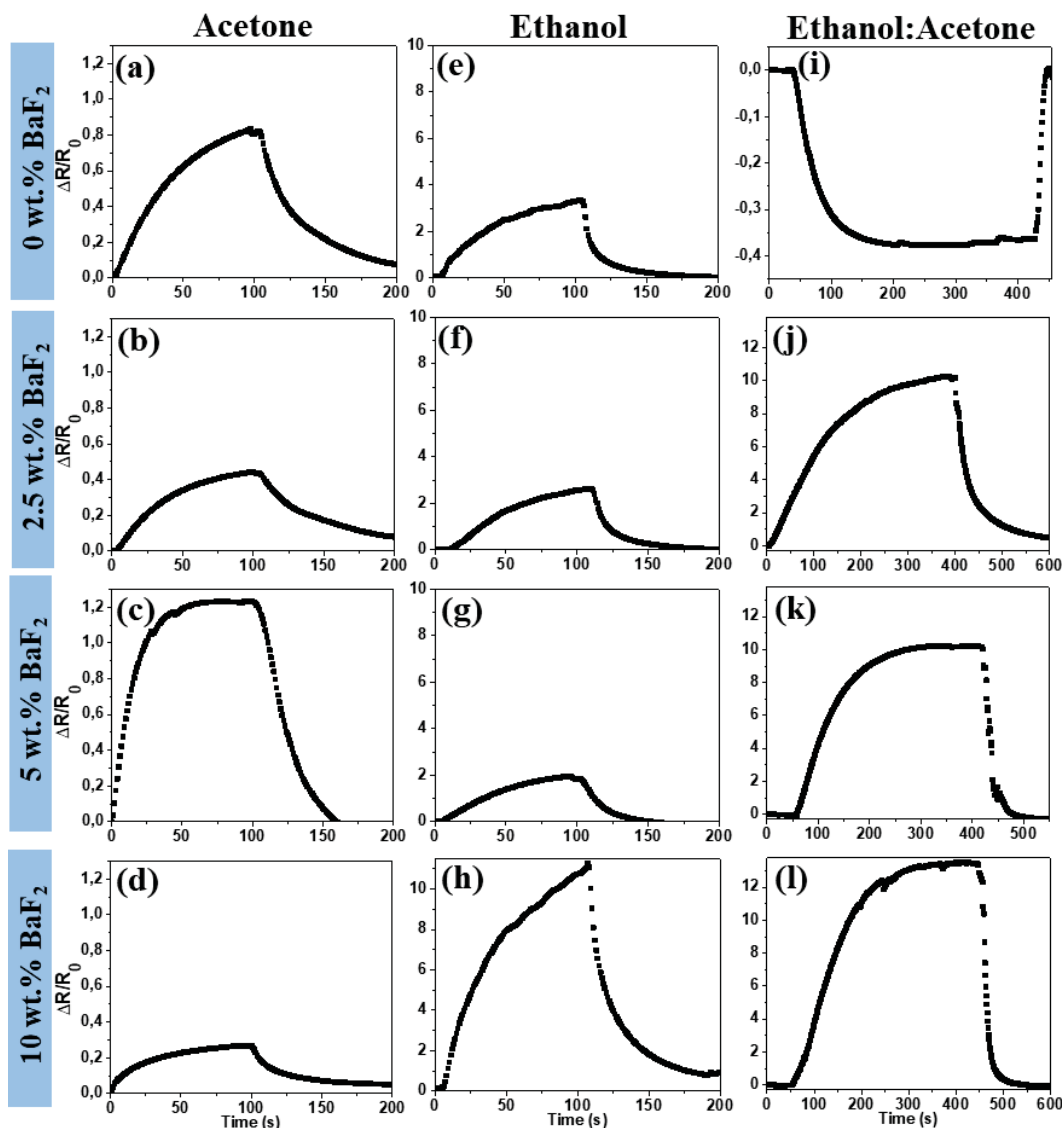
Figure 27 – Responses and recovery times for devices fabricated after exposure and removal of 160 ppm of (a–d) acetone, (e–f) ethanol, and (i–l) acetone: ethanol vapors at optimum operating frequencies.

On the contrary, the extended response times observed for the pristine hBN sample (74 s) and the 2.5 wt% BaF$_2$-modified hBN sample (61 s) in detecting acetone can be attributed to the presence of structural defects that retain the charge carriers. These defects cause prolonged electron-hopping effects, resulting in delayed sensor response. Moreover, it can be inferred that these defects promote a strong interaction between acetone molecules and the hBN surface, leading to longer recovery times of 95 s and 71 s for the pristine and 2.5 wt% BaF$_2$-modified hBN samples, respectively. The extended response and recovery times, approximately 113 s and 75 s respectively, for the 2.5 wt% BaF$_2$-modified hBN samples further indicate the retention of charge by the defects. Consequently, these defects negatively impact the sensing performance of the 2.5 wt% BaF$_2$-modified hBN samples to detect the mixture of acetone and ethanol.

As shown in Table 7, the sensors exhibited poor response times (70-80 s) when exposed to ethanol vapor, indicating inefficient transfer of charge carriers from the hBN active materials to the adsorbed ethanol molecules, resulting in a prolonged electron-hopping effect. While the sensing performance towards ethanol and/or acetone is primarily influenced by the interaction between ethanol molecules and adsorbed O_2^{-}, O^{-}, or O^{2-} species, the extended response times observed during ethanol exposure for all devices suggest the challenging absorption of the more polar ethanol molecules on the surface and grain boundaries of hBN nanosheets, in contrast to the adsorption mechanism of acetone. Furthermore, the two-step reduction process of ethanol on the active materials (Figure 28c(ii, iii)) could contribute to the longer response times observed for ethanol across all samples[53,147]. In this case, when the sensing device was exposed to ethanol vapor, the reduced gas molecules were first oxidised into an acetaldehyde molecule (Figure 28c(ii)), which then required more oxygen anions for the final conversion into carbon dioxide and water (Figure 28c(iii)). However, the relatively shorter recovery times of approximately 34 s, 56 s, 34 s, and 40 s for the pristine, 2.5 wt%, 5 wt.%, and 10 wt% BaF$_2$-modified hBN-based devices, respectively (Table 7), suggest a weak interaction between the ethanol molecule and the basal planar hBN surface[30].
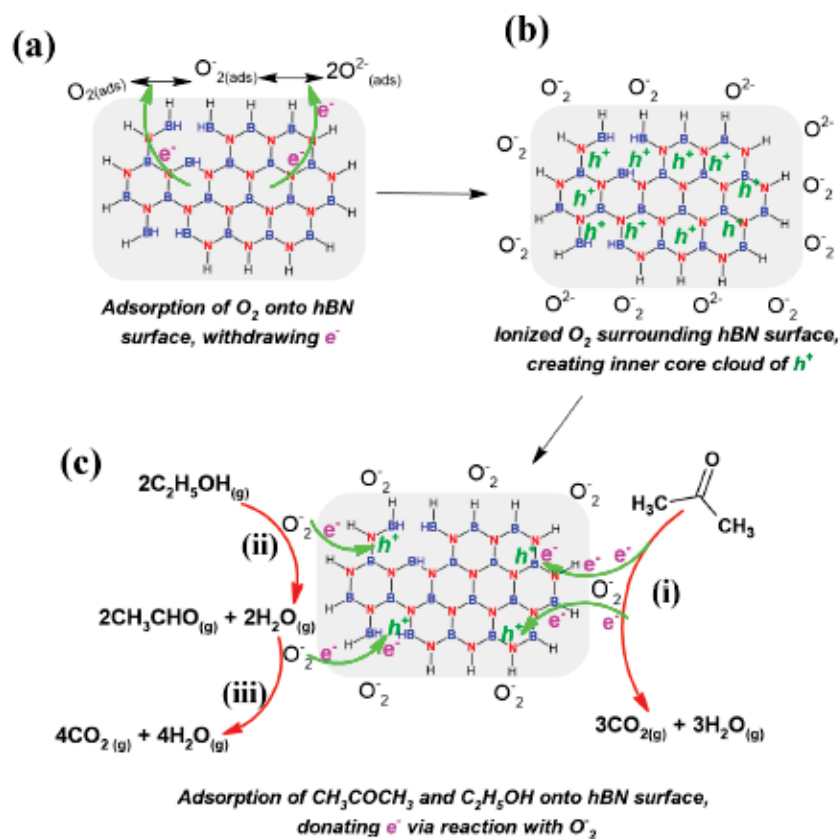
Figure 28 – Adsorption and reaction mechanism of acetone or ethanol on the hBNs surface.

These findings highlight the potential of layered hBN nanosheets with well-defined morphologies and improved properties as efficient resistance-based sensors for volatile organic compounds (VOCs), similar to other materials such as zero-bandgap graphene, small band-gap semiconducting transitional metal dichalcogenides (TMDs), and conducting mxenes[148–150].

3.3.5 Stability of the sensors

The hBN sensors demonstrate long-term stability, maintaining in some samples their sensitivity even after an extended period of storage. After 18 months, the sensitivity values for acetone were 0.04, 0.1, 0.04, and 0.12×10^{-2} ppm^{-1}, while for ethanol they were 0.4, 2.3, 0.06, and 0.2×10^{-2} ppm^{-1}, corresponding to the 0 wt%, 2.5 wt%, 5 wt%, and 10 wt% modified hBN samples, respectively (Table 8). When comparing the sensitivities of the initial samples (Table 6) with the same samples after the storage period, the 5 wt% BaF_2 modified hBN samples consistently exhibited reproducible results. This can be credited to the improved crystalline structure of the nanoflakes, which effectively mitigated or decelerated the degradation of the hBN.

TABLE 8 –Sensitivity Long-Term Evaluation of hBN Sensors after 18 Months of Testing and Storage

Analyte	Parameter	0 wt%	2.5 wt%	5 wt%	10 wt%
Acetone	f (kHz)	1	1	3	3
	S ($\times 10^{-2}$ ppm^{-1})	0,04	0,1	0,04	0,12
Ethanol	f (kHz)	1	3	3	1
	S ($\times 10^{-2}$ ppm^{-1})	0,4	2.3	0,06	0,2

Furthermore, when exposed to 160 ppm of acetone, the sensor responses exhibited approximately 75%, 50%, 92%, and 8% decreases for the 0 wt%, 2.5 wt%, 5 wt%, and 10 wt% modified hBN samples, respectively (Figure 29).
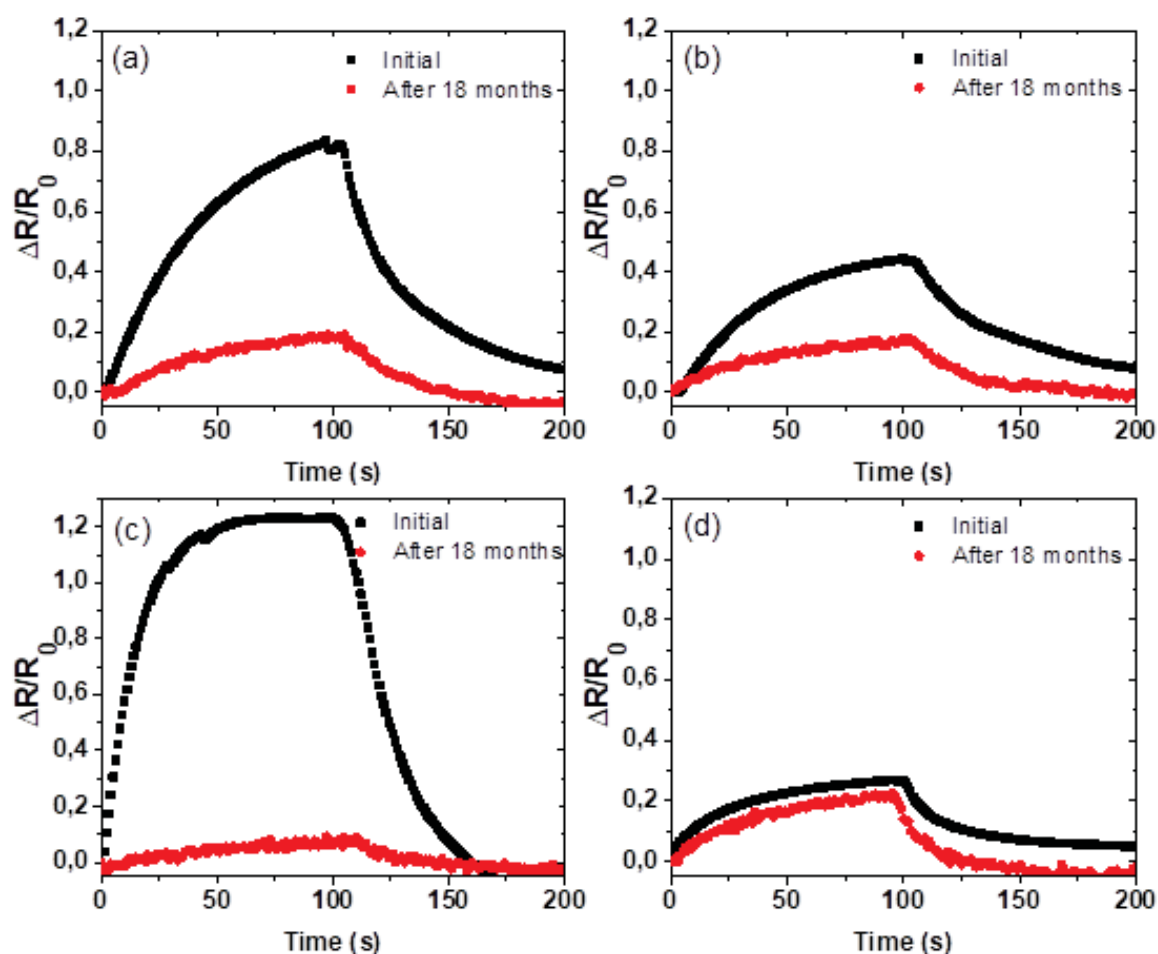
Figure 29 – Responses and recovery times for (a) 0 wt%, (b) 2.5 wt%, (c) 5 wt% and (d) 10 wt% BaF$_2$-modified *h*BN devices fabricated 18 months ago and initial measurements, during exposure and removal of 160 ppm of acetone at optimum operating frequencies.

3.3.6 Comparison of results

The results presented in Table 9 reveal comparable performance to other 2D materials such as graphene oxide, transition metal dichalcogenides (TMDs), and mxenes in terms of the limit of detection (LoD). Importantly, the defective *h*BN samples exhibited significantly lower LoD values for both acetone and ethanol compared to previous studies, exceeding the reported values.

TABLE 9. Comparative sensor data for the hBN samples with other related materials for VOCs sensors[30].

Analyte	Active Material	Sensor Type	Conc. Range (ppm)	Temp. (°C)	LoD (ppm)	Ref.
Acetone	pristine hBN	Chemoresistive	0 - 100	RT	86	This work
	2.5 wt% BaF$_2$-hBN				43	
	5 wt% BaF$_2$-hBN				460	
	10 wt% BaF$_2$-hBN				144	
	ZnO		5 - 1000	300	10	[151]
	ZnO/Gr		10 - 10000	280	13.3	[152]
	α-Fe$_2$O$_3$/rGO		5 - 500	225	5	[153]
	g-C$_3$N$_4$/WO$_3$		N/A	340	100	[149]
	Ti$_3$C$_2$T$_x$	Electrochemical	N/A	RT	0.05	[53]
Ethanol	pristine hBN	Chemoresistive	0 - 100	RT	30	This work
	2.5 wt% BaF$_2$-hBN				62	
	5 wt% BaF$_2$-hBN				543	
	10 wt% BaF$_2$-hBN				134	
	SnO$_2$/MoS$_2$		N/A	280	50	[154]
	ZnO/GO		0 - 1000	400	10	[155]
	Ti$_3$C$_2$T$_x$	Electrochemical	N/A	RT	0.10	[53]

3.4 SUMMARY

The study investigated hexagonal boron nitride (hBN) flakes modified with barium fluoride (BaF$_2$) for volatile organic compounds (VOCs) detection. Sensors utilizing hBN nanostructures showed activity for acetone and ethanol, with their performance influenced by structural properties. Pristine hBN and 2.5 wt% BaF$_2$-modified hBN sensors exhibited improved sensing capabilities, with low limits of detection (LoDs) and high sensitivities attributed to defective domains. However, 5-10 wt% BaF$_2$-modified hBN sensors with improved morphology hindered sensing performance due to high LoDs and poor sensitivities, possibly due to lower surface areas. The study highlights the importance of structural properties in hBN-based sensors' performance for VOC detection.

CHAPTER 4

4 SENSING PROPERTIES OF LIG/ZNO/MWCNTs AND LIG/ZNO/MWCNTs/PVP COMPOUND AS VOCs GAS SENSORS

4.1 INTRODUCTION

The field of flexible electronics has witnessed significant advancements, leading to the development of more ergonomic devices. Among the promising techniques for fabricating graphene electrodes on flexible substrates[156], laser-direct writing (LDW) has emerged as a notable approach[157]. LDW enables precise control and high-resolution patterning using a computer-controlled robotic system[158], without the need for direct contact between the system and the substrate. This technique offers advantages such as high resolution, rapid fabrication, and design flexibility, while eliminating the requirements for masks or complex clean-room environments, thereby making it a cost-effective method[157].

In 2014, the discovery of laser-induced graphene (LIG) revolutionized the synthesis of graphene, utilizing the innovative and sustainable LDW technique[159]. This process involves irradiating the surface of polyimide films with a CO_2 infrared laser beam. The photothermal reaction induced by the laser, breaks the C-O, C=O and N-C bonds, converting the sp^3 carbon atoms of the polyimide into sp^2 carbon atoms and forming graphitic structures[159,160]. This single-step process eliminates the need for reducing agents, expensive equipment, solvents, or additional treatments[161]. LIG exhibits turbostratic (disordered layering) structure with a spacing between layers approximately 0.1 nm larger compared to graphite[162]. Its foam-like structure contains numerous bent planes, leading to a broader D band in Raman spectroscopy[159]. LIG is typically less than 10 layers thick and lacks optical and electronic coupling between layers. In contrast, graphite is AB stacked and comprises many graphene layers, exceeding 10 layers in thickness[163]. Graphite demonstrates optical and electronic coupling between layers, with the layers being joined together by van der Waals attractions between adjacent layers[163,164]. The structures of monolayer graphene, multi-layer graphene, and graphite are depicted in Figure 30 While graphene is defined as a monolayer, the term has been used ambiguously to encompass other layered forms of the material, including multi-layer graphene[165].
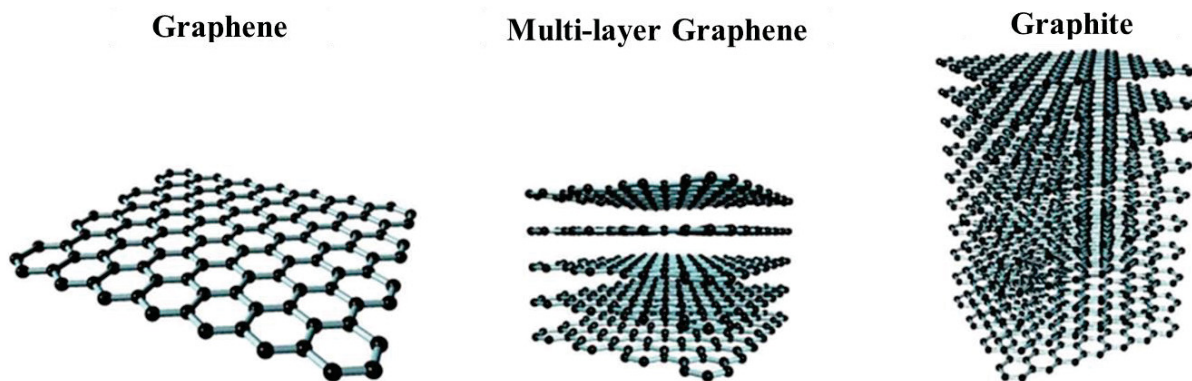
Figure 30 – Various forms within the graphene family[166–168].

Additionally, LIG demonstrates compatibility with a wide range of carbon precursors[169]. Its high electrical conductivity and mechanical robustness make it particularly suitable for sensor electrodes[156,170]. Moreover, LIG can be effectively integrated with other materials, including metals, metal oxides, additives, or heteroatoms, to form composite materials. This integration leads to synergistic effects, harnessing the strengths of both LIG and the additional materials. These benefits encompass improved thermal conductivity, enhanced electron mobility, increased mechanical stability, and an expanded surface area, which confer significant advantages in diverse applications, including gas sensing devices[171].

Zinc oxide (ZnO) is a noteworthy semiconductor metal oxide that is frequently utilized in conjunction with laser-induced graphene[169]. ZnO possesses several desirable properties, including piezoelectricity, high-energy radiation stability, non-toxicity, biocompatibility, and cost-effective growth techniques[169,172,173]. The combination of laser-induced graphene as a substrate with ZnO shows promise, as the porous structure of LIG allows for superior loading of ZnO structures[174]. Consequently, the integration of LIG and ZnO materials presents a novel avenue to enhance the gas response and improve the response time of gas sensors. Numerous studies have reported the use of graphene/ZnO-based nanocomposites for detecting various toxic gases, including hydrogen, hydrogen sulfide, acetylene, formaldehyde, nitrogen dioxide, and ammonia[108,175–183]. However, there is a limited availability of research specifically focused on incorporating LIG with ZnO for the detection of VOCs.

In a study conducted by Zhao et al.[184] (2023), they reported the in situ laser-assisted synthesis and patterning of MoS_2, CuO, and Ag/ZnO on laser-induced graphene (LIG). This resulted in the development of a flexible and stretchable gas sensing platform capable of detecting NO_2, H_2S, and trimethylamine (TMA). The researchers achieved low limits of detection (LOD) ranging from 2.7 to 9.8 ppb. Additionally, the gas sensing platform demonstrated excellent sensitivity, selectivity, rapid response and recovery times, and the

capability to adjust the operating temperature. Additionally, the analysis of a gas sensor array enabled the identification of multiple gas species present in the environment or exhaled breath.

Hussein et al.[185] conducted a study where they fabricated gas sensors by modifying a porous silicon (PS) layer with a thin layer of carbon nanotubes (CNTs) and carbon nanotubes doped with zinc oxide (ZnO) nanoparticles in a ratio of 70-30 %, respectively. The aim was to detect ethanol at room temperature. The findings showed that the CNTs-ZnO/PS sensor exhibited the highest sensitivity to ethanol gas, reaching approximately 2.005 at a concentration of 500 ppm.

This chapter focuses on the preparation of a composite material composed of LIG/ZnO/MWCNTs and LIG/ZnO/MWCNTs/PVP for the detection of volatile organic compounds (VOCs). The fabrication and electrical characterization of the sensors were conducted at the *Sensors and Measurements (MST) research group, located at Chemnitz University of Technology in Germany*. The sensing films underwent comprehensive characterization employing various techniques, such as morphological, structural, and chemical analysis. The properties of the composite material are thoroughly examined and discussed, providing valuable insights into their impact on VOC sensing.

4.2 EXPERIMENTAL

Zinc Oxide (ZnO) <50 nm (Aldrich), Multi-Walled Carbon Nanotubes (MWCNTs, OD: 40-60 nm, L: 5 -15 µm, IOLITEC), Surfactant hexadecyltrimethylammonium bromide (CTAB, 98% w/w, Sigma-Aldrich) and polyvinylpyrrolidone (PVP, wt 40,000, Sigma-Aldrich), were used as received. The interdigitated electrodes were fabricated using commercial Kapton® polyimide (abbreviated PI) film.

The ZnO nanoparticles dispersion was obtained by stirring, for 30 minutes, 26 mg of ZnO nanoparticles in 10 mL of deionized water, reaching a concentration of 1.6×10^{-2} w/w. On the other hand, MWCNTs dispersions were prepared using a surfactant dispersion method[30,139]. For this 2 mg of MWCNTs and 4 mg of CTAB were mixed in 1 mL of deionized water, and then the mixture was sonicated in bath for 30 minutes at 60 °C, followed by another 30 minutes at 0 °C. Subsequently, MWCNTs/CTAB dispersions were kept at 0 °C for 2 days. The supernatant of the final dispersion was extracted and used in the subsequent steps. On the other hand, to prepare the MWCNTs/PVP compound, a solution of PVP was made by dissolving 25 mg of PVP in 0.2 mL of deionized water. The resulting mixture was stirred for

30 minutes at a temperature of 50 °C. Finally, the MWCNTs/PVP composite dispersion was prepared by combining 250 μL of the previously prepared MWCNTs supernatant dispersion with 50 μL of the PVP solution. The mixture was then subjected to sonication for 30 minutes at room temperature[134].

A schematic illustrating the fabrication process of the sensors is shown in Figure 31. The process involved three steps: **(a)** the generation of LIG interdigitated electrodes using a commercial Kapton thin film, which was first cleaned with isopropyl alcohol. The Epilog laser UML 340 machine (405 nm, raster setting, speed: 20%, Power: 15%) was utilized for laser engraving. The laser traced an interdigitated pattern of electrodes onto the surface, causing the Kapton in that area to change to a black color and become conductive. **(b**) A 40 μL ZnO dispersion was drop-cast onto the interdigitated area and then dried in an oven at 100 °C for 20 minutes. **(c)** Similarly, a 40 mL supernatant dispersion was drop-cast onto the active area of LIG/ZnO separately for each device, based on MWCNTs or MWCNTs/PVP. Subsequently, they were dried in an oven and utilized in our study for sensor applications.

For sensor measurements, the analytes were dropped into a securely sealed glass chamber (7 L), which was properly grounded and kept unilluminated, with the sensors placed inside. The analytes were added to the test chamber at various volumes to achieve concentrations of 100, 200, and 300 ppm (calculated according to equation 3.1). Following a 30-minute period, measurements were taken to ensure the analysis chamber reached a stable and steady-state condition. The sensor response was obtained by conducting resistance measurements using an Agilent 4294A Precision Impedance Analyzer, operating within a dry nitrogen atmosphere. This measurement setup closely resembled the one depicted in Figure 24. Multiple devices were simultaneously measured by utilizing a test chamber that facilitated the switching of electrical connections from wire.
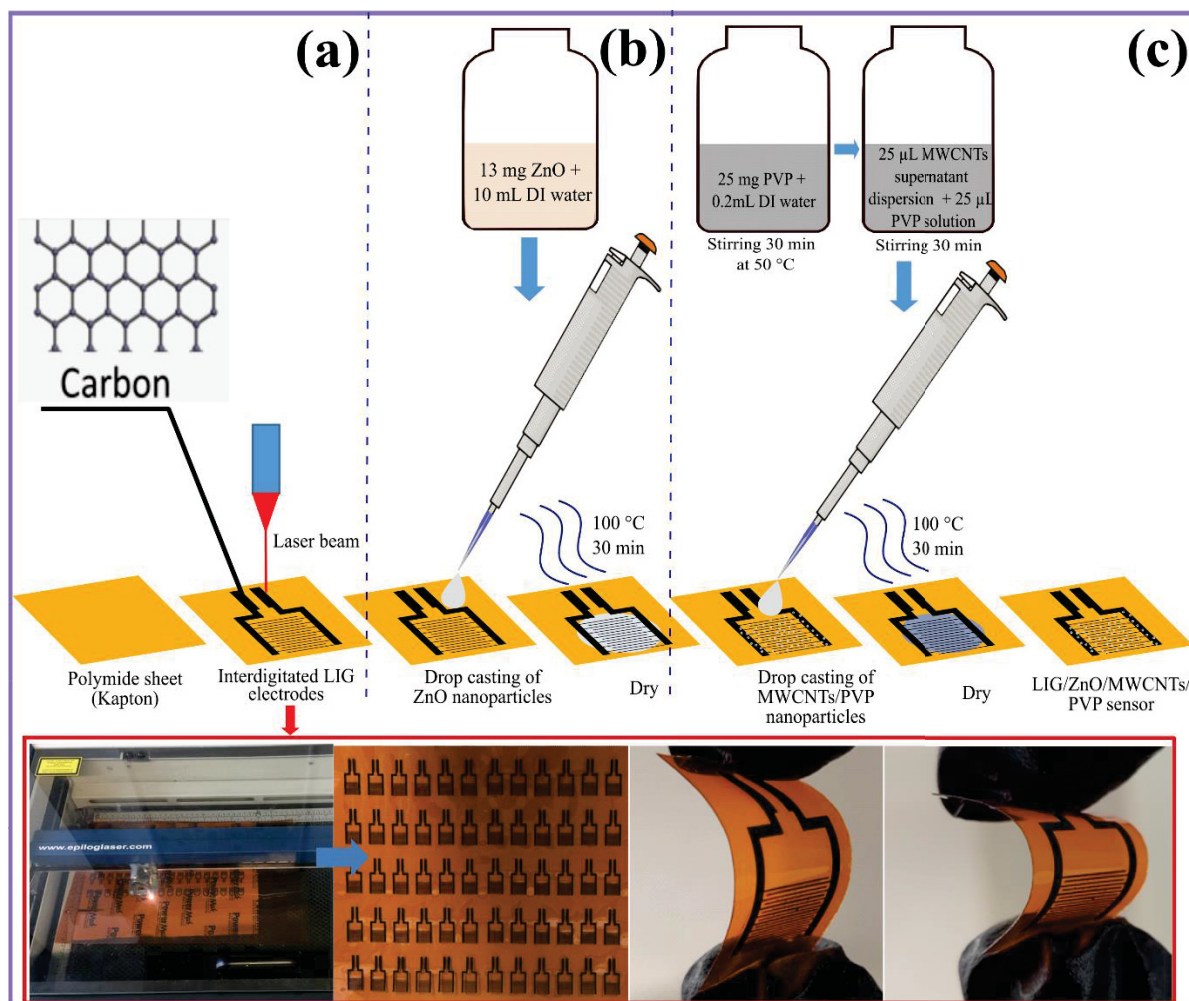
Figure 31 – (a–c) Schematic illustration of the sensor fabrication. The inset provides an image of laser machine and flexible interdigitated LIG electrodes on Kapton sheet.

On the other hand, dynamic measurements of gas sensing responses of the sensors were carried out using the experimental setup depicted in Figure 32. The chamber contained three fans to homogenize the volatiles. During the test, the sensor was placed inside a test chamber and exposed to gas flows containing analyte vapors of known concentration, which were generated using a bubbler system. In the initial stage, the bubbler mass flow controller (MFC) was turned off (line 1). As a result, the flow of nitrogen gas (99.9% purity) served as the reference gas and was controlled using a rotameter (line 2). The MFC regulated the flow of nitrogen carrier gas through the bubbler line, which contained the liquid analyte, providing a known flow rate of saturated vapor. Simultaneously, the flow rate of the dilution gas in the line 2 was controlled by the rotameter. This gas stream was mixed with the saturated vapor flow (line 1) to achieve the desired concentration of the total gas flow. By adjusting the relative flow rates of both lines, a vapor with a known analyte concentration was generated and delivered to the sample, while monitoring its electrical resistance using an Agilent 4284A LCR at 100 Hz

with a bias voltage of 0.5 V. The concentration of ethanol and acetone vapors, calculated using a method described elsewhere[186,187], was maintained at 200 ppm. Finally, pure nitrogen was used to flush the sample chamber by solely utilizing the nitrogen flow from the second line.
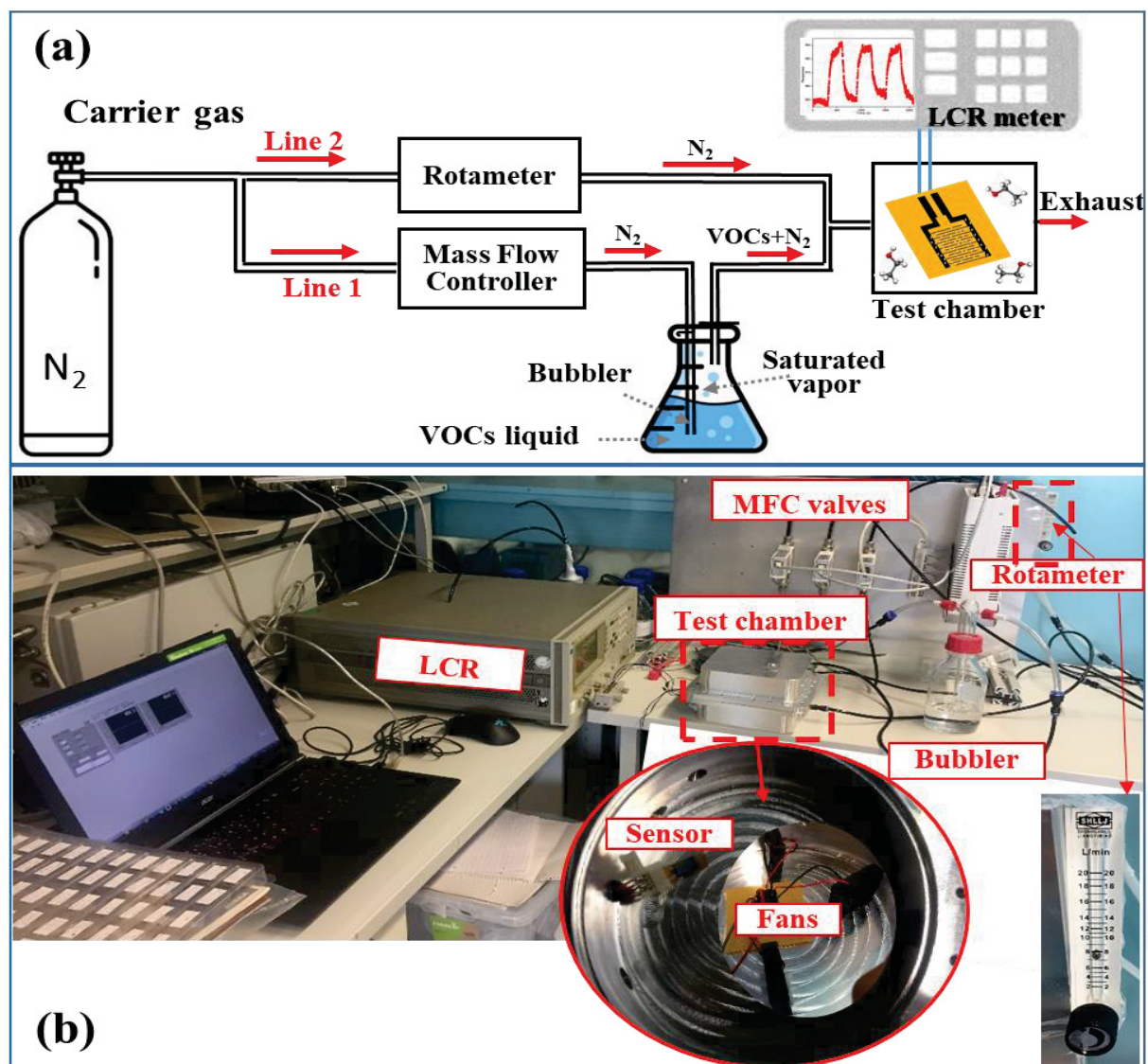
Figure 32 – Delivery of vapors with known analyte concentration to the test chamber: (a) Illustration of the bubbler system, (b) photographic image depicting the experimental setup utilized for measuring the response and recovery times. Inset: Internal view of the test chamber.

4.3 CHARACTERIZATION OF THE FILMS

The intrinsic and extrinsic structural morphology features of the LIG/ZnO/MWCNTs and LIG/ZnO/MWCNTs/PVP sensors were examined using various techniques available at the UFPR (Universidade Federal do Paraná). Transmission electron microscopy (TEM) was conducted using a JEOL JEM 1200EX-II operated at 120 kV, while scanning electron

microscopy (SEM) was performed using a TIESCAN VEGA3 LMU operated at 15 kV. Additionally, the samples were further investigated to determine their elemental composition through electron probe mapping, using energy dispersive X-ray spectroscopy (EDS) with the Oxford EDS system, which was coupled to the SEM.

To investigate the crystallographic phases and structural nature of LIG/ZnO/MWCNTs and LIG/ZnO/MWCNTs/PVP, X-ray Powder diffraction (XRD) using a D8 ADVANCE (BRUKER) was employed, along with comparison to the results obtained from EDS analysis. Additionally, to evaluate the graphitic nature of the nanomaterials, laser Raman spectroscopy was employed using a WITEC ALPHA 300R. This technique enabled the examination of the developed LIG on the Kapton polyimide (PI) sheet and provided valuable insights into its structural information.

4.4 RESULTS AND DISCUSSION

4.4.1 Morphological characterization and analysis of structural features of the LIG/ZNO/MWCNTs and LIG/ZNO/MWCNTs/PVP film

In order to illustrate the design of the devices and provide detailed structural characteristics of the LIG electrodes, Figure 33a,c illustrates the interdigitated electrode configuration. Each device comprises 9 pairs of electrode strips, each with a length of 10 mm, a width of 0.1 mm and a gap of 0.2 mm. These electrode strips collectively form an active area of approximately 34 mm². Porous electrodes have the advantage of an increased effective active area[119] compared to ENIG electrodes. Furthermore, Figure 33b displays a top-view SEM image showcasing the pattern of the LIG electrodes, which consistently aligns with the direction of laser movement during the fabrication process. Additionally, this image highlights the materials deposited between and on the electrodes, such as ZnO/MWCNTs (as shown in Figure 33b) or ZnO/MWCNTs/PVP, referred to as zones A and B.

The SEM images of the cross-section of LIG (Figure 33d) clearly demonstrate a three-dimensional porous carbon structure with a distinct thickness on the PI sheet. This observation indicates that the entire volume of the LIG consists of highly porous materials. Importantly, the remaining PI material beneath the LIG layer serves as mechanical support[156], ensuring that the integrity of the PI film remains intact even after the laser writing process.
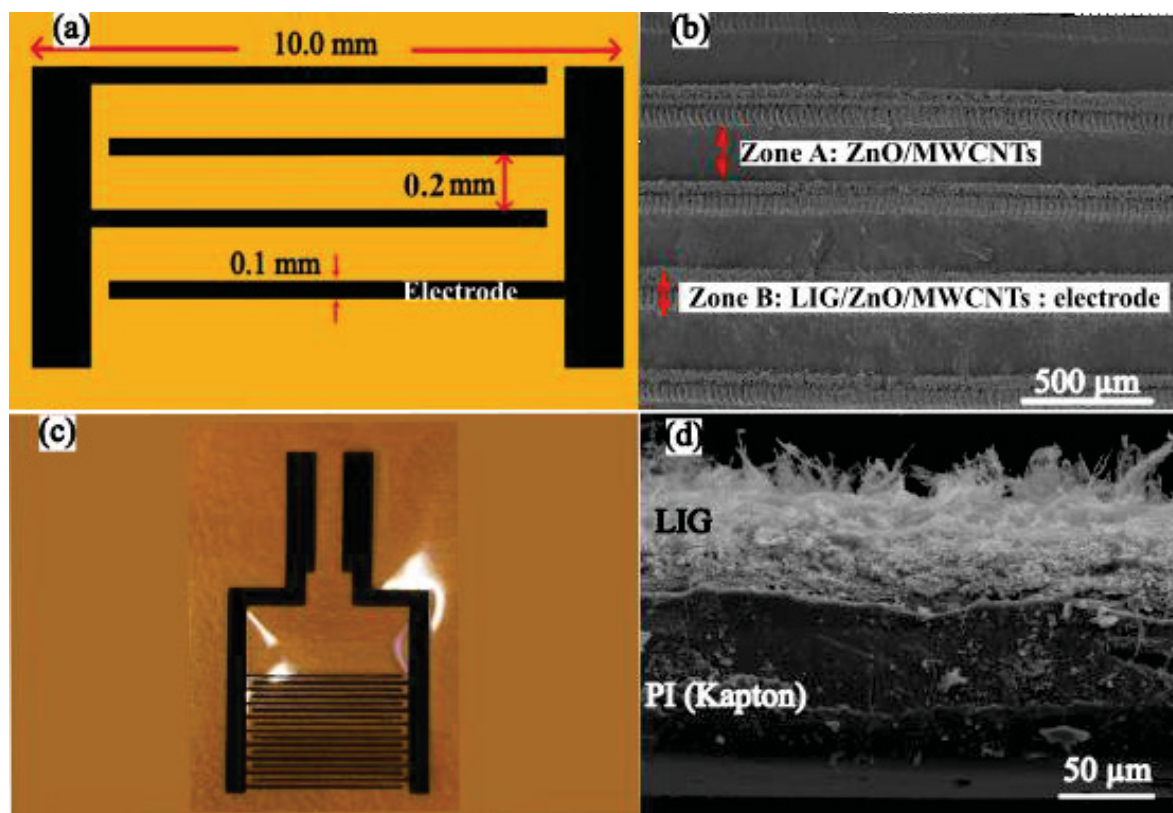
Figure 33 – (a,c) Illustration of electrodes and (b, d) SEM micrograph of the LIG electrodes.

On the other hand, Figure 34 showcases the morphology of the materials on the PI sheet, characterized through SEM and TEM micrographs. Zones A (ZnO/MWCNTs, ZnO/MWCNTs/PVP) and B (LIG/ZnO/MWCNTs, LIG/ZnO/MWCNTs/PVP) are depicted in subfigures (a, d) and (b, e), respectively.

The SEM micrographs of Zone A reveal the structural shape of ZnO and nanotubes deposited on the substrate, exhibiting a rougher texture. In contrast, the morphology of Zone B appears porous in texture, presenting a three-dimensional perspective, as illustrated in Figure 34b, e. Notably, the presence of ZnO nanoparticles is not discernible on the LIG electrodes, suggesting that the latter may function similar to a sponge. Furthermore, in zone B, a distinct and dense porous structure is clearly visible, as depicted in Figure 34b, c. This structure is directly associated with the LIG, and the high magnification image reveals an intricate network of circular pores with varying sizes. The formation of this porous structure is attributed to the rapid release of gaseous by-products during the carbonization process of the PI under laser irradiation[188]. These porous structures significantly increase the accessible surface area and facilitate the infiltration of sensing materials into the electrodes, thereby enhancing their overall performance[159,189].

Additionally, the TEM micrograph in Figure 34c,f and Figs. A4 –A8 (Appendix 1), reveals the presence of LIG, MWCNTs, ZnO particles, and carbon particles. These materials appear to be encapsulated in a matrix with a smooth surface, particularly evident in the devices fabricated with PVP (Figure 34f).
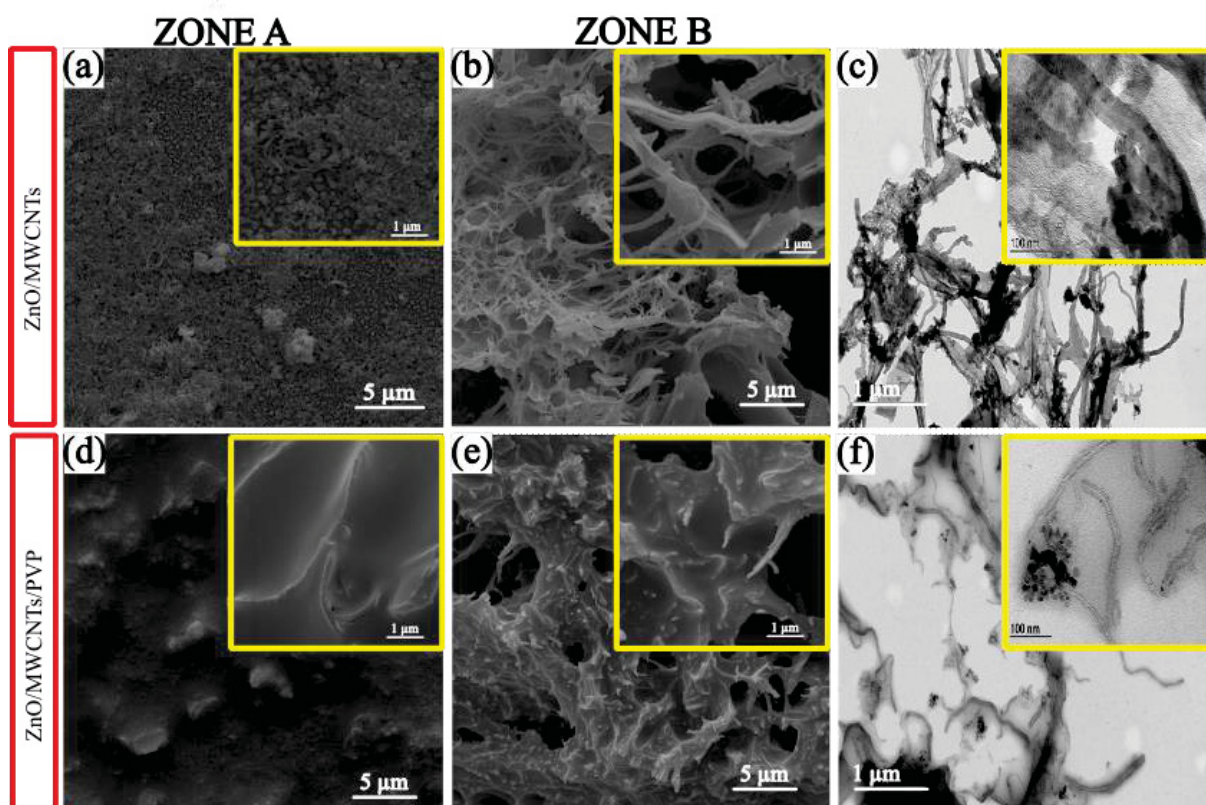
Figure 34 – Morphological SEM images of zone A and B of the LIG electrode, (a) ZnO/MWCNTs, (b) LIG/ZnO/MWCNTs, (d) ZnO/MWCNTs/PVP and (e) LIG/ZnO/MWCNTs/PVP compound. (c and f) TEM images of LIG/ZnO/MWCNTs and LIG/ZnO/MWCNTs/PVP compound respectively.

4.4.2 Elemental mapping and analysis of devices

The sensing materials underwent EDS analysis, and the results are presented in Table 10 and Appendix 1 (Figs. A2 and A3). The EDS analysis confirmed the presence of carbon (C), zinc (Zn), and oxygen (O). The data clearly indicate that as the LIG content increased in Zone B, the percentage of carbon also increased. When examining the samples with PVP, it was observed that both Zone A and Zone B had similar concentrations of zinc oxide (ZnO). However, in the samples without PVP, Zone A exhibited a significantly higher content of zinc compared to Zone B. This suggests that PVP has a passivating effect on the LIG and helps to homogenize the content of the sensing materials between Zone A and Zone B.

TABLE 10 – Elemental analysis of the LIG/ZnO/MWCNTs and LIG/ZnO/MWCNTs/PVP

	Wt%			
	ZnO/MWCNTs (Zone A)	LIG/ZnO/MWCNTs (zone B)	ZnO/MWCNTs/ PVP (Zone A)	ZnO/MWCNTs (Zone A)
C	49.5	82.4	60.7	79.7
Zn	31.8	10.8	14.7	14.4
O	18.6	6.8	14.6	5.8

4.4.3 Raman spectroscopy analysis of sensing materials

Raman spectroscopy was used to confirm the graphene-like structure of the interdigitated electrodes because this technique allows us to observe the characteristic behavior of few-layer graphene that emerges following laser treatments[190–192]. In all spectra, including pure LIG and LIG activated with ZnO/MWCNTs and PVP, three intensity peaks characteristic of graphene were observed. These peaks are the D peak, located at 1356, 1348 and 1352 cm^{-1}, the G peak, observed at 1592, 1588 and 1594 cm^{-1}; and the 2D peak, identified at 2685, 2681 and 2688 cm^{-1} for pure LIG, LIG/ZnO/MWCNTs, and LIG/ZnO/MWCNTs/PVP, respectively. Figure 35 illustrates the presence of these characteristic peaks, which provide insights into the graphenization of LIG and can be compared with those reported in the literature (D, G, and 2D bands observed at approximately 1350, 1580, and 2700 cm^{-1}, respectively)[192]. Furthermore, there are additional modes observed in the spectra of graphene materials, which arise from multi-phonon processes. These modes include D + D″, D + D′, and 2D′, and they are commonly observed in graphene spectra[174].

The D peaks serve as indicators of the presence of defects like vacancies, grain boundaries[193], and amorphous carbon species[194]. The D band specifically represents a mode associated with carbon atoms bonded in a sp^3 configuration. Interestingly, in graphite and high-quality graphene, the D band is typically quite faint. Furthermore, this intensity can also serve as a gauge to determine the degree of functionalization when graphene undergoes chemical modifications[195]. Whereas the G band, known as Rayleigh scattering, is the primary Raman peak[191] and the most prominent characteristic of graphene. It corresponds to the doubly degenerate phonon mode associated with the in-plane vibrations of carbon atoms within a graphene sheet [196]. This mode is closely linked to the sp^2 carbon network and the number of graphene layers, with the intensity of the peak increasing as the number of layers increases[197]. Additionally, the 2D peak (also referred to as the G' band)[198] represents a second-order scattering process that arises from the coupling of two phonons. It is associated with the

overtone of the D band. Importantly, the 2D peak is consistently strong in graphene, even in the absence of the D band, and it does not indicate the presence of defects[195].
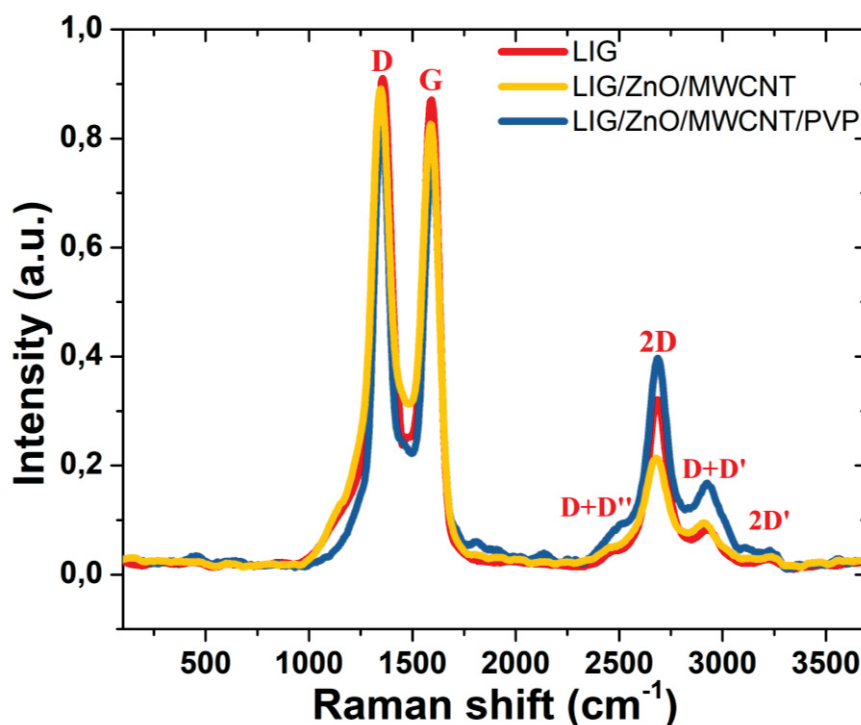
Figure 35 – Raman spectra at 532 nm photon excitation of LIG, LIG/ZnO/MWCNTs and LIG/ZnO/MWCNTs/PVP.

Consequently, the structural characteristics of LIG can be elucidated by analyzing the intensity ratios of its D, G, and 2D bands[199]. The G peak height serves as a reference point for comparing the heights of the D and 2D peaks (I_D/I_G) and (I_{2D}/I_G)[200]. The ratio of the D-to-G peak heights is commonly utilized to quantify the amount of disordered graphene and/or graphite, thereby indicating the quality of the LIG product. In simpler terms, the I_D/I_G ratio can be correlated with the degree of graphitization in the material[201]. Moreover, the I_{2D}/I_G ratio is inversely proportional to the number of layers present in the material[197].

The (I_D/I_G) and (I_{2D}/I_G) values obtained for the pure LIG, LIG/ZnO/MWCNTs and LIG/ZnO/MWCNTs/PVP, are presented in Table 11, indicating the presence of distinct graphene layers[190]. The D peak displays a higher intensity compared to the G peak, whereas the 2D peak shows a moderate height. This observation indicates a significant degree of graphitization for the D peak and a moderate level of graphenization for the 2D peak. These findings suggest the presence of graphene disorder or surface defects[192]. The prominent peaks observed in the LIG samples can be attributed to the reduced coverage of ZnO/MWCNTs and ZnO/MWCNTs/PVP on the porous surface of LIG.

TABLE 11 – The I_D/I_G and I_{2D}/I_G ratios from the Raman spectra of investigated materials

Sample	I_D/I_G	I_{2D}/I_G
LIG	1.043	0.365
LIG/ZnO/MWCNTs	1.078	0.255
LIG/ZnO/MWCNTs/PVP	1.078	0.515

The intensity of the 2D peak decreases as the number of layers increases[197]. Single-layer graphene can also be identified by examining the intensity ratio between the 2D and G bands. For high-quality single-layer graphene, the I_{2D}/I_G ratio is typically greater than or equal to 2[195]. Conversely, I_{2D}/I_G ratio values below 1 in pure LIG, LIG/ZnO/MWCNTs, and LIG/ZnO/MWCNTs/PVP samples indicate the presence of graphene with multiple layers.

The estimation of the graphene domain size can be achieved by calculating the intensity ratio I_D/I_G, utilizing the Tuinstra-Koenig relation, specifically equation 4.1[202].

$$L_\alpha(nm) = (2.4 \times 10^{-10})\lambda_{laser}^4 (I_D/I_G)^{-1} \tag{4.1}$$

Where, λ_{laser} is the excitation laser wavelength (λ_{laser} = 532 nm) and $L\alpha$ is the crystallite size of the samples. $L\alpha$ calculated for the samples pure LIG, LIG/ZnO/MWCNTs and LIG/ZnO/MWCNTs/PVP, were 18.43, 17.83 nm and 17.83 nm, respectively.

4.4.4 X-ray Diffraction analysis (XRD)

To investigate the impact of the preparation method on the crystalline form and chemical composition of the sensing materials, two types of sensors were fabricated: Device 1 (LIG/ZnO/MWCNTs/PVP) and Device 2 (LIG/ZnO/MWCNTs). X-ray diffraction (XRD) analysis was conducted to compare the diffraction patterns of these sensors (Figure 36 and Figure 37) with the X-ray powder diffraction patterns of each individual powder material used in device fabrication, including Kapton (Figure 36c), MWCNTs (Figure 37c), CTAB surfactant (Figure 37d), ZnO (Figure 36b), and PVP (Figure 37b). The obtained XRD patterns for each material were consistent with the reported XRD patterns found in the literature. However, upon comparing these materials with those found in devices 1 and 2, only the crystal patterns of Kapton and ZnO were detected. Therefore, the sample preparation method did not alter the crystalline form of these materials or introduce any artifacts into the diffraction patterns, as

demonstrated in Figure 36. On the other hand, this result confirms the anticipated behavior, which suggests that only materials with well-defined crystal patterns can be detected. Clear observation of LIG patterns in the devices, as well as their comparison with powdered LIG, was impeded due to the challenge of extracting an adequate amount of powdered sample from the LIG electrodes. Additionally, it is worth noting that no theoretical spectra of LIG could be found in the available literature. Figure 36b illustrates the phase purity of ZnO as determined by the XRD pattern. The XRD TOPAS software[203] accurately identified all diffraction peaks, confirming the presence of a hexagonal crystal structure.
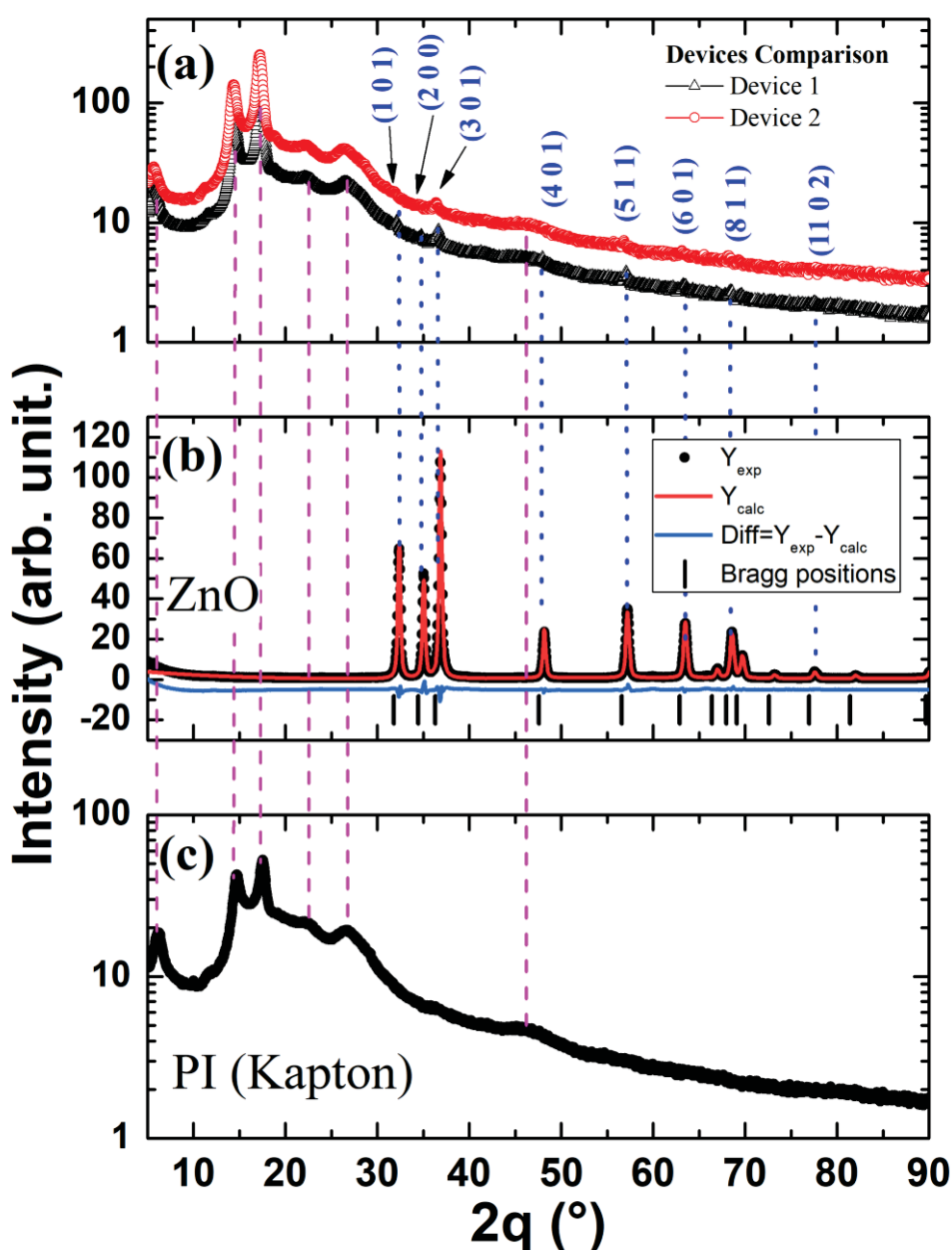
Figure 36 – XRD spectra of the sensors and crystalline materials
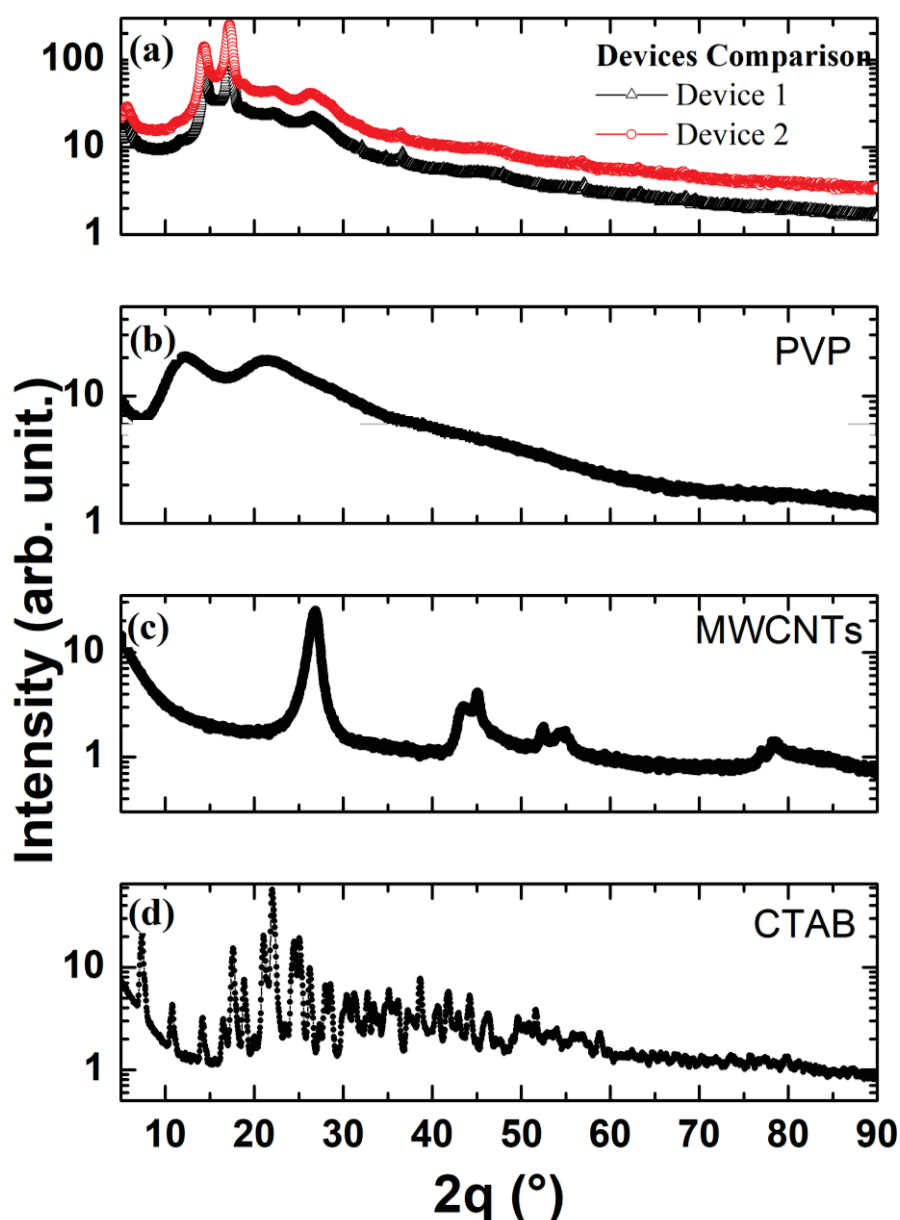
Figure 37 – XRD spectra of the sensors and non-crystalline materials

To determine the crystallite sizes of ZnO, the refinement method depicted in Figure 38 was employed. The indexed peaks with the highest intensities were identified as (101), (200), and (301). Crystallite sizes of ZnO were found to be 39.9 nm in device 1 and 24.0 nm in device 2. The sharp and well-defined diffraction peaks indicate a high level of crystallinity in the samples, and the absence of peaks from other materials confirms their purity. On the other hand, grains within the layers that have sizes of approximately 30 nm exhibit a significant improvement in sensor response, which can be attributed to their highly porous nature. This porosity enables the infiltration of gases into the thin film-sensitive layers, leading to an amplified sensor sensitivity[204].
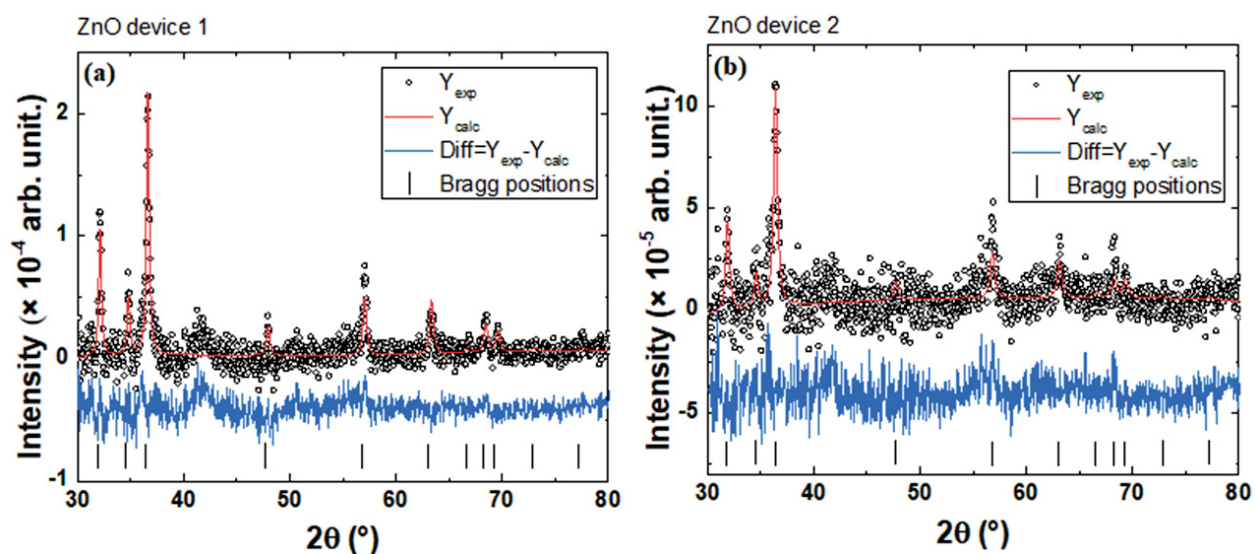
Figure 38 – The output from the refinement analysis of the XRD pattern for ZnO in device 1 and 2. The difference between the experimental data and the calculated data is shown at the bottom.

4.4.5 Performance of the VOCs sensors

Resistance measurements of the sensors

In this study, three sensors were utilized for each individual analyte (ethanol and acetone), resulting in a total of six sensors for each tested material (LIG/ZnO/MWCNTs and LIG/ZnO/MWCNTs/PVP). Figure 39 depicts the real part of impedance of the sensors plotted against the frequency for the respective sensing materials (LIG/ZnO/MWCNTs and LIG/ZnO/MWCNTs/PVP), demonstrating a consistent inverse relationship between real part of impedance and frequency across all samples, regardless of the analyte. The behavior exhibited in the study aligns with the charge transport characteristics of disordered materials[143]. At high frequencies, the movement of charge carriers becomes limited, confining them to short distances, likely restricted within the nanostructure. Consequently, they are unable to effectively follow the oscillating signal. On the other hand, at low frequencies, the charge carriers track the alternating electric field, enabling them to travel relatively long distances and overcome potential barriers. However, during this process, some charges tend to become trapped on the surface of the nanostructures, such as within pores or voids, leading to a high-resistance state. This behavior has been observed in previous studies[31].
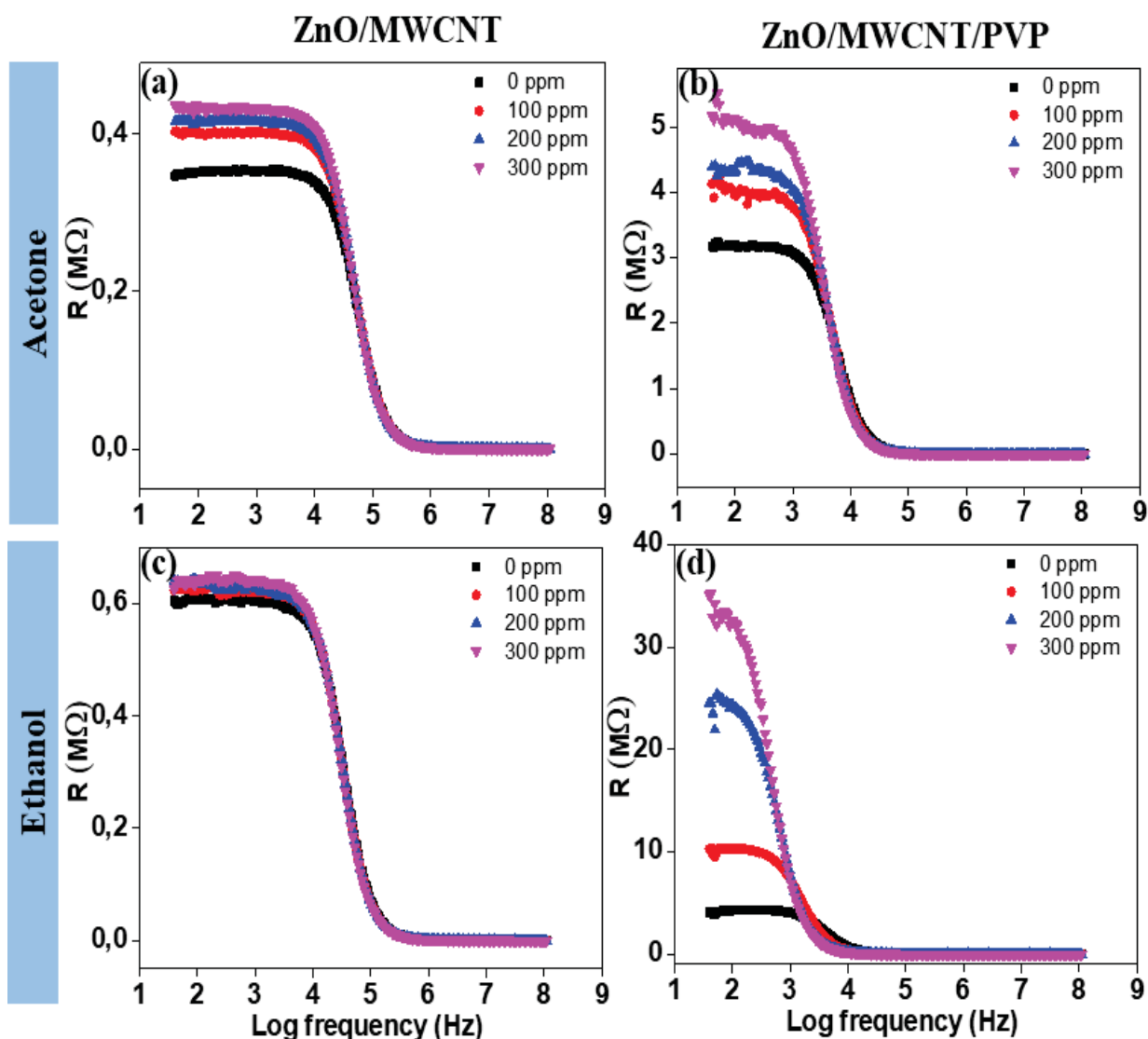
Figure 39 – Sensors' resistance dependence on frequency when exposed to different concentrations of (a, b) acetone, (c, d) ethanol.

Selection of the Optimal Operating Frequency

Investigating the impact of frequency on the real part of impedance of the active materials in the presence of different analytes, the study aimed to determine the optimum working conditions for all devices to achieve higher sensitivity (*S*) (Figure 40). By increasing the operating frequency from 0.1 to 20 kHz, the goal was to identify the frequency that yielded the highest sensitivity.

At lower frequencies, the sensors exhibit the highest sensitivity, primarily due to the dominance of the space charge region in governing the conductivity process. However, as the frequency increases, the sensitivity declines significantly, and the conductivity is instead regulated by the surface charge of the grains[205]. As a result, a single optimum operating

frequency was determined for the entire set of sensors and analytes. Consequently, the best operating frequency for LIG/ZnO/MWCNTs and LIG/ZnO/MWCNTs/PVP-based devices in detecting acetone and/or ethanol was found to be 100 Hz. Although Figure 40c shows that the highest sensitivity is found at 1 kHz, the sensitivity at 100 Hz is not significantly different. Therefore, all sensors were tested at 100 Hz.
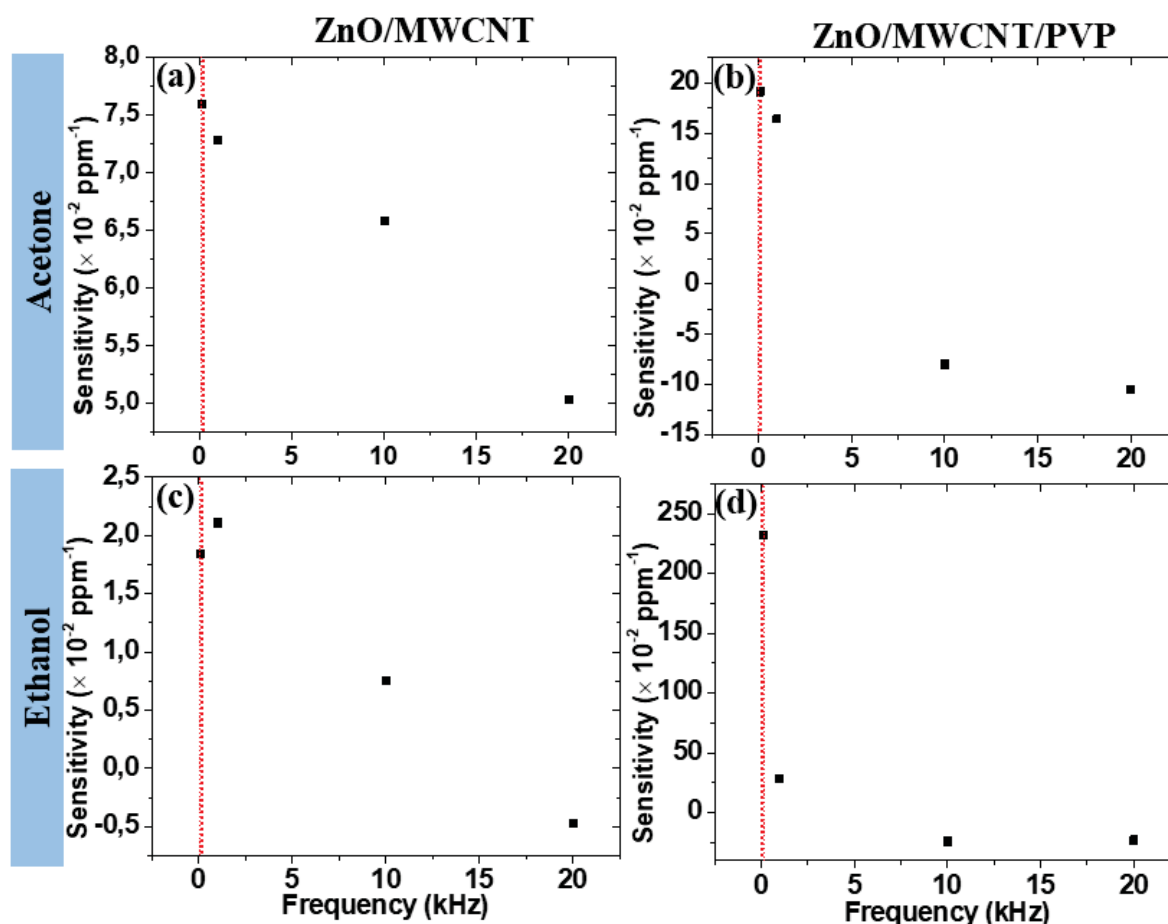
Figure 40 – The sensitivities of sensors data based on LIG/ZnO/MWCNTs and LIG/ZnO/MWCNTs/PVP for acetone and ethanol, as a function frequency; dashed line indicates the optimum operating frequency.

Sensitivity (*S*), Limit of Detection (LoD), Response and Recovery Time of the Sensors

The real part of impedance as a function of analyte concentration was determined for the two materials of interest at a selected operating frequency. Figure 41a,b illustrate these results for acetone, while Figure 41e, f depict the findings for ethanol. Through this analysis, the limit of detection (LoD) and sensitivities (*S*) were estimated. By examining the sensor responses ($\Delta R/R_0$) presented in Figure 41 the sensitivities were determined and employing equation 2.8, the LoD was calculated (as summarized in Table 12). Notably, the sensor responses (Figure 41c,d) exhibited an increase with increasing concentration, indicating a

characteristic p-type semiconducting behavior in these LIG/ZnO/MWCNTs and LIG/ZnO/MWCNTs/PVP-based sensors. This p-type behavior can be attributed to the presence of defects, which act as adsorption sites for gas molecules on the surface, thereby creating shallow acceptor sites[31,206,207].

Figure 42 depicts the response and recovery times for acetone and ethanol. Specifically, in terms of the acetone sensors, both sensors showed similar durations for achieving saturation and recovery. However, the ZnO/MWCNTs/PVP sensor exhibited shorter times, with saturation achieved in 90 seconds and recovery in 255 seconds. In contrast, the other sensor based on ZnO/MWCNTs took 108 seconds to reach saturation and 259 seconds for recovery.

The response and recovery time values are summarized in Table 12. Among the sensors, the ZnO/MWCNTs sensors demonstrated the shortest response and recovery times (< 60 s) for ethanol. This suggests that the ZnO/MWCNTs surface had a higher rate of ethanol absorption and desorption, leading to quicker response and recovery times. These findings confirm the stronger affinity of this material towards ethanol. However, the ZnO/MWCNTs/PVP composite exhibited longer response and recovery times. This can be attributed to the hinderance caused by the PVP polymer functional groups, impeding ethanol transport in the sensor's active layer. This indicates a more pronounced interaction between ethanol vapor and the LIG/ZnO/MWCNTs/PVP surface.

TABLE 12 – Sensitivity (S), limit of detection (LoD), response and recovery time for the detection of acetone and ethanol in sensors based on ZnO/MWCNTs and ZnO/MWCNTs/PVP.

Analytes	Samples	S ($\times 10^{-2}$ ppm^{-1})	LoD (ppm)	t_{resp}/t_{recov} (s)
Acetone	ZnO/MWCNTs	0.076	8	108/259
	ZnO/MWCNs/PVP	0.191	11	90/255
Ethanol	ZnO/MWCNTs	0.018	58	54/55
	ZnO/MWCNTs/PVP	2.319	17	200/279
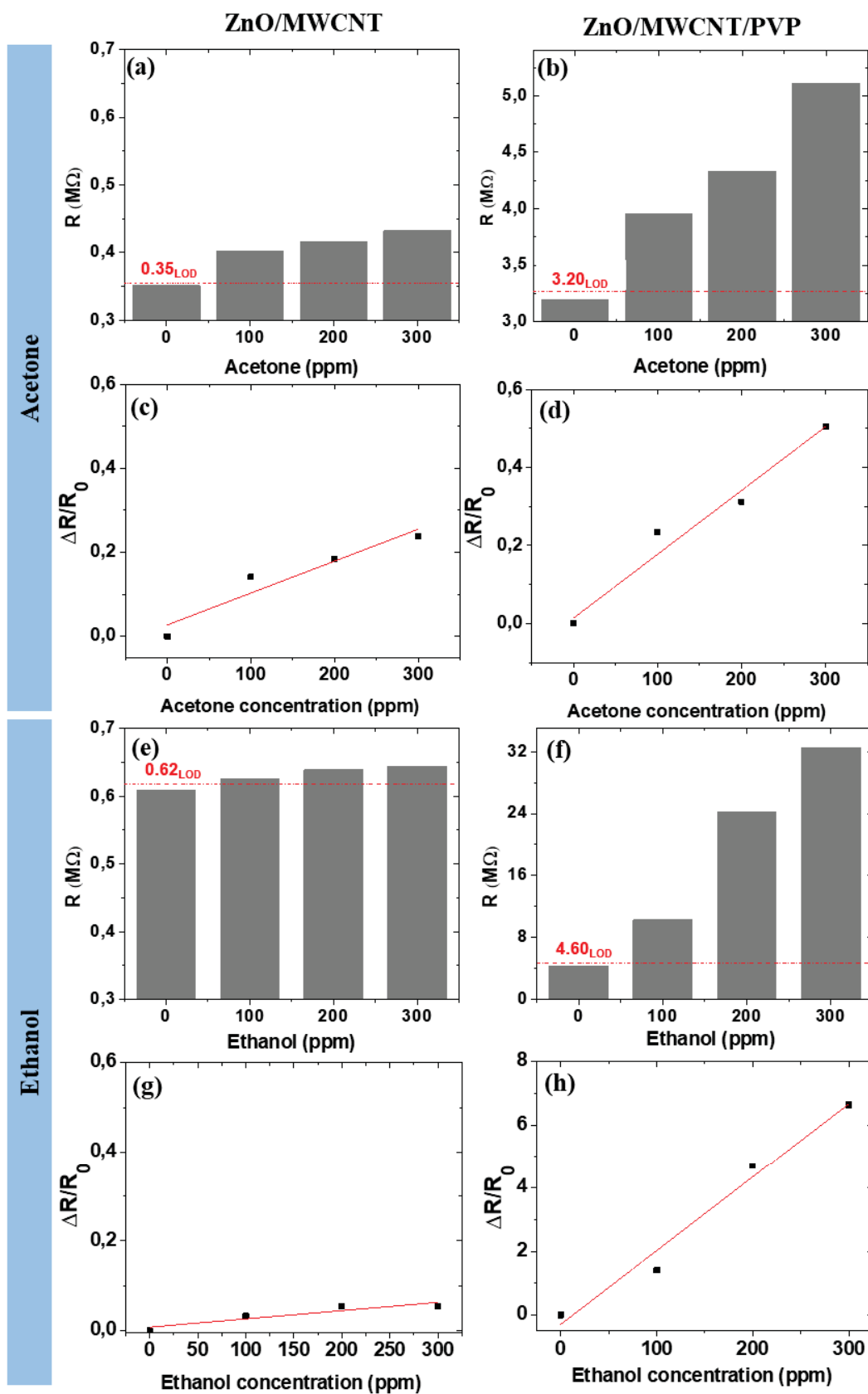
Figure 41 – Data set for sensors based on LIG/ZnO/MWCNTs and LIG/ZnO/MWCNTs/PVP, when exposed to acetone and ethanol at optimum operating frequencies, are presented in the first and second columns, respectively. (a, b, e and f) resistance as a function of analyte concentration and (c, d, g and h) response of the sensor versus analyte concentration; the dotted red line indicates the estimated LoD resistance of the corresponding sensor.
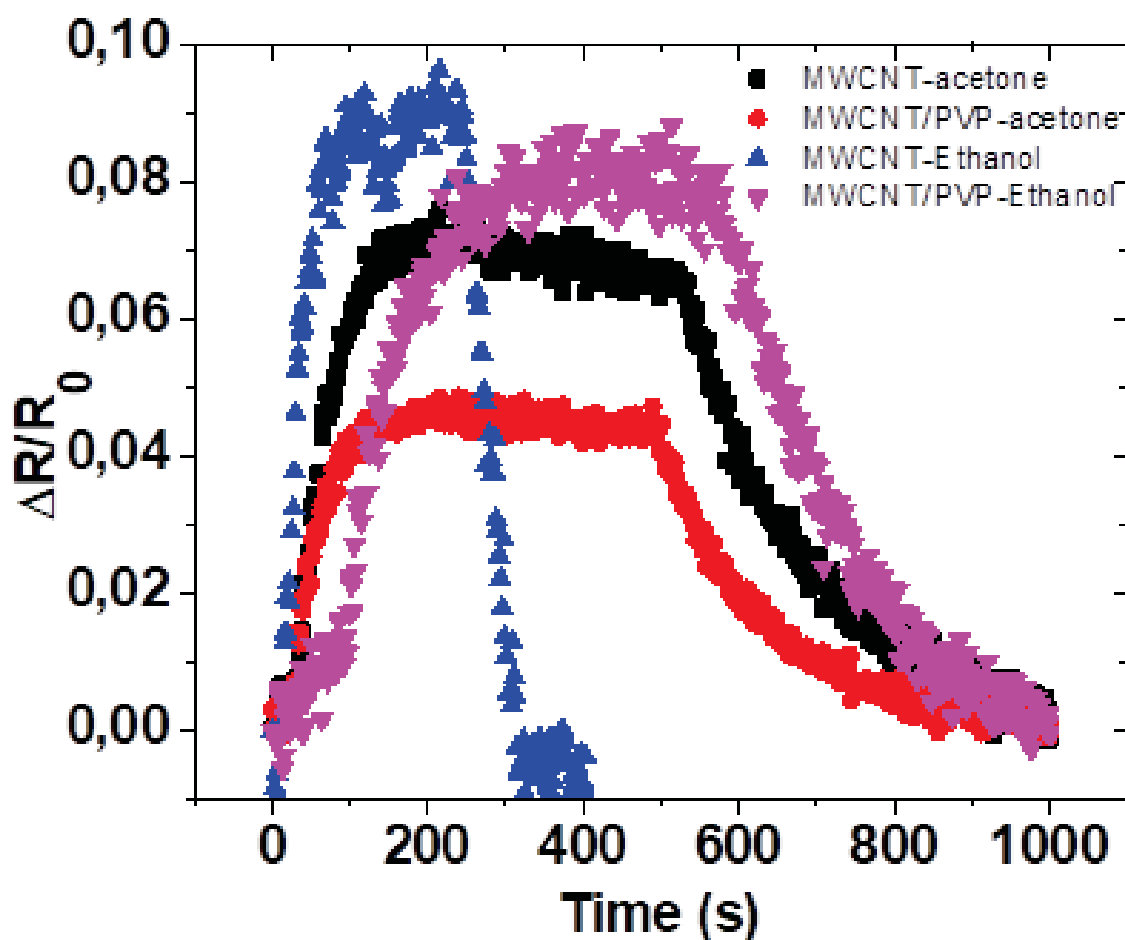
Figure 42 – Responses and recovery times for devices fabricated after exposure and removal of 200 ppm of acetone and ethanol vapors at optimum operating frequencies.

Complex impedance

Figure 43 to Figure 46 display the changes in the complex impedance spectra (CIS) through Nyquist and Bode plots for LIG/ZnO/MWCNTs and LIG/ZnO/MWCNTs/PVP-based sensors at varying analyte concentrations. The measurements were conducted with a constant sinusoidal applied potential of 0.5 V, while the frequency range was adjusted from 40 Hz to 110 MHz.

The observations indicate that the size of the semicircles in the impedance plots increases with rising analyte concentrations within the test chamber. All sensors exhibit a distinctive Nyquist plot characterized by a single semicircle positioned close to the x-axis. This behavior of a single arc has been reported in various studies involving different metal oxide materials with nano-scale grains[108,208]. It is hypothesized that this phenomenon involves a charge transfer process within the material[119]. The diameter of the semicircle correlates with the charge transfer resistance between the sensing materials and analytes interface. This value

can be estimated from the intersection with the real axis (Z′) at low frequency[209]. Additionally, the shape of the obtained Nyquist curves suggests that the structure under investigation can be modeled by equivalent circuits, enabling the distinction of different contributions from the sensor elements. Initially, the fitting process, and consequently, the resistance and capacitance values, were estimated manually from the experimental curve. Subsequently, these values were refined to their optimal values using the ZView® software from Scribner Associates, Inc., version 3.2b.

Figure 43 to Figure 46 depict the fitting curves of the proposed model alongside experimental data. The inset in each Figure 43a to Figure 46a showcases the proposed equivalent circuit model. The impedance spectra are well-matched by an equivalent circuit consisting of parallel *RC* (resistor and capacitor). For the impedance analysis of LIG/ZnO/MWCNTs-based sensors, capacitors were optimally fitted using a constant phase element (*CPE*), while for LIG/ZnO/MWCNTs/PVP-based sensors, ideal capacitors (*C*) were identified.

The model was utilized to estimate the values of the circuit elements under the test conditions, with the results presented in Tables 13 to 16. Considering these findings along with the specimen's morphology and microstructure, an explanation for the sensing behavior is proposed**.**

Considering the well-studied nature of this phenomenon, it is known that at high frequencies, intercepts with the Z' axis correspond to characteristics related to the volume of grains, while the diameter of the low-frequency arc corresponds to the grain boundary resistance[209,210]. Figure 40 (sensitivities at different frequencies) illustrates that the sensitivity to acetone and ethanol vapor is much higher at low frequencies compared to high frequencies. Consequently, it can be concluded that the primary contribution to sensitivity is attributed to processes associated with surface states.

Further examination of the nature of the grain boundary resistance was conducted through analyte concentration-dependent impedance measurements. The high-frequency intercepts of the semi-circular arcs remain constant regardless of the applied analyte concentration. This non-dependence on the concentration of the analyte is clearly illustrated in the inset of the Bode plots (Figure 43b to Figure 46b). In contrast, the diameter of the arc varies with concentration. Specifically, the grain boundary resistance was found to increase with increasing analyte concentration.

The results are consistent with the notion that most chemoresistive sensors rely on surface conductance for operation. These sensors detect variations in surface conductivity, often reflected as changes in electrical resistance, primarily caused by fluctuations in free electron concentration resulting from charge transfers between the sensing material and the analyte during interaction[211]. Moreover, this finding aligns with the classification of materials into two groups based on their operating temperature, which determines their functional mechanism. Materials employing surface conductance effects, such as nanomaterials effective up to 600°C operating temperature, belong to one group, while those relying on bulk conductance effects, suitable for higher operating temperatures (i.e., above 700°C), comprise the other group[49,212,213]. Given that impedance measurements were conducted at room temperature, it is reasonable that no electrical contributions associated with the bulk resistances appear.

On the other hand, no electrical contribution, such as resistance, associated with the interface between the semiconducting sensitive layer and the electrodes, or any potential chemical influence like the activity of the contact material in the region close to the contacts, was identified. The significance of this resistance to the overall sensor resistance value depends on the morphological conditions; typically, this electrical contribution is observed in metallic electrodes[214]. Finally, the sensing layer composed of LIG/MWCNTs/ZnO is loosely connected, and no discernible electrical contributions were observed for each individual component of the structure.
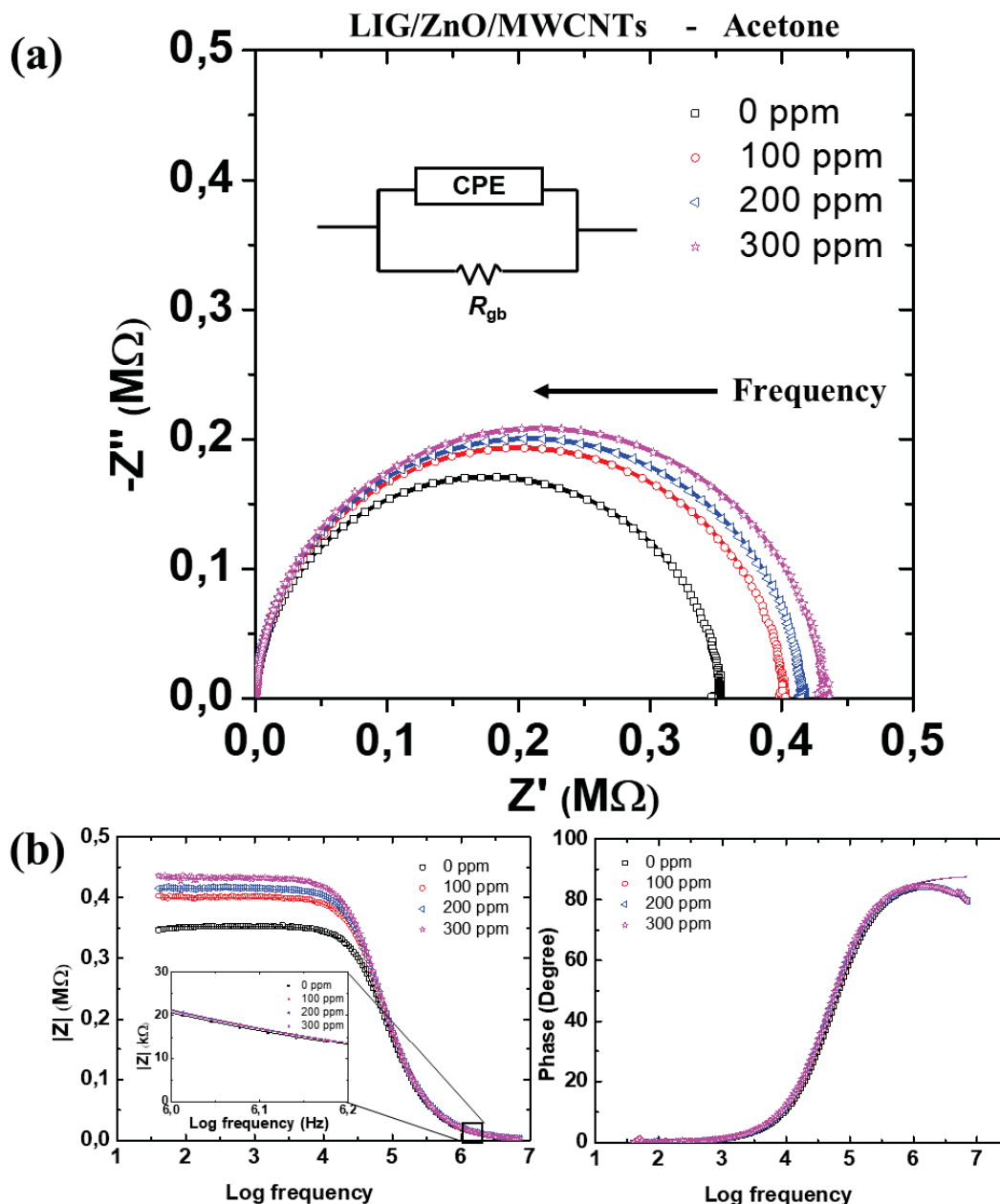
Figure 43 – (a) Impedance spectroscopy Nyquist plots and corresponding equivalent circuit model (inset) of LIG/ZnO/MWCNTs at different concentrations of acetone. Open symbols represent experimental data while continuous lines are the fittings by Zview® software using the proposed equivalent circuit model. (b) Bode plots of LIG/ZnO/MWCNTs at different concentrations of acetone. The Inset highlights the impedance's independence at high frequencies.

TABLE 13 – Z-fit equivalent circuit data of LIG/ZnO/MWCNTs-based sensors at different concentrations of acetone.

Concentration (ppm)	R_{gb} ($\times 10^5$ Ω)	CPE ($\times 10^{-11}$ F s$^{(n-1)}$)	n
0	3.53	1.07	0.98
100	4.00	1.04	0.98
200	4.15	1.05	0.98
300	4.31	1.06	0.98
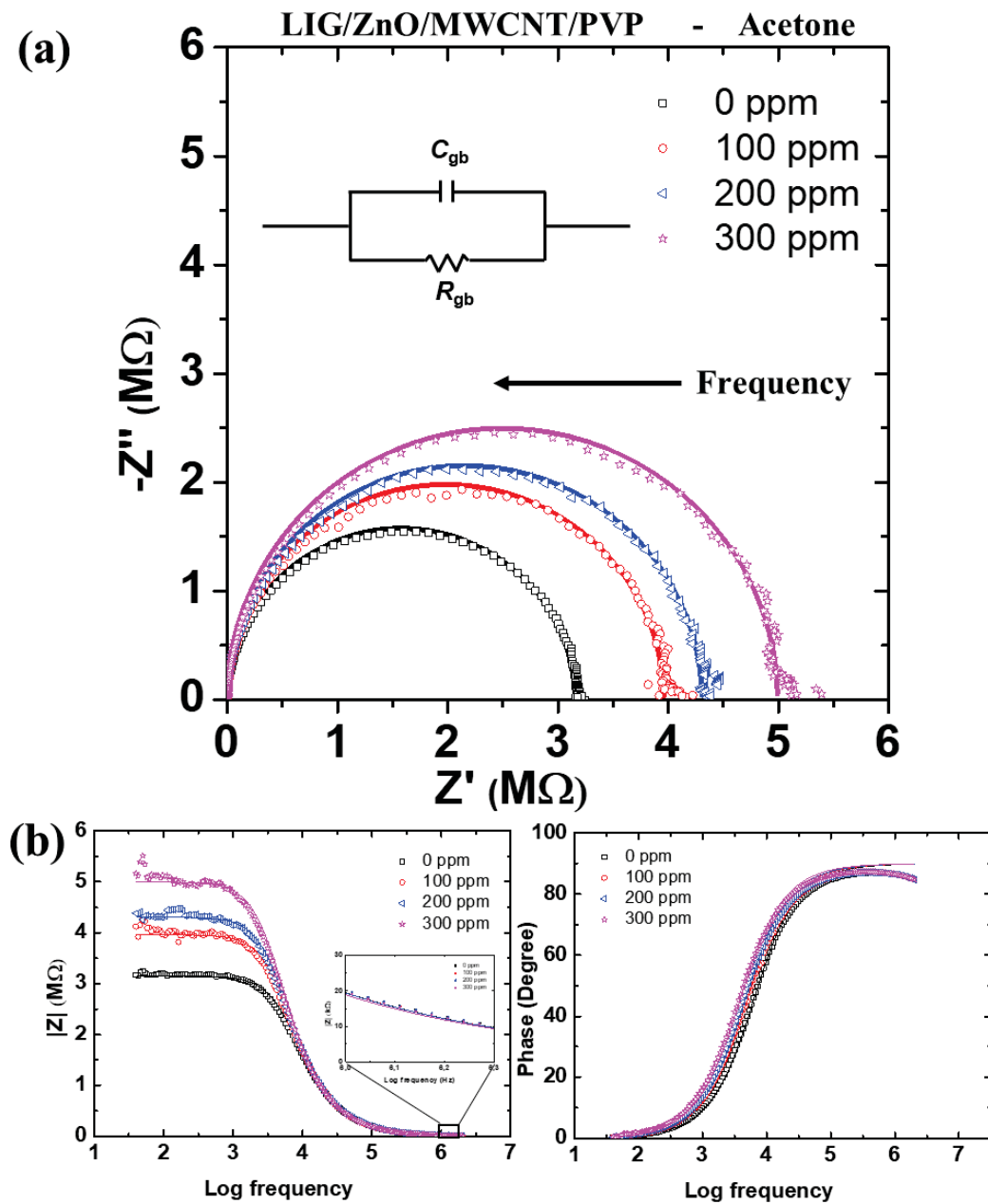
Figure 44 – (a) Impedance spectroscopy Nyquist plots and corresponding equivalent circuit model (inset) of LIG/ZnO/MWCNTs/PVP at different concentrations of acetone. Open symbols represent experimental data, whereas the continuous lines was fitted by EISSA software using the proposed equivalent circuit model, (b) Bode plots of LIG/ZnO/MWCNTs/PVP at different concentrations of acetone. The Inset highlights the impedance's independence at high frequencies.

TABLE 14 – Z-fit equivalent circuit data of LIG/ZnO/MWCNTs/PVP-based sensors at different concentrations of acetone.

Concentration (ppm)	R_{gb} ($\times 10^6$ Ω)	C_{gb} ($\times 10^{-12}$ F)
0	3.15	8.16
100	3.96	8.19
200	4.31	8.19
300	4.99	8.43
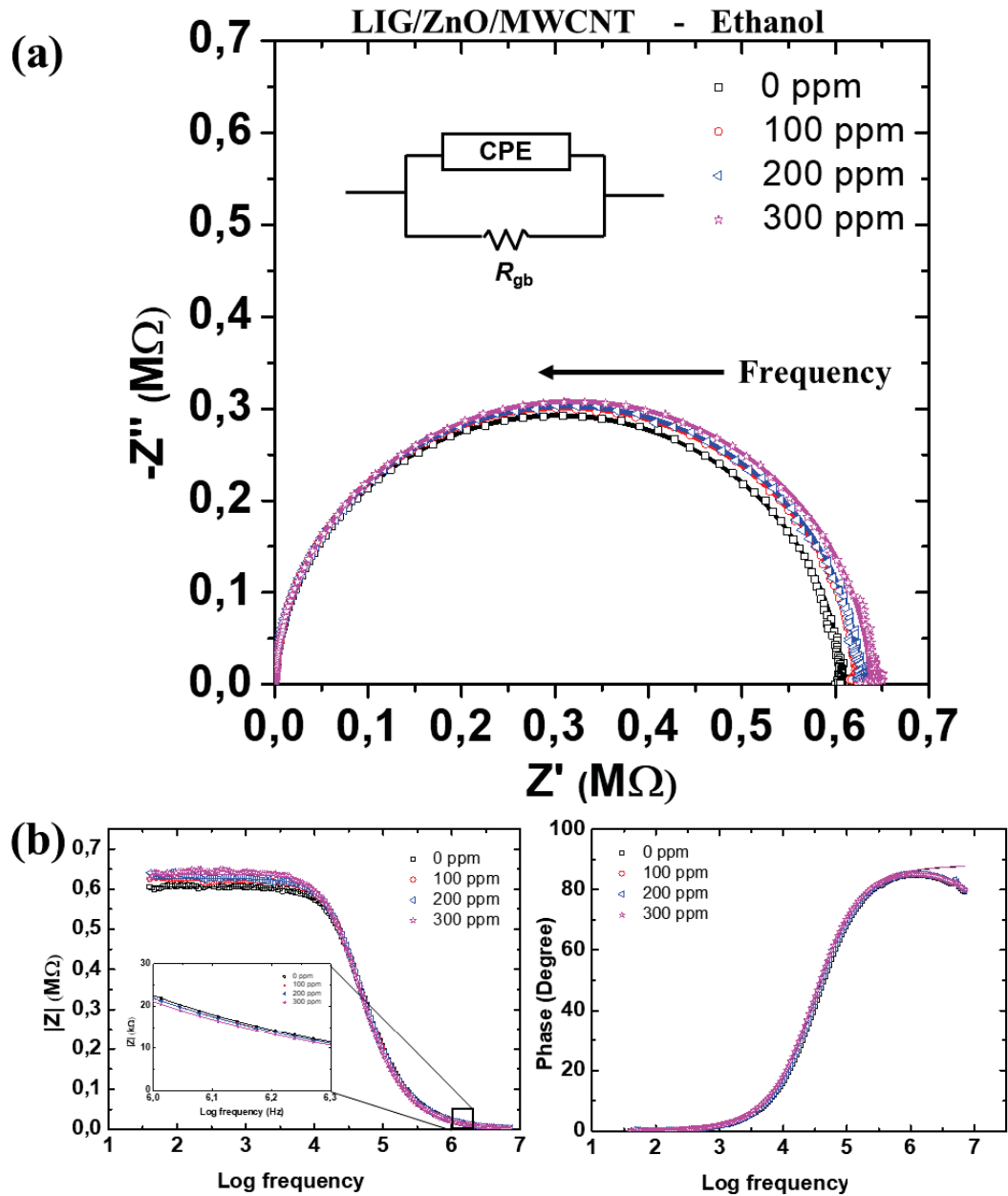
Figure 45 – (a) Impedance spectroscopy Nyquist plots and corresponding equivalent circuit model (inset) of LIG/ZnO/MWCNTs at different concentrations of ethanol. Open symbols represent experimental data. The continuous lines was fitted by EISSA software using the proposed equivalent circuit model (b) Bode plots of LIG/ZnO/MWCNTs at different concentrations of ethanol. The Inset highlights the impedance's independence at high frequencies.

TABLE 15 – Z-fit equivalent circuit data of LIG/ZnO/MWCNTs-based sensors at different concentrations of ethanol.

| Concentration (ppm)	R_{gb} ($\times 10^5$ Ω)	CPE ($\times 10^{-11}$ F s$^{(n-1)}$)	n
0	6.06	1.00	0.98
100	6.23	1.01	0.98
200	6.26	1.01	0.98
300	6.38	1.06	0.98
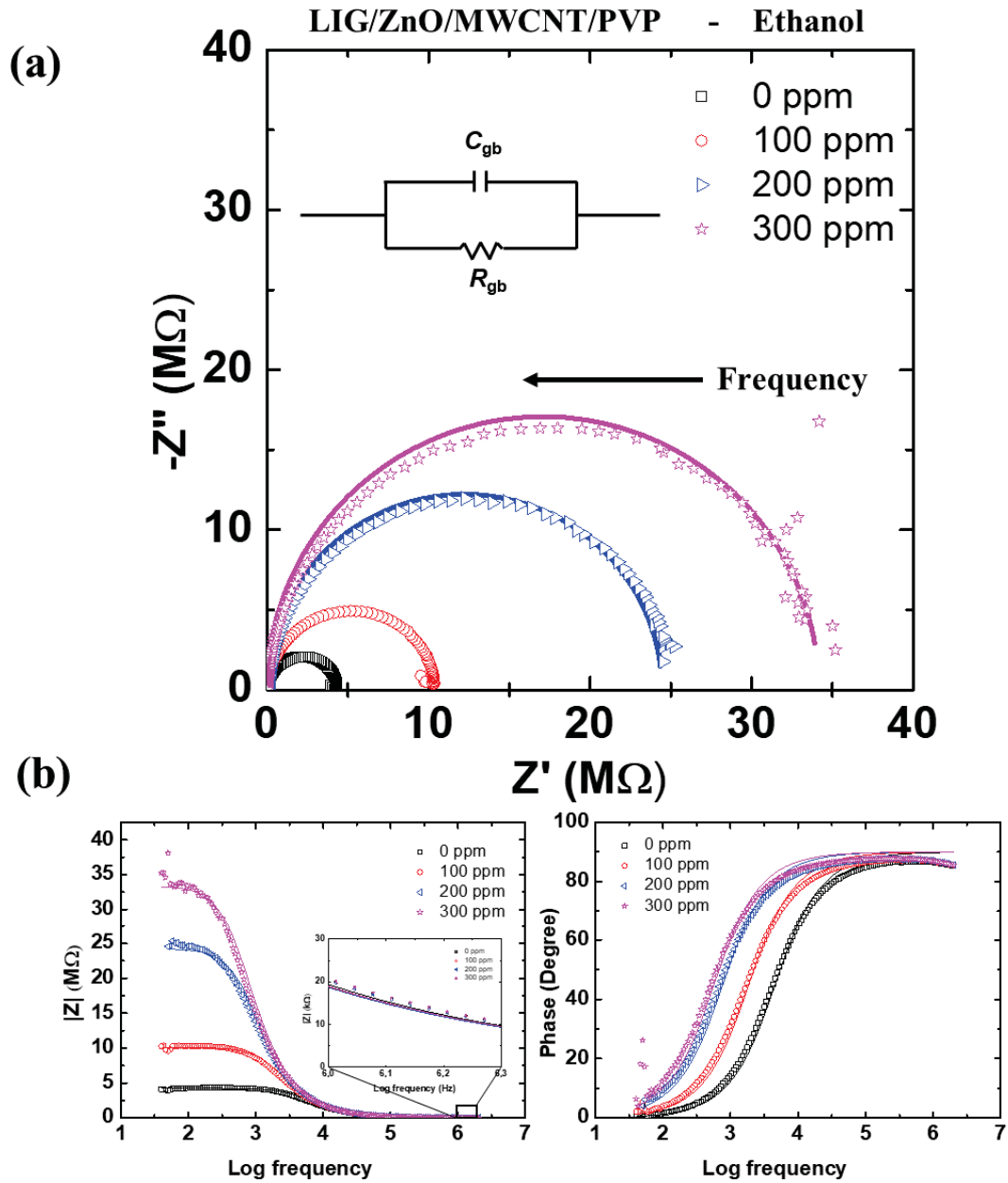
Figure 46 – (a) Impedance spectroscopy Nyquist plots and corresponding equivalent circuit model (inset) of LIG/ZnO/MWCNTs/PVP at different concentrations of ethanol. Open symbols represent experimental data, whereas the continuous lines was fitted by EISSA software using the proposed equivalent circuit model (b) Bode plots of LIG/ZnO/MWCNTs/PVP at different concentrations of ethanol. The Inset highlights the impedance's independence at high frequencies.

TABLE 16 – Z-fit equivalent circuit data of LIG/ZnO/MWCNTs/PVP-based sensors at different concentrations of ethanol.

Concentration (ppm)	R_{gb} ($\times 10^6$ Ω)	C_{gb} ($\times 10^{-12}$ F)
0	4.23	8.20
100	10.10	8.42
200	24.24	8.51
300	33.33	8.37

The LIG/ZnO/MWCNTs-based sensor exhibited a significant increase in the resistance component R_{gb} when exposed to acetone and ethanol, ranging from 353 to 431 kΩ and 606 to 638 kΩ, respectively, as concentrations of these analytes increased from 0 to 300 ppm, documented in Tables 13 and 15. In contrast, the corresponding *CPE* values remained practically unchanged when exposed to acetone and ethanol vapors, hovering around ~10 pF and remains predominantly capacitive (n ~ 1)[212, 114,122,213]. The consistent value of *CPE* and its favorable fit as a constant phase element in LIG/ZnO/MWCNTs-based sensors (Figure 43 and Figure 45), suggest its association with the interfacial contribution to the overall impedance within the equivalent circuit (R_{gb}//*CPE*). *CPE* can be attributed to surface non-uniformity, roughness, and even porosity[216,217]. In each local sub-microscopic area, its own unique RC combination arises. However, macroscopically, the cumulative effect of all these contributions was observed.

Notably, in the R_{gb}//*CPE* component, the primary contribution arises from the resistive component R_{gb} attributed to the reducing effect of acetone and ethanol vapors. This observation indicates that the conduction process is best described by considering that the charge carriers (holes for LIG/ZnO/MWCNTs) must overcome the surface barriers present at the grains' surface in the LIG/ZnO/MWCNTs composite.

It's noteworthy that sensors based on LIG/ZnO/MWCNTs exhibited similar sensing behavior towards acetone and ethanol, with sensitivities of 0.076×10^{-2} and 0.018×10^{-2} ppm^{-1}, respectively. Additionally, these sensors exhibited a LoD of 8 ppm for acetone and 58 ppm for ethanol.

On the other hand, the impedance behavior of the LIG/ZnO/MWCNTs/PVP-based sensors to acetone and ethanol is shown in Figure 44 and Figure 46 and the values of R_{gb} and C_{gb} estimated from the model presented in Tables 14 and 16, respectively. Interestingly, the *CPE* (constant phase element) component does not appear, suggesting that the PVP acts as a passivation layer, reducing the roughness of the layer. This observation aligns with the SEM images (Figure 34), where a reduction in surface roughness can be observed.

Similar to LIG/ZnO/MWCNTs-based sensors, an intergranular contact can be represented electronically by a resistor R_{gb} (due to the high resistive depletion layers) and a capacitor C_{gb} in parallel[218] in LIG/ZnO/MWCNTs/PVP-based sensors. The resistance value exhibited a noticeable variation with changes in acetone and ethanol concentrations, while the capacitance value remained relatively constant. Given the lack of significant change in capacitance values, it can be inferred that the analytes primarily affected the surface charge

region of the LIG/ZnO/MWCNTs/PVP compound structures[219]. This capacitive contribution is minimally affected by the analyte charge interactions, likely due to the structures' size not exceeding 60 nm in diameter. Consequently, it can be inferred that the entire particle is in the depletion zone. This observation aligns with findings reported by other authors[220–222], albeit for smaller particles.

In the same way that sensors based on LIG/ZnO/MWCNTs exhibited, the sensors based on LIG/ZnO/MWCNTs/PVP showed similar sensing behavior towards acetone and ethanol, but with higher sensitivities of 0.191×10^{-2} and 2.319×10^{-2} ppm^{-1}, respectively. Additionally, these sensors exhibited a LoD of 11 ppm for acetone and 17 ppm for ethanol. The enhanced sensor response and sensitivity of the LIG/ZnO/MWCNTs/PVP compound can be attributed to the presence of PVP, which facilitates a more uniform dispersion of carbons within the electrode matrix[134]. The role of PVP in achieving this homogeneous dispersion is ascribed to the presence of polar groups in the polymer, such as polyvinylpyrrolidone (PVP), which aids in the dispersion of carbon materials[223]. Furthermore, the use of PVP as an insulating matrix within a conductive material, such as graphene, has been documented to create percolation pathways that enhance electrical response[224]. This combined effect of PVP in promoting homogeneous dispersion and aiding electrical response contributes to the increased sensor performance and sensitivity observed in the LIG/ZnO/MWCNTs/PVP compound.

The sensor's selectivity was evaluated based on the values of the equivalent circuit derived from the experimental Nyquist and Bode plots. These circuit element values were graphically represented, as illustrated in the Figure 47. The clustering of each analyte at varying concentrations further highlights the distinct response of LIG/ZnO/MWCNTs and LIG/ZnO/MWCNTs/PVP to acetone and ethanol vapors. Notably, among the elements of the equivalent circuit, R_{gb} demonstrated more significant differentiation between the types of sensing materials compared to the resistance of the analytes. These findings, depicted in the Figure 48, underscore the synergistic effect of the LIG/ZnO/MWCNTs/PVP compound, resulting in a highly selective and sensitive sensor for acetone and ethanol vapors.
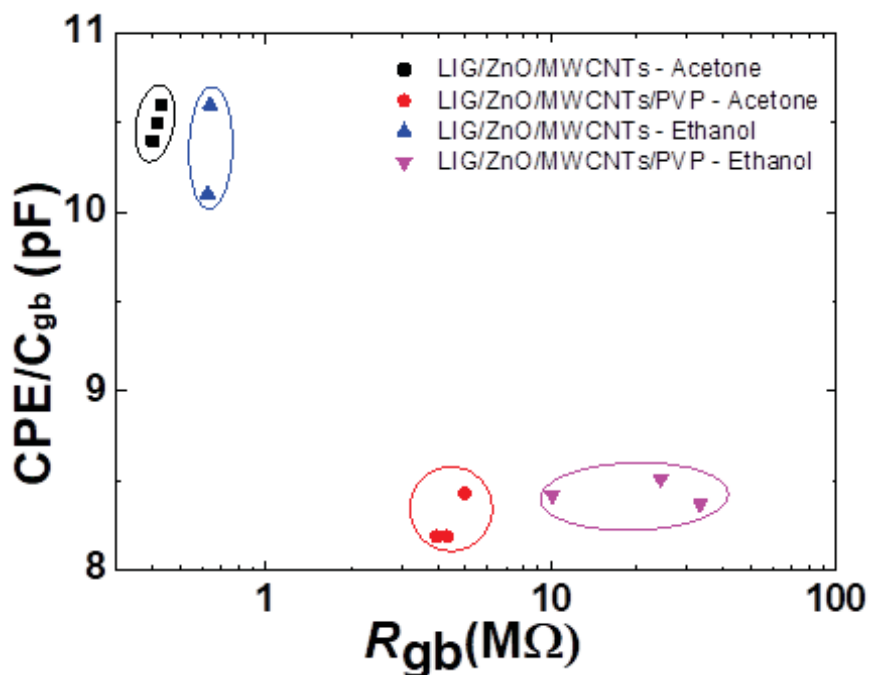
Figure 47 – The values of equivalent circuit elements for LIG/ZnO/MWCNTs and LIG/ZnO/MWCNTs/PVP-based sensors exposed to acetone and ethanol.
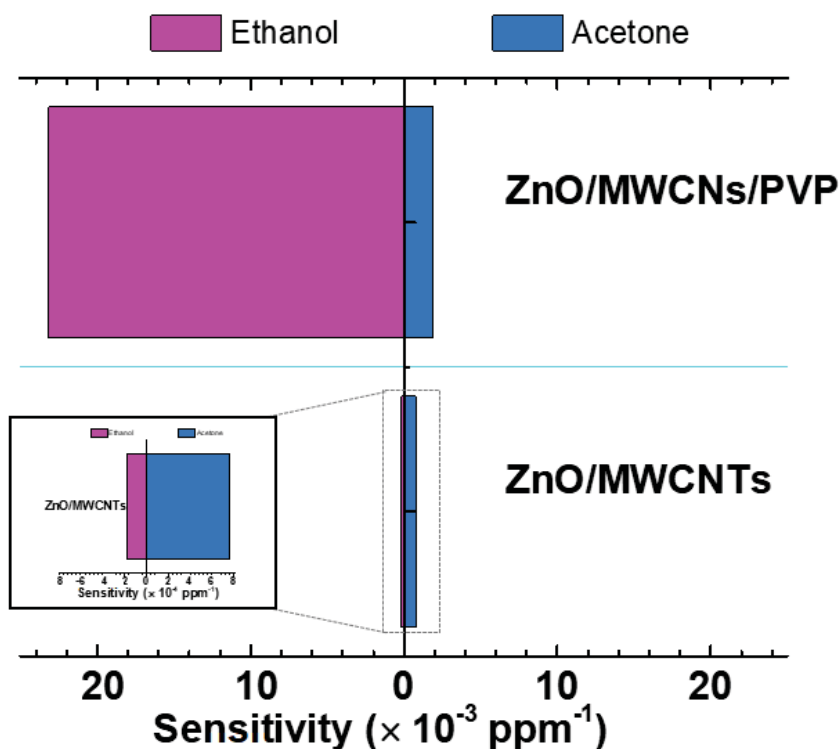
Figure 48 – Comparison of the sensitivities for LIG/ZnO/MWCNTs and LIG/ZnO/MWCNTs/PVP-based sensors, at the operating frequency of 100Hz. The inset is a zoom-in of LIG/ZnO/MWCNTs sensors response.

Upon exposure to the sensing materials inside the chamber, a specific quantity of acetone or ethanol molecules is adsorbed on the surface of the LIG/ZnO/MWCNTs or LIG/ZnO/MWCNTs/PVP. The extent of this adsorption depends on the analyte concentration.

During the adsorption process, electrons are transferred from the analyte molecules to the sensing material due to the difference in electric potential. Consequently, an increase in analyte concentration leads to a reduction in the electrical conductivity of the sensor. These transferred electrons move from the analyte molecules to the LIG/ZnO/MWCNTs or LIG/ZnO/MWCNTs/PVP, where they recombine with holes carriers in the material. This recombination results in a decrease in the majority carriers of the sensing material, ultimately increasing the sample's resistance, as demonstrated in Figure 41. Thus, analyte molecules function as electron donors[225]. These observed changes further confirm that acetone and ethanol vapors affect the grain boundary resistance. The reaction mechanism of acetone and ethanol gas sensing follows a similar pattern to Equations 2.1 to 2.6 and is schematized in Figure 49.

Acetone $CH_3COCH_3 + 4O_{2ads}^- \rightarrow 3CO_2 + 3H_2O + 4e^-$

Ethanol $C_2H_5OH \rightarrow CH_3COH + H_2$

$CH_3COH + 6O_{ads}^- \rightarrow 2CO_2 + 3H_2O + 6e^-$
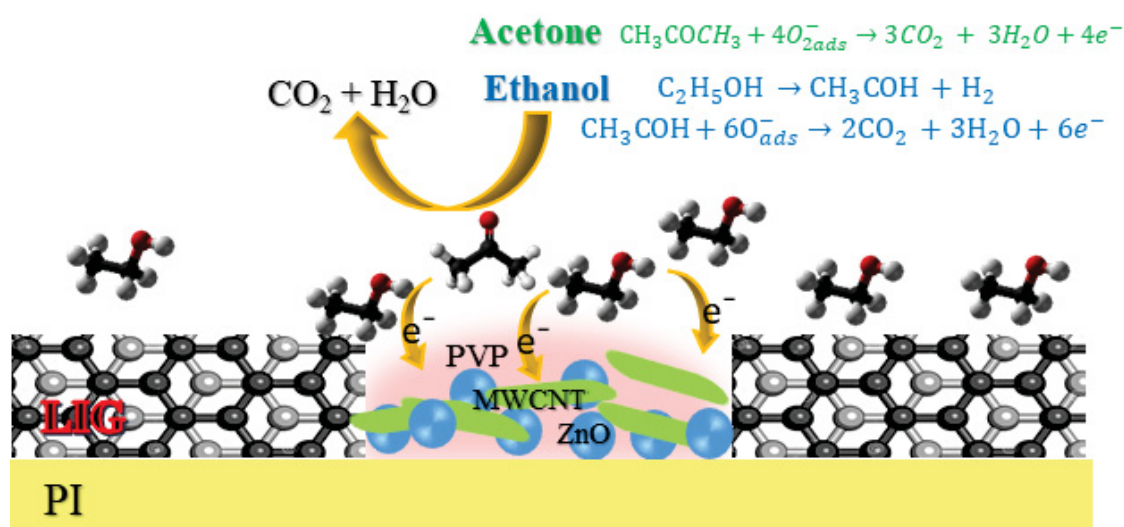
Figure 49 – Adsorption and reaction mechanism of acetone or ethanol on the sensing surface.

4.5   SUMMARY

The study introduced laser-written graphene sensors for acetone and ethanol detection, employing ZnO, MWCNTs and PVP with LIG electrodes. At concentrations up to 300 ppm, sensors showed low limits of detection (LoD), notably achieving a low LoD of 8 ppm for acetone and 58 ppm for ethanol in LIG/ZnO/MWCNTs sensors. Incorporating PVP enhanced sensor performance, with LoDs of 11 ppm for acetone and 17 ppm for ethanol in LIG/ZnO/MWCNTs/PVP sensors. Complex impedance spectroscopy characterized sensor behavior, indicating sensitivity to analyte concentration. The study demonstrates cost-effective, scalable VOC sensors suitable for laser-induced graphene electronics applications, with surface charge influencing sensing performance.

5 CONCLUSIONS

This project aimed to optimize the sensing performance of VOCs gas sensors through the evaluation of different sensing materials and their performance in the presence of analyte mixtures. The initial phase of the study focused on assessing the sensing capabilities hBN flakes modified with BaF_2 towards VOCs. The results revealed that the sensing devices utilizing hBN nanostructures exhibited activity for detecting acetone and ethanol, with their performance influenced by the structural properties of the nanostructures.

The pristine hBN and the 2.5 wt% BaF_2-modified hBN-based sensors demonstrated improved sensing capabilities for both analytes. This was evident from their low limits of detection (LoDs) ranging from 43 to 86 ppm for acetone and 30 to 62 ppm for ethanol, as well as high sensitivities of 1.8 to 2.1×10^{-2} ppm^{-1} for acetone and 1.5 to 1.6×10^{-2} ppm^{-1} for ethanol. These enhancements can be attributed to the presence of defective domains in these samples, providing abundant adsorption sites for the target analyte molecules.

However, despite the 5-10 wt% BaF_2-modified hBN-based sensors exhibiting rapid response and recovery times, the improved two-dimensional (2D) morphology of the hBN flakes hindered their sensing performance towards acetone and ethanol. This was evident from the high LoD values ranging from 144 to 460 ppm for acetone and 134 to 543 ppm for ethanol, along with extremely poor sensitivities of 0.042 to 0.72×10^{-2} ppm^{-1} for acetone and 0.045 to 0.19×10^{-2} ppm^{-1} for ethanol in the structurally improved 5-10 wt% BaF_2-modified hBN flakes. The decline in sensor activity could also be attributed to the relatively low surface areas of the hBN nanostructures, ranging from 2.9 to 3.5 m²/g.

The second part of the investigation involved the development of fully laser-written graphene sensors capable of detecting acetone and ethanol with a low limit of detection. Various sensor structures were employed, utilizing ZnO, MWCNTs and PVP as sensing materials in combination with LIG electrodes. The experimental results and calculations demonstrated that as the concentration level increased from 0 to 300 ppm, the response resistance of the LIG/ZnO/MWCNTs and LIG/ZnO/MWCNTs/PVP-based sensors showed remarkable LoD at a frequency of 100 Hz. For sensors based on LIG/ZnO/MWCNTs, the ultra-lowest LoD of 8 ppm and 58 ppm for acetone and ethanol, respectively, was achieved, with a sensitivity of 0.076×10^{-2} ppm^{-1} and 0.018×10^{-2} ppm^{-1}. For sensors based on LIG/ZnO/MWCNTs/PVP, the LoD of 11 ppm for acetone and 17 ppm for ethanol was observed, with a sensitivity of 0.191×10^{-2} ppm^{-1} and 2.319×10^{-2} ppm^{-1}, respectively. The incorporation of the polymer

enhanced the dispersion of MWCNTs within the interdigitated LIG electrode, resulting in an increased electrical response. Moreover, both the LIG/ZnO/MWCNTs and LIG/ZnO/MWCNTs/PVP-based sensors exhibited response and recovery times within the range of less than 300 seconds at room temperature. Overall, this work demonstrates the feasibility of a cost-effective and scalable method for producing high-performance VOC sensors suitable for laser-induced graphene electronics applications.

Complex impedance spectroscopy revealed a clear and distinct single semicircle, which could be effectively modeled using simple parallel resistance-capacitance circuits, with parameters calculated accordingly. The influence of various analyte concentrations on the complex impedance behavior was investigated. The study indicates that the sensing performance was primarily influenced by the surface charge of the grains in the LIG/ZnO/MWCNTs and LIG/ZnO/MWCNTs/PVP-based sensors.

FUTURE DIRECTIONS

Following are some potential research directions that could be pursued based on this project:

1.   Investigate the impact of other metal oxides as active materials, emphasizing the importance of finding suitable conditions for dispersing the structures. A comparative analysis between different types of metal oxides on LIG electrodes would provide valuable insights.

2.   Explore the influence of humidity and light on sensing performance to complete the analysis. Real-world applications are often affected by humidity and light, which can significantly impact sensor responses.

3.   When fabricating devices through drop casting, it would be interesting to study the morphology of the films. Understanding the efficacy of techniques used to achieve homogeneous films, such as controlled drying steps and the application of deposition of dispersions by steps in small quantities, is essential.

4.   Experiment with sensors based on alternative materials, such as tungsten disulfide (WS_2) and phosphorene, which have garnered considerable attention as potential candidates for VOCs detection.

5.   Evaluate a large number of sensors and analytes under standardized conditions (e.g., substrate type, analyte concentration, setup) to statistically analyze sensor performance and reliably analyze mixtures.

REFERENCES

[1] B. R. Eggins, *Chemical Sensors and Biosensors*, **2004**.

[2] A. H. Deshpande, J. M. Weldode, J. S. Pise, *Int J Manag Technol Eng* **2018**, *8*, 1403.

[3] M. Ghasemi, et al., *Eng Agric* **2019**, *9*, 365.

[4] T. Eamsa-ard, T. Seesaard, T. Kitiyakara, T. Kerdcharoen, in *9th Biomed. Eng. Int. Conf. BMEiCON*, **2016**.

[5] C. W. Na, J. H. Kim, H. S. Woo, A. Gupta, H. K. Kim, J. H. Lee, *Sens. Actuators B Chem* **2018**, *255*, 1671.

[6] W. Chen, S. Laiho, O. Vaittinen, L. Halonen, F. Ortiz, C. Forsblom, P. H. Groop, M. Lehto, *J Breath Res* **2016**, *10*, 036011.

[7] B. Timmer, W. Olthuis, A. Den Berg, *B Chem* **2005**, *107*, 666.

[8] M. A. Franco, P. P. Conti, R. S. Andre, D. S. Correa, *Sens. Actuators Rep.* **2022**, *4*, 100100.

[9] L. Clark, C. Lyons, *Ann N Acad Sci* **1962**, *102*, 29.

[10] F. Regan, *Encycl. Anal. Sci.* **2019**, 172.

[11] M. Soler, O. C. Huertas, L. M. Lechuga, *Expert Rev. Mol. Diagn.* **2019**, *19*, 71.

[12] M. C. Estevez, M. Alvarez, L. M. Lechuga, *Laser Photonics Rev.* **2012**, *6*, 463.

[13] M. Soler, O. Calvo-Lozano, M. C. Estevez, L. M. Lechuga, *Opt. Photonics News* **2020**, *31*, 24.

[14] L. Ramirez, A. T. C. Johnson, G. Preti, *J. Clin. Oncol.* **2018**, *36*, 17524.

[15] N. Kybert, K. Prokop-Prigge, G. Preti, A. Krilaviciute, J. A. Heiss, J. K. Ma. Leja, H. Haick, H. Brenne, *AIP Adv.* **2020**, *10*, 035213.

[16] A. Krilaviciute, J. A. Heiss, M. Leja, J. Kupcinskas, H. Haick, A. Brenne, *Oncotarget* **2015**, *6*, 38643.

[17] G. Peng, U. Tisch, H. Haick, *Nat. Nanotechnol. Vol.* **2009**, *4*, 669.

[18] Y. Broza, H. Haick, *Nanomed.* **2013**, *8*, 785.

[19] M. Hakim, Y. Broza, O. Barash, N. Peled, M. Phillips, A. Amann, H. Haick, *Chem Rev* **2012**, *112*, 5949.

[20] D. Hashoul, H. Haick, *Eur. Respir. Rev.* **2019**, *28*, 190011.

[21] T. Huynh, H. Haick, *Adv. Mater.* **2018**, *30*, 1802337.

[22] X. Chu, X. Zhu, Y. Dong, X. Ge, S. Zhang, W. Sun, *J Mater Sci Technol* **2012**, *28*, 200.

[23] M. Riguettoni, A. Tricoli, J. B. Res, **2011**, *5*, 037109.

[24] D. Smith, P. Spanel, A. A. Fryer, F. Hanna, A. A. Ferns, *J Breath Res* **2011**, *5*, 022001.

[25] J. Shin, S. J. Choi, I. Lee, D. Y. Youn, C. O. Park, J. H. Lee, H. L. Tuller, I. D. Kim, *Adv. Funct. Mater.* **2013**, *19*, 2357.

[26] Y. Fan, X. Zhu, H. Sui, H. Sun, Z. Wang, *Sensors* **2019**, *19*, 369.

[27] R. Paolesse, S. Nardis, D. Monti, M. Stefanelli, C. Natale, *Chem Rev* **2017**, *117*, 2517.

[28] G. E. Olifant, V. Mavumengwana, I. A. Hümmelgen, M. A. Mamo, J. Mater, *J Mater Sci Mater Electron* **2019**, *30*, 3552.

[29] B. J. Matsoso, C. Garcia-Martinez, T. H. Mongwe, T. Bérangère, J. P. M. Serbena, C. Journet, *J Phys Mater* **2021**, *4*, 044007.

[30] B. Matsoso, C. Garcia-Martinez, T. H. Mongwe, B. Toury, J. P. M. Serbena, C. Journet, *Chemosensors* **2021**, *9*, 263.

[31] I. Usman, C. Garcia, J. Matsoso, I. Cruz, R. Erasmus, *Mater. Today Commun.* **2022**, *33*, 104704.

[32] A. Paliwal, A. Jain, D. Jain, V. Kate, K. Namdev, *Int. J. Sci. Res. Dev.* **2020**, *8*, 2321.

[33]   C. K. Amuzuvi, P. K. Ashilevi, *Ghana J. Technol.* **2016**, *1*, 12.

[34]   M. N. Padvi, A. V. Moholkar, S. R. Prasad, N. R. Prasad, *Eng Sci* **2021**, *15*, 20.

[35]   M. Halder, S. Chatterjee, *Int. J. Eng. Appl. Sci.* **2019**, *6*, 2394.

[36]   M. V. Nikolic, V. Milovanovic, Z. Z. Vasiljevic, Z. Stamenkovic, *Sensors* **2020**, *20*, 6694.

[37]   P. Dariyal, S. Sharma, G. S. Shauhan, B. P. Singh, S. R. Dhakate, *Nanoscale Adv* **2021**, *3*, 6514.

[38]   W. H. Brattain, J. Bardeen, *Bell Syst Tech J* **1952**, *32*, 1.

[39]   G. Heiland, *Z Phys.* **1954**, *138*, 459.

[40]   Shaver P. J., *Appl Phys Lett* **1967**, *11*, 255.

[41]   N. Taguchi, **1971**, 3,631,436.

[42]   N. Joshi, T. Hayasaka, Y. Liu, H. Liu, O. Oliveira Jr., L. Lin, *Mikrochim Acta* **2018**, *185–213*.

[43]   G. Neri, *Chemosensors* **2015**, *3*, 1.

[44]   P. V. Shinde, C. S. Rout, *Nanoscale Adv* **2021**, *3*, 1551.

[45]   H. Bi, X. Han, *Chem. Gas Biosens. Internet Things Relat. Appl.* **2019**, 147.

[46]   S. Abdul, T. Judit, F. Ilona, M. Nikoletta, *Micro Nano Technol.* **2018**, 485.

[47]   S. F. Shaikh, M. Ubaidullah, R. S. Mane, A. M. Al-Enizi, *Micro Nano Technol.* **2020**, 51.

[48]   S. Guo, *Molecules* **2022**, *27*, 5381.

[49]   A. Dey, *Mater. Sci. Eng. B* **2018**, *229*, 206.

[50]   J. Cao, C. Qian, W. Xiaoshan, Z. Qiang, Y. Hai-Dong, H. Xiao, H. Wei, *Research.* **2021**, *2021*, 9863038.

[51]   T. Suzuki, A. Sackmann, A. Oprea, U. Weimar, N. Barzan, *ACS Sens* **2020**, *5*, 2555−2562.

[52]   M. Latino, G. Neri, *Atti Accad Pelorit Pericol Cl Sci Fis Mat Nat* **2021**, *98*, 41.

[53]   L. Filipovic, S. Selberherr, *Nanomater. Basel* **2022**, *12*, 3651.

[54]   K. M. Kabir, M. J. Baker, W. A. Donald, *Trends Anal. Chem.* **2022**, *153*, 116655.

[55]   K. B. Reddy, P. H. Borse, *J Electrochem Soc* **2021**, *168*, 057521.

[56]   T. Li, G. Liu, H. Kong, G. Yang, G. Wei, X. Zhou, *Coord. Chem. Rev.* **2023**, *475*, 214909.

[57]   A. Goyal, H. Dutta, S. Pal, *J Phys Appl Phys* **2017**, *50*, 203001.

[58]   A. Ghosh, A. Pal, N. Das, *Opt. - Int. J. Light Electron Opt.* **2020**, *208*, 163997.

[59]   Z. Wang, Y. Wang, J. Yan, B. Liu, Y. Chen, Y. Tian, *Mater Adv* **2022**, *3*, 6728.

[60]   C. Yuan, J. Ma, Y. Zou, G. Li, H. Xu, V. Sysoev, X. Cheng, Y. Deng, *Adv Sci* **2022**, *9*, 2203594.

[61]   M. M. Abdullah, P. Singh, S. Ikram, *Micro Nano Technol.* **2020**, 123.

[62]   A. Mirzaei, *Chemosensors* **2022**, *10*, 289.

[63]   N. Yamazoe, K. Shimanoe, *Sens. Actuators B* **2008**, *128*, 566.

[64]   A. Calvi, A. Ferrari, L. Sbuelz, A. Goldoni, S. Modesti, *Sensors* **2016**, *16*, 731.

[65]   E. Ciftyurek, Z. Li, K. Schierbaum, *Sensors* **2023**, *23*, 29.

[66]   Y. G. Song, G. S. Kim, B. Ju, C. Kang, *J Sens Sci Technol* **2020**, *29*, 1.

[67]   T. Lin, X. Lv, Z. Hu, A. Xu, C. Feng, *Sensors* **2019**, *19*, 233.

[68]   X. Liu, *Nanoscale* **2015**, 14872.

[69]   T. Chen, Q. J. Liu, Z. L. Zhou, Y. D. Wang, *Nanotechnology* **2008**, *19*, 095506.

[70]   Y. Li, *Sens. Actuators B* **2017**, *238*, 264.

[71]   R. Zhao, Z. Wang, T. Zou, *J Mater Sci Mater Electron* **2019**, *30*, 3032.

[72]   A. O. Mohamed, E. K. Paleologos, *Fundam. Geoenvironmental Eng.* **2018**, 205.

[73]   C. Garcia-Martinez, Ammonia Sensors in Humid Environment, Universidade Federal do Paraná, **2020**.

[74] H. J. Kim, J.-H. Lee, *Sens. Actuators B* **2014**, *192*, 607.

[75] Majhi S. M., *Nano Energy* **2021**, *79*, 105369.

[76] C. Wang, L. Yin, L. Zhang, D. Xiang, R. Gao, *Sensors* **2010**, *10*, 2088.

[77] B. Wang, L. Sun, M. Ramelow, K. Lang, H. Ngo, *Micromachines* **2021**, *12*, 1429.

[78] J. Morales, A. Maldonado, M. Olvera, in *12th Int. Conf. Electr. Eng. Comput. Sci. Autom. Control CCE*, **2015**, pp. 1–5.

[79] E. Fazio, *Sensors* **2021**, *21*, 2494.

[80] P. Nag, P. Devi, *Trans Ind Ceram Soc* **2015**, *74*, 129.

[81] Z. Feng, A. Gaiardo, M. Valt, E. Fabbri, D. Casotti, S. Krik, L. Vanzetti, M. D. Ciana, S. Fioravanti, S. Caramori, *Sensors* **2022**, *22*, 1233.

[82] S. Choopun, N. Hongsith, E. Wongrat, **2012**.

[83] A. Sarkar, S. Maity, P. Chakraborty, S. Chakraborty, *Int. J. Sci. Res. IJSR* **2015**, *6*, 2319.

[84] Y. Gautam, et al., *R Soc Open Sci* **2021**, *8*, 201324.

[85] V. Harish, et al., *Nanomaterials* **2022**, *12*, 457.

[86] J. Jeevanandam, A. Barhoum, Y. Chan, A. Dufresne, M. Danquah, *Beilstein J Nanotechnol* **2018**, *9*, 1050.

[87] H. Zhang, Y. Guo, F. Meng, *Chemosensors* **2022**, *10*, 231.

[88] T. Pandhi, A. Chandnani, H. Subbaraman, D. Estrada, *Sensors* **2020**, *20*, 5642.

[89] P. Gründler, *Chemical Sensors An Introduction for Scientists and Engineers*, Springer, Dresden, **2007**.

[90] J. G. Webster, *Measurement, Instrumentation and Sensors*, Taylor & Francis Group, London, **1999**.

[91] J. Janata, *Principles of Chemical Sensors*, Springer, Atlanta, **2009**.

[92] A. Javey, J. Konj, *Carbon Nanotube Electronics*, Springer, New York, NY, USA, **2009**.

[93] S. Ratan, *Nanotechnology* **2019**, *30*, 395501.

[94] G. Korotcenkov, B. K. Cho, *Sens. Actuators B Chem* **2017**, *244*, 182.

[95] G. Korotcenkov, B. K. Cho, *Sens. Actuators B Chem* **2013**, *188*, 709.

[96] G. L. Donati, *J Anal Chem* **n.d.**, *9*, 8.

[97] H. Rahman, M. M. Rahman, *Bangladesh Agric* **2015**, *19*, 55.

[98] R. Boqué, Y. Vander Heyden, *LCGC Eur.* **2009**, *22*, 82.

[99] M. Yang, S. Zhang, F. Qu, S. Gong, C. Wang, L. Qiu, M. Yang, W. Cheng, *Alloys Compd* **2019**, *797*, 246.

[100] H. Zhao, Y. Wang, Y. Zhou, *Materials* **2023**, *16*, 3249.

[101] D. R. Patil, Patil, *Talanta* **2009**, *77*.

[102] R. Tang, Y. Shi, Z. Hou, L. Wei, *Sensors* **2017**, *17*, 882.

[103] R. Zhang, Y. Wang, *Sensors* **2018**, *18*, 2211.

[104] F. Meng, *J Alloys Compd* **2022**, *893*, 162189.

[105] C. Bur, Selectivity Enhancement of Gas Sensitive Field Effect Transistors by Dynamic Operation, Linköping University, **2015**.

[106] L. Meng, *Actuators B Chem* **2021**, *342*, 130018.

[107] M. Morales, J. Halpern, *Bioconjug Chem* **2018**, *29*, 3231.

[108] V. Balasubramani et al., *J Electrochem Soc* **2020**, *167*, 037572.

[109] J. Aguedo, L. Lorencova, M. Barath, P. Farkas, J. Tkac, *Chemosensors* **2020**, *8*, 127.

[110] H. Herrera et al., *Electrochemical Impedance Spectroscopy (EIS): A Review Study of Basic Aspects of the Corrosion Mechanism Applied to Steels*, **2020**.

[111] H. Cesiulis, N. Tsyntsaru, A. Ramanavičius, G. Ragoisha, **2019**.

[112] W. Choi, H. Shin, J. Kim, J. Choi, W. Yoon, *J Electrochem Sci Technol* **2020**, *11*, 1.

[113] C. Brett, *Molecules* **2022**, *27*, 1497.

[114] J. Macdonald, *Ann. Biomed. Eng.* **1992**, *20*, 289.

[115] S. Feliu, *Metals* **2020**, *10*, 775.

[116] J. Huang, Z. Li, B. Liaw, J. Zhang, *J. Power Sources* **2016**, *309*, 82.

[117] E. Ellis, E. Smith, **2018**, pp. 163–196.

[118] F. Schipani, D. R. Miller, M. A. Ponce, C. M. Aldao, S. A. Akbar, P. A. Morris, *Rev. Adv. Sci. Eng.* **2016**, *5*, 86.

[119] M. E. Orazem, B. Tribollet, *Electrochemical Impedance Spectroscopy*, John Wiley & Sons, Inc., New York, NY, USA, **2008**.

[120] E. Hauff, D. Klotz, *J Mater Chem C* **2022**, *10*, 742.

[121] G. W. Hunter, *J. Electrochem. Soc.* **2020**, *167*, 037570.

[122] J. Rossignol, A. Harrabi, D. Stuerga, P. Pribetich, G. Bailly, T. Leblois, *ACS Omega* **2020**, *5*, 11507 11514.

[123] M. Vázquez, A. Dominguez-Alfaro, N. Alegret, A. Silvestri, I. J. Gómez, *Sens. Bio-Sens. Res.* **2022**, *38*, 100540.

[124] S. S. Varghese, S. H. Varghese, S. Swaminathan, K. Kumar, V. Mittal, *Electronics* **2015**, *3*, 651.

[125] P. Ares, K. S. Novoselov, *Nano Mater. Sci.* **2022**, *4*, 3.

[126] Bhimanapati, et al., *2D Mater* **2016**, *3*, 025028.

[127] M. Zhao, *Crystals* **2022**, *12*, 1087.

[128] O. Hod, *J Chem Theory Comput* **2012**, *8*, 1360 1369.

[129] X. Ye, Y. Du, M. Wang, B. Liu, J. Liu, S. Jafri, W. Liu, R. Papadakis, X. Zheng, H. Liu, *Nanomaterials* **2023**, *13*, 1379.

[130] M. Li, G. Huang, X. Cheng, J. Yin, P. Zhang, Y. Yao, J. Shen, Y. Wu, J. Huang, *Nano Today* **2022**, *44*, 101486.

[131] C. Gautam, S. Chelliah, *RSC Adv* **2021**, *11*, 31284.

[132] M. Sajjad, P. Feng, *Mater. Res. Bull.* **2014**, *49*, 35.

[133] B. J. Matsoso, V. Vuillet-a-ciles, L. B. L, B. Toury, C. Journet, *Nanomaterials* **2020**, *10*, 6.

[134] B. K. Mutuma, R. Rodrigues, K. Ranganathan, B. Matsoso, D. Wamwangi, I. A. Hümmelgen, N. J. Coville, *J Mater Chem A* **2017**, *5*, 2539.

[135] E. T. Haugan, P. Dalsjø, *Characterization of the Material Properties of Two FR4 Printed Circuit Board Laminates*, Norwegian Defence Research Establishment (FFI), Norway, **2013**.

[136] S. Dölle, B. Lechner, J. Park, S. Schymura, J. Lagerwall, G. Scalia, *Chem Int Ed* **2012**, *51*, 3254.

[137] A. K. S. Kumar, Y. Zhang, D. Li, R. G. Compton, *Electrochem. Commun.* **2020**, *121*, 106867.

[138] G. Bussetti, S. Trabattoni, S. Uttiya, A. Sassella, M. Riva, A. Picone, A. Brambilla, L. Duò, F. Ciccacci, M. Finazzi, *Synth. Met.* **2014**, *195*, 201.

[139] B. K. Mutuma, C. I. Garcia-Martinez, R. C. Dias, B. Matsoso, N. J. Coville, I. A. Hümmelgen, *New J Chem* **2019**, *43*, 8418.

[140] R. Rodrigues, Sensores químicos para a detecção de compostos voláteis orgânicos e misturas binárias, Thesis, Universidade Federal do Paraná, **2018**.

[141] M. W. C. C. Greenshields, I. A. Hümmelgen, M. A. Mamo, A. Shaikjee, S. D. Mhlanga, W. A. L. Otterlo, N. J. Coville, *J Nanosci Nanotechnol* **2011**, *11*, 10211.

[142] Y. Shen, H. Yan, H. Guo, Y. Long, W. Li, *Sens. Actuators B Chem.* **2020**, *303*, 127248.

[143] J. C. Dyre, P. Maass, B. Roling, D. L. Sidebottom, *Rep Prog Phys* **2009**, *72*, 46501.

[144] J. Strand, L. Larcher, A. L. Shluger, *J Phys Condens Matter* **2020**, *32*, 055706.

[145] C. Sagar, V. Chinthapenta, *J Mol Model* **2020**, *26*, 1.

[146] K. Zhang, Y. Feng, F. Wang, Z. Yang, J. Wang, *J Mater Chem C* **2017**, *5*, 11992.

[147] C. Gervais, J. Maquet, F. Babonneau, C. Nuriez, E. Framery, M. Vaultier, P. Florian, D. Massiot, *Chem Mater* **2001**, *13*, 1700.

[148] S. Yang, C. Jiang, S. H. Wei, *Appl Phys Rev* **2017**, *4*, 021304.

[149] D. Wang, S. Huang, H. Li, A. Chen, P. Wang, J. Yang, X. Wang, *Sens Actuators B Chem* **2019**, *282*, 961.

[150] S. J. Kim, H. Koh, C. E. Ren, O. Kwon, K. Maleski, S. Cho, *ACS Nano* **2018**, *12*, 986.

[151] S. Li, L. X. Zhang, M. Y. Zhu, G. J. Ji, L. X. Zhao, J. Yin, L. J. Bie, *Sens Actuators B Chem* **2017**, *249*, 611.

[152] R. Boroujerdi, A. Abdelkader, R. Paul, *Nano-Micro Lett* **2020**, *12*, 1.

[153] B. Zhang, J. Liu, X. Cui, Y. Wang, Y. Gao, P. Sun, F. Liu, K. Shimanoe, N. Yamazoe, G. Lu, *Sens Actuators B Chem 2017* **2017**, *241*, 904.

[154] H. Yan, Z. Yang, P. Song, S. Zhang, Q. Wang, *RSC Adv* **2015**, *5*, 79593.

[155] S. Liang, J. Zhu, J. Ding, H. Bi, P. Yao, Q. Han, X. Wang, *Appl Surf Sci* **2015**, *357*, 1593.

[156] C. Zhu, L. Tao, Y. Wang, K. Zheng, J. Yu, *Sens. Actuators B Chem.* **2020**, *325*, 128790.

[157] A. Samouco, A. C. Marques, A. Pimentel, R. Martins, E. Fortunato, *Flex. Print. Electron.* **2018**, *3*, 044002.

[158] C. B. Arnold, A. Piqué, *MRS Bull* **2007**, *32*, 9.

[159] J. Lin, Z. Peng, Y. Liu, F. Ruiz-Zepeda, R. Ye, E. L. G. Samuel, M. G. Yacaman, B. I. Yakobson, J. M. Tour, *Nat Commun* **2014**, *5*, 1.

[160] A. Lamberti, F. Clerici, M. Fontana, L. Scaltrito, *Adv. Energy Mater.* **n.d.**, *6*, 1.

[161] N. Dixit, S. P. Singh, *ACS Omega* **2022**, *7*, 5112−5130.

[162] P. Devashish, X. Sanshui, W. Martijn, *Opt Express* **2022**, *30*, 44504.

[163] N. Parvin, V. Kumar, S. W. Joo, S.-S. Park, T. K. Mandal, *Electronics* **2022**, *11*, 3345.

[164] A. A. Moosa, M. S. Abed, *Turk J Chem* **2021**, *45*, 493.

[165] J. Stafford, O. K. Matar, C. Petit, *Chem. Eng.* **2018**, *930*, 24.

[166] S. F. Kiew, L. V. Kiew, H. B. Lee, T. Imae, L. Y. Chung, *J. Controlled Release* **2016**, *226*, 217.

[167] A. A. Iqbal, N. Sakib, A. K. M. P. Iqbal, D. M. Nuruzzaman, *Materialia* **2020**, *12*, 100815.

[168] M. A. A. Mohamed, M. Adel, A. M. Abd El-Aziz, *J. Compos. Mater.* **2023**, *57*, 4327.

[169] J. Zanoni, J. P. Moura, N. Santos, A. Carvalho, *Chemosensors* **2021**, *9*, 102.

[170] D. X. Luong, K. Yang, J. Yoon, S. P. Singh, T. Wang, C. J. Arnusch, J. M. Tour, *ACS Nano* **2019**, *13*, 2579.

[171] P. Garcia, A. Perez, G. Domenech, D. Constantin, *J Mater Chem A* **2021**, *9*, 1192.

[172] J. Rodrigues, N. Ben, M. R. Correia, M. Pimenta, *Mater. Today Chem.* **2020**, *16*, 100243.

[173] Ü. Özgür., D. Hofstetter, H. Morkoç, *Proc. IEEE* **2010**, *98*, 1255.

[174] N. F. Santos, S. O. Rodrigues, A. J. S. Pereira, T. Fernandes, T. Monteiro, *Sci. Rep.* **2021**, *11*, 17154.

[175] K. Anand, O. Singh, M. P. Singh, J. Kaur, R. C. Singh, *Sens Actuators B* **2014**, *195*, 409.

[176] Z. Sun, D. Huang, Z. Yang, X. Li, N. Hu, C. Yang, H. Wei, G. Yin, D. He, Y. Zhang, *IEEE Electron Device Lett* **2015**, *36*, 1376−1379.

[177] T. Wang, D. Huang, Z. Yang, S. Xu, G. He, X. Li, N. Hu, G. Yin, D. He, L. Zhang, *Nano Micro Lett* **2016**, *8*, 95−119.

[178] H. Du, G. Xie, Su, H. Tai, X. Du, H. Yu, Q. Zhang, *Sensors* **2019**, *19*, 889.

[179] Y. Su, Y. Xie, S. Wang, H. Tai, Q. Zhang, H. Du, H. Zhang, X. Du, Y. Jiang, *Sens Actuators B* **2017**, *251*, 144−152.

[180] P. Cao, Cai, D. Pawar, S. T. Navale, C. Rao, S. Han, W. Xu, M. Fang, X. Liu, Y. Zeng, W. Liu, D. Zhu, D. Lu, *Chem. Eng. J.* **2020**, *401*, 125491.

[181] J. Liu, S. Li, B. Zhang, Y. Xiao, Y. Gao, Q. Yang, Y. Wang, G. Lu, *Sens. Actuators B* **2017**, *249*, 715.

[182] M. A. Gomez, C. Morales, J. Melendez, A. del Campo, F. J. Urbanos, A. Diaz, L. Resendiz, J. I. Flege, D. Granados, L. Soriano, *C* **2020**, *6*, 41.

[183] T. Khoa, N. Tang, N. Thi, P. Hong, N. Ngoc, L. Viet, C. Manh, N. Van, N. Duc, N. Van, *J. Alloys Compd.* **2021**, *879*, 160457.

[184] J. Zhao, N. Yi, X. Ding, S. Liu, J. Zhu, A. Castonguay, *Chem. Eng. J.* **2023**, *456*, 140956.

[185] H. Hussein, M. H. Kareem, A. M. Abdul, *Opt. - Int. J. Light Electron Opt.* **2021**, *248*, 168107.

[186] S. Yun, J. Kim, *Sens. Actuators B* **2010**, *150*, 308.

[187] Y. Kim, S. Ha, H. Yang, Y. Kim, *Sens. Actuators B* **2007**, *122*, 211.

[188] R. W. Dreyfus, *Appl. Phys. A* **1992**, *55*, 335.

[189] Z. Peng, L. Tao, S. Zou, C. Zhu, G. Wang, H. Sun, *Chem. Eng. J.* **2022**, *428*, 131079.

[190] C. Powell, L. Pisharody, C. Thamaraiselvan, A. Gupta, H. Park, B. A. Tesfahunegn, C. P. Sharma, M. Kleinberg, *ACS Appl Nano Mater* **2022**, *5*, 11923.

[191] F. Mahmood, C. Zhang, Y. Xie, D. Stalla, J. Lin, C. Wan, *RSC Adv* **2019**, *9*, 22713.

[192] I. R. Hristovski, L. A. Merman, M. E. Mitchell, N. I. Lesack, J. Reich, J. F. Holzman, **2022**, *12*, 1241.

[193] A. C. Ferrari, J. C. Meyer, V. Scardaci, C. Casiraghi, M. Lazzeri, F. Mauri, S. Piscanec, Jang, *Phys Rev Lett* **2006**, *97*, 187401.

[194] F. Johra, J. Lee, W. Jung, *J. Ind. Eng. Chem.* **2014**, *20*, 2883.

[195] M. Wall, *Adv. Mater. Process.* **2012**, *170*, 35.

[196] A. C. Ferrari, *Solid State Commun* **2007**, *143*, 47.

[197] S. Naghdi, K. Rhee, M. T. Kim, B. Jaleh, S. Park, *Carbon Lett.* **2016**, *18*, 37.

[198] Z. Li, L. Deng, I. A. Kinloch, R. Young, *Prog. Mater. Sci.* **2023**, *135*, 101089.

[199] B. Sindhu, A. Kothuru, P. Sahatiya, S. Goel, S. Nandi, *IEEE Trans. Electron Devices* **2021**, *68*, 3189.

[200] S. Kim, O. Park, J. H. Lee, B. Ku, *Carbon Lett* **2013**, *14*, 47.

[201] P. Zaccagnini, Ballin, M. Fontana, M. Parmeggiani, S. Bianco, S. Stassi, Pedico, S. Ferrero, A. Lamberti, *Adv Mater Interfaces* **2021**, 2101046.

[202] F. Tuinstra, J. L. Koenig, *J Chem Phys* **1970**, *53*, 1126.

[203] A. A. Coelho, *J Appl Cryst* **2018**, *51*, 210.

[204] J. Sotelo, J. Bonilla, F. García, J. Gordillo, *Coatings* **2021**, *11*, 303.

[205] N. H. Al-Hardan, M. J. Abdullah, A. Abdul, *Int. J. Hydrog. Energy* **2010**, *35*, 4428.

[206] W. Tian, W. Li, W. Yu, X. Liu, *Micromachines* **2017**, *8*, 163.

[207] M. Ali, M. Tit, *Surf. Sci.* **2019**, *684*, 28.

[208] J. Lee, J. Hwang, J. J. Mashek, T. O. Mason, A. E. Miller, R. W. Siegel, *J. Mater. Res.* **1995**, *10*, 2295.

[209] G. H. Shahkhatuni, V. M. Aroutiounian, V. M. Arakelyan, et al., *J Contemp Phys* **2019**, *54*, 188.

[210] I. Kim, A. Rothschild, H. Tuller, *Appl Phys Lett* **2006**, *88*, 72902.

[211] Z. Ahmad, M. K. Abdullah, M. Z. Ali, M. A. M. Zawawi, in *Polym. Electron.*, Elsevier, **2023**, pp. 225–271.

[212] S. S. Golia, M. Arora, in *Ind. Appl. Nanocrystals* (Eds.: S. Mallakpour, C. M. Hussain), Elsevier, **2022**, pp. 219–249.

[213] N. Goel, K. Kunal, A. Kushwaha, M. Kumar, *Eng. Rep.* **2023**, *5*, e12604.

[214] N. Bârsan, U. Weimar, *J. Electroceramics* **2001**, *7*, 143.

[215] S. Choi, G. Ankonina, D. Youn, S. Oh, J. Hong, A. Rothschild, I. Kim, *ACS Nano* **2009**, *3*, 2623.

[216] S. Carrara, V. Bavastrello, D. Ricci, E. Stura, C. Nicolini, *Sens Actuators B* **2005**, *109*, 221.

[217] J. Jorcin, M. Orazemb, N. Pébère, B. Tribollet, *Electrochimica Acta* **2006**, *51*, 1473.

[218] N. Bârsan, U. Weimar, *J Phys Condens Matter* **2003**, *15*, R813.

[219] A. Labidi, C. Lambert, C. Jacolin, M. Bendahan, M. Maaref, K. Aguir, *Sens Actuators B Chem* **2006**, *119*, 74.

[220] S.-Y. Cho, H.-W. Yoo, J. Y. Kim, W.-B. Jung, M. L. Jin, J.-S. Kim, H.-J. Jeon, H.-T. Jung, *Nano Lett.* **2016**, *16*, 4508.

[221] N. Kar Chowdhury, B. Bhowmik, *Nanoscale Adv.* **2021**, *3*, 73.

[222] A. Rothschild, Y. Komem, *J. Appl. Phys.* **2004**, *95*, 6374.

[223] F. Torres, C. Blanc, C. Zamora, P. Silva, E. Anglaret, *J Phys Chem C* **2015**, *119*, 703.

[224] S. Santra, G. Hu, R. Howe, A. De Luca, S. Ali, F. Udrea, J. Gardner, S. Ray, P. Guha, T. Hasan, *Sci Rep* **2015**, *5*, 17374.

[225] M. Shooshtari, A. Salehi, S. Vollebregt, *IEEE Sens. J.* **2020**, *21*, 5763.
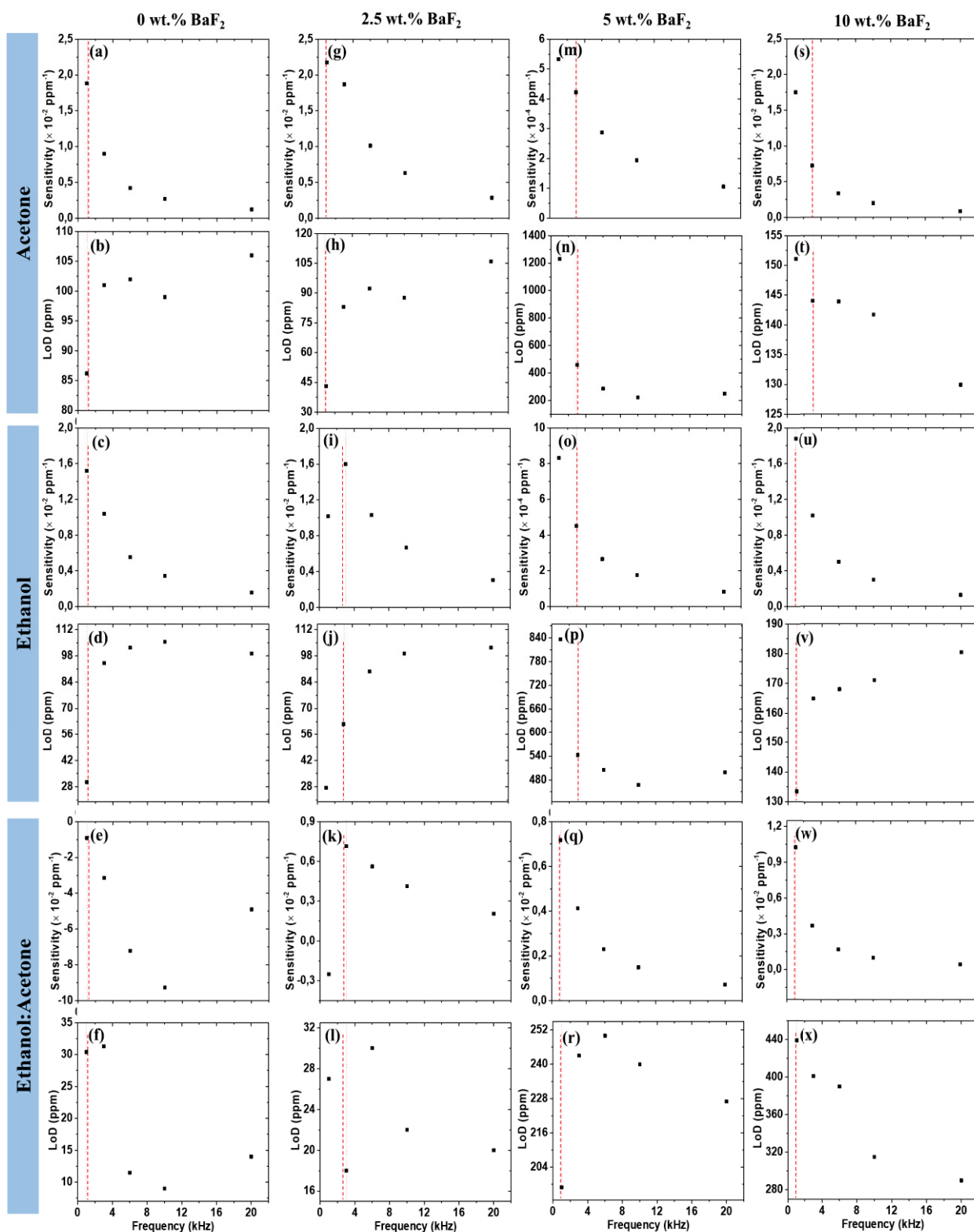
APPENDIX 1 – RESULTS

Figure A1 – The sensitivities and LoD of sensors data based on hBN-BaF$_2$ (a–f) 0 wt%, (g–l) 2.5 wt%, (m–r) 5 wt% and (s–x) 10 wt% for acetone, ethanol and EtOH:Acetone as a function frequency; dashed line indicates the optimum operating frequency.
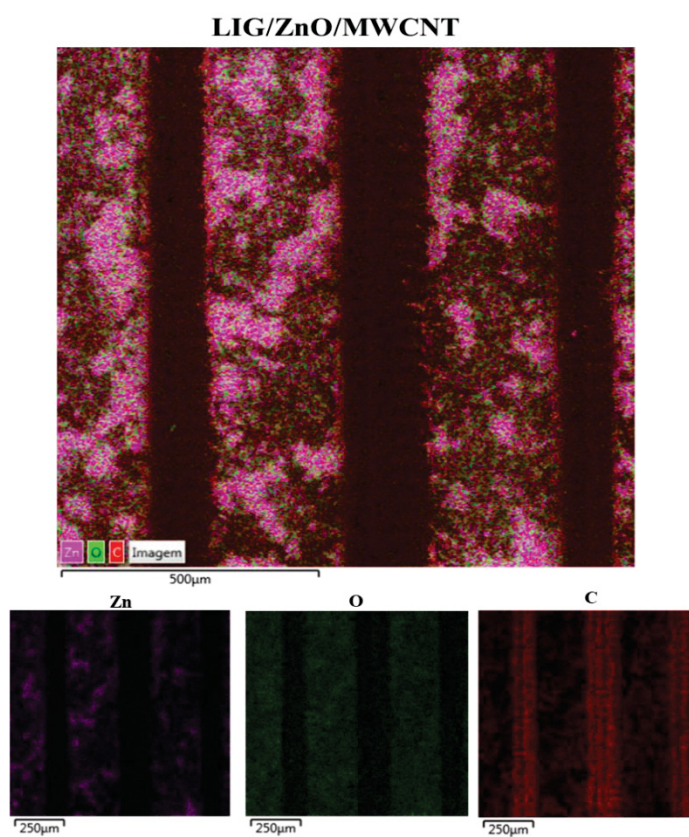
LIG/ZnO/MWCNT

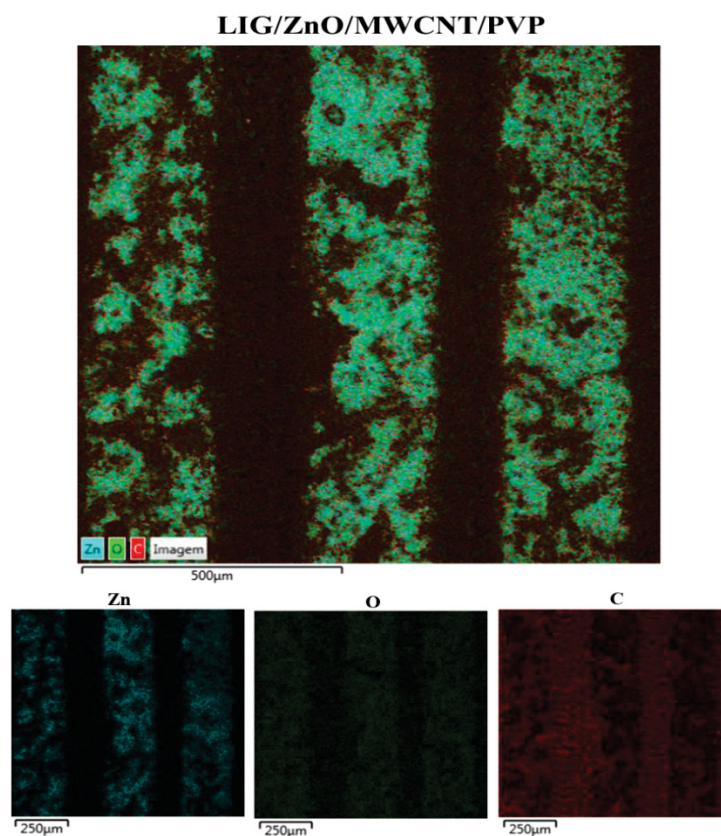Figure A2 – SEM-EDS elemental mapping images of Zn, O and C on the sensor based on LIG/ZnO/MWCNTs.

LIG/ZnO/MWCNT/PVP

Figure A3 – SEM-EDS elemental mapping images of Zn, O and C on the sensor based on LIG/ZnO/MWCNTs/PVP.
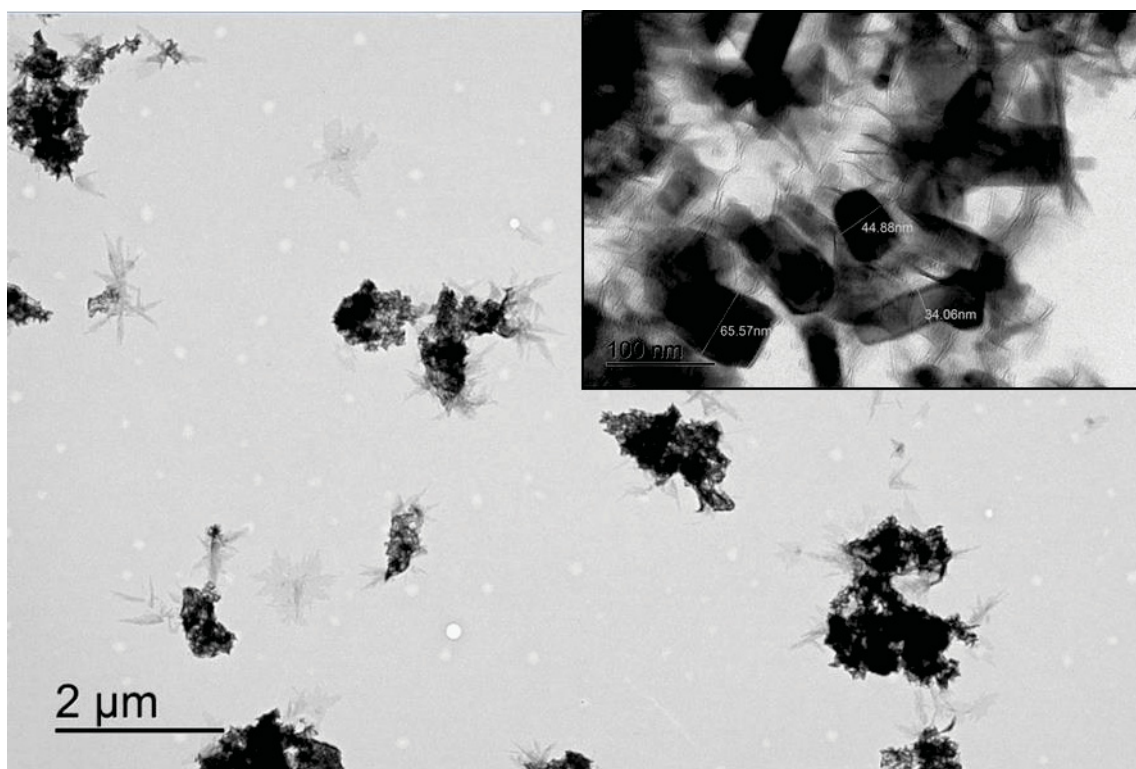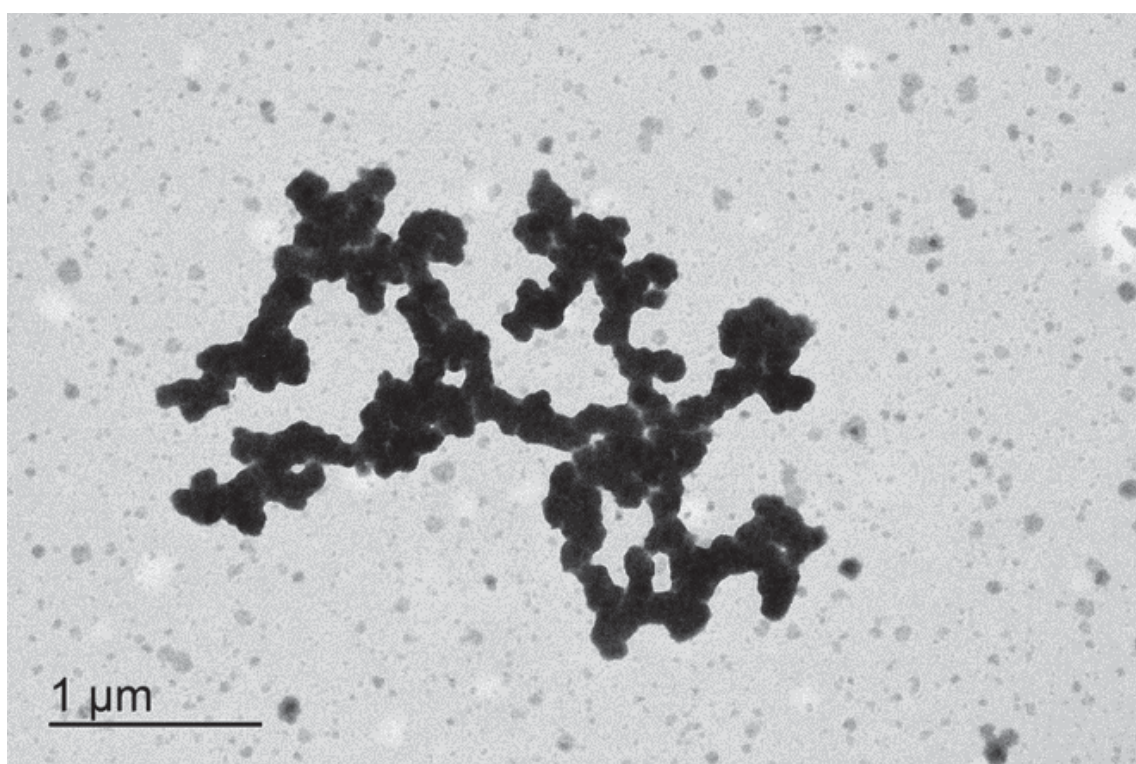
Figure A4 – TEM (inset) image of the ZnO.
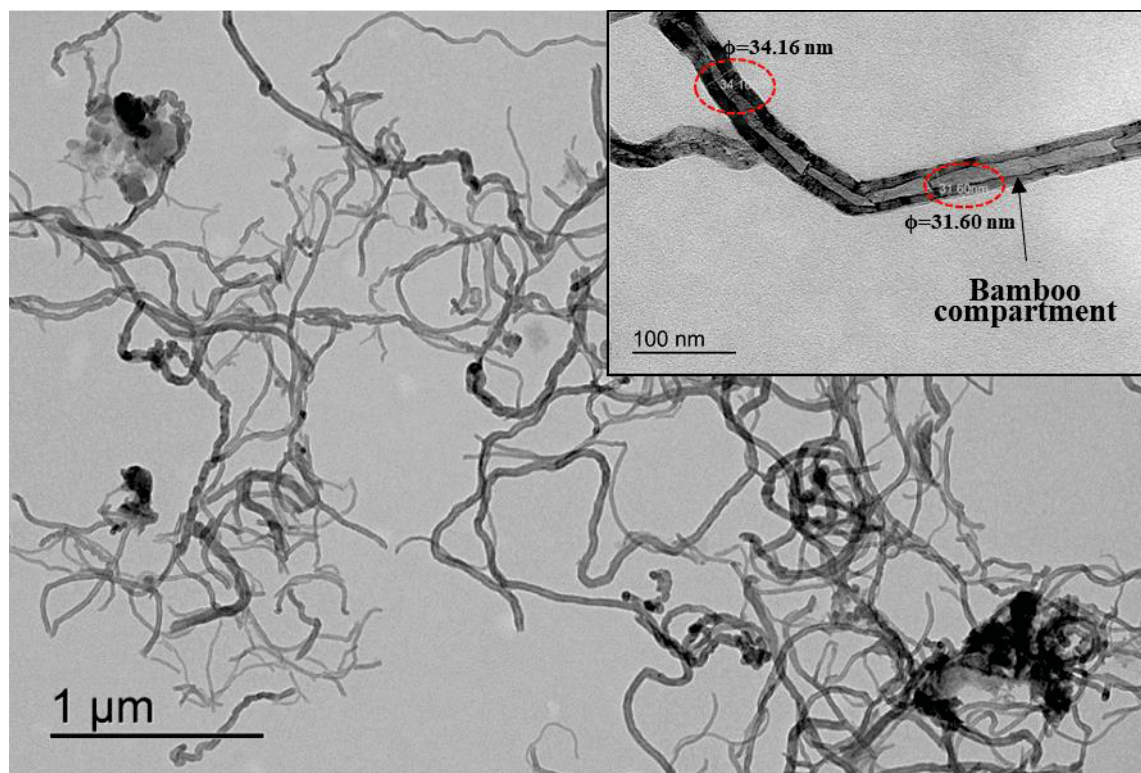

Figure A5 – TEM images of the CTAB.

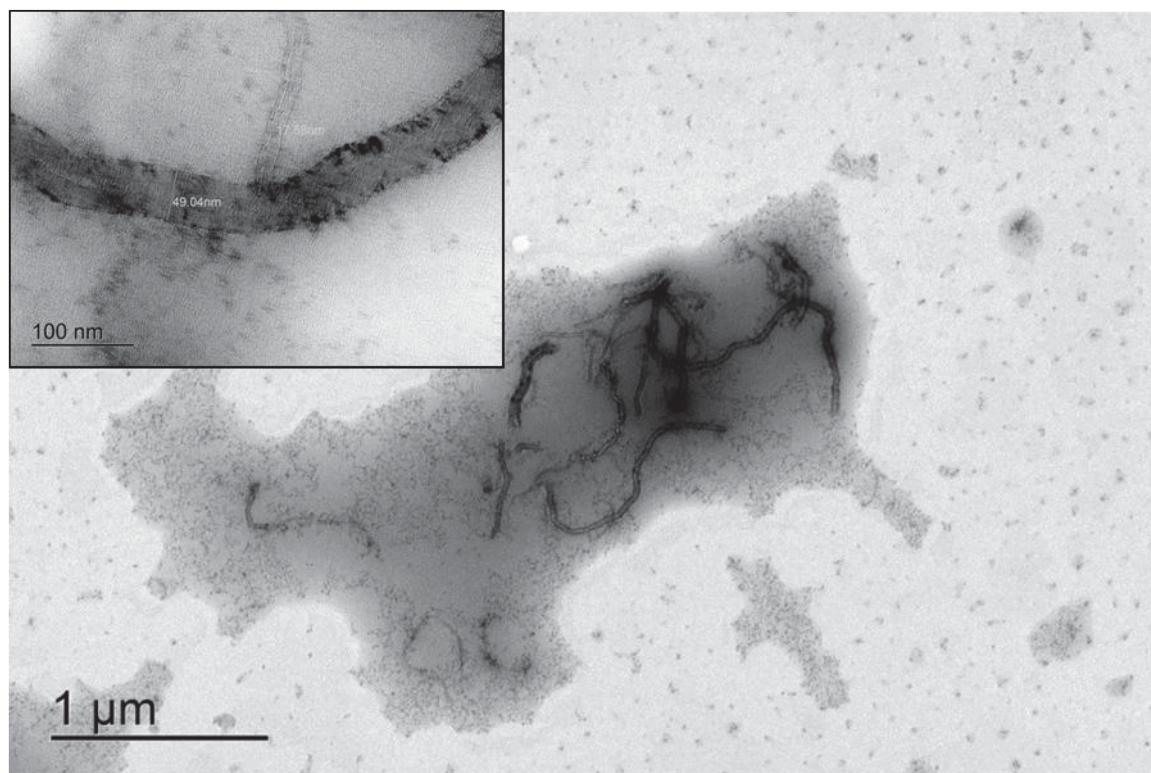Figure A6 – TEM (inset) images of the dispersion of MWCNTs with CTAB.

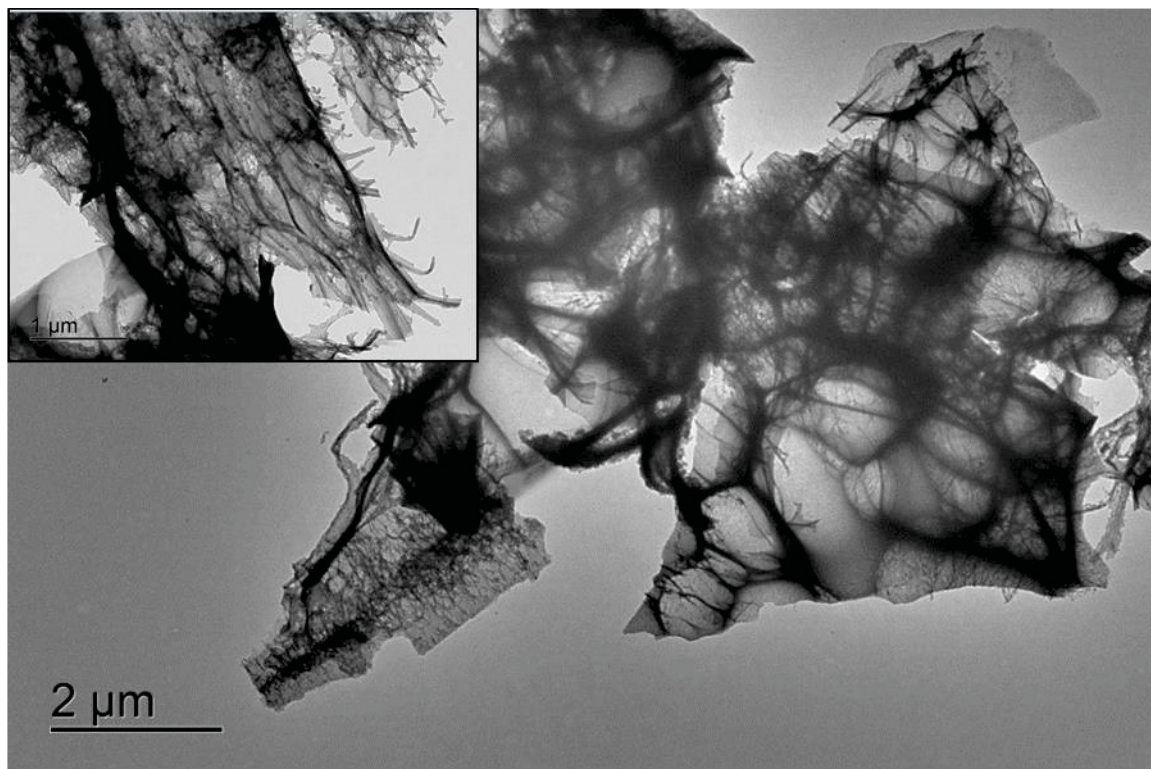Figure A7 – TEM (inset) images of the dispersion of MWCNTs-CTAB/PVP.

Figure A8 – TEM (inset) images of the LIG.

APPENDIX 2 – SCIENTIFIC CONTRIBUTIONS

1. Bridget K. Mutuma, <u>Clara I. Garcia-Martinez</u>, Boitumelo Matsoso, Rodrigo C. Dias, Neil J. Coville and Ivo A. Hümmelgen, *Nitrogen-doped hollow carbon spheres as chemical vapour sensors*, **New Journal of Chemistry**, 2019, DOI: 10.1039/C9NJ00628A. *Back cover of the NJC Journal*.

2. Boitumelo J. Matsoso, <u>Clara Garcia-Martinez</u>, Thomas H. Mongwe, Bérangère Toury, José P. M. Serbena and Catherine Journet, *Room temperature ammonia vapour detection on hBN flakes*, **Journal of Physics: Materials**, 2021, DOI: 10.1088/2515-7639/ac09d4.

3. Boitumelo J. Matsoso, <u>Clara Garcia-Martinez</u>, Thomas H. Mongwe, Bérangère Toury, José P. M. Serbena and Catherine Journet, *Chemical sensing properties of BaF2-modified hBN flakes towards detection of volatile organic compounds*, **Chemosensors**, 2021, DOI:10.3390/chemosensors9090263.

4. Carlo Trigona, Tianqi Lu, Malak Talbi, Salvatore Baglio, Ammar Al-Hamry, <u>Clara Garcia-Martinez</u> and Olfa Kanoun, *MEMS based on Chitosan – Tetrasulfonated Copper Phthalocyanine Composite for Detection of Ethanol Vapor in Air*, IEEE International Workshop on Metrology for Industry, 2022, DOI:10.1109/MetroInd4.0IoT54413.2022.9831469.

5. Ibrahim B. Usman, <u>C. I. Garcia-Martinez</u>, B. J. Matsoso, I. Cruz-Cruz, R. Erasmus, N. J. Coville J. P. M. Serbena and D. Wamwangi, *Carbon Coating of GaN Nanostructures for Enhanced Sensitivity and Selectivity of Chemical Vapours*, **Materials Today Communications**, 2022, DOI: 10.1016/j.mtcomm, 2022.104704.

6. <u>Clara I. Garcia-Martinez</u>, Tianqi-Lu, Yang Liu, Ammar Al-Hamry, Guinther Kellermann, Fabiano Yokaichiya, José Pedro Mansueto Serbena and Olfa Kanoun, *Sensing properties of LIG/ZnO/MWCNTs and LIG/ZnO/MWCNTs/PVP compound as a Volatile Organic Compounds gas sensor*, **To be Submitted.**